Alma Mater Studiorum – Università di Bologna

DOTTORATO DI RICERCA IN

CHIMICA

Ciclo XXVI

Settore Concorsuale di afferenza: 03/B2

Settore Scientifico disciplinare: CHIM/07

SELF-ASSEMBLED MONOLAYERS (SAMs) IN ORGANIC FIELD-EFFECT TRANSISTORS

Presentata da: Francesca Leonardi

Coordinatore Dottorato

Prof. Aldo Roda

Relatore

Prof. Fabio Biscarini

Co-relatore

Dott. Stefano Casalini

Esame finale anno 2014

The experimental work described in this thesis has been carried out at the Institute for Nanostructured Materials Studies (ISMN-CNR) in Bologna under the supervision of Prof. Fabio Biscarini.

Supervisor: Prof. Fabio Biscarini

Life Science Dept. - University of Modena and Reggio Emilia
Via Campi 183, I-41125 Modena, Italy
tel: +39-059-2055079
mobile: +39-3462308958
fax: +39-059-2055410
e-mail: fabio.biscarini@unimore.it
web-page: http://personale.unimore.it/Rubrica/dettaglio/fbiscari
personal web-page: http://www.bo.ismn.cnr.it/biscarinilab/index.php/en/.

Co-supervisor: Dr. Stefano Casalini

Institute of Nanostructured Materials (ISMN)
Research Division on "Nanotechnology of Multifunctional materials" (NMM)
National Research Council (CNR)
v. P. Gobetti n.101, I-40129 Bologna, Italy
office1: +39-051-6398531
office2: +39-059-2055697
mobile: +39-3487021397
fax: +39-0516398539
e-mail: s.casalini@bo.ismn.cnr.it

Dedicated to my beloved family

Abstract:

Organic printed electronics is attracting an ever-growing interest in the last decades because of its impressive breakthroughs concerning the chemical design of π-conjugated materials and their processing. This has an impact on novel applications, such as flexible-large-area displays, low- cost printable circuits, plastic solar cells and lab-on-a-chip devices.

The organic field-effect transistor (OFET) relies on a thin film of organic semiconductor that bridges source and drain electrodes. Since its first discovery in the 80s, intensive research activities were deployed in order to control the chemico-physical properties of these electronic devices and consequently their charge. Self-assembled monolayers (SAMs) are a versatile tool for tuning the properties of metallic, semi-conducting, and insulating surfaces. Within this context, OFETs represent reliable instruments for measuring the electrical properties of the SAMs in a Metal/SAM/OS junction.

Our experimental approach, named Charge Injection Organic-Gauge (CIOG), uses OTFT in a charge-injection controlled regime. The CIOG sensitivity has been extensively demonstrated on different homologous self-assembling molecules that differ in either chain length or in anchor/terminal group.

One of the latest applications of organic electronics is the so-called “bio-electronics” that makes use of electronic devices to encompass interests of the medical science, such as biosensors, biotransducers etc…

As a result, thee second part of this thesis deals with the realization of an electronic transducer based on an Organic Field-Effect Transistor operating in aqueous media. Here, the conventional bottom gate/bottom contact configuration is replaced by top gate architecture with the electrolyte that ensures electrical contact between the top gold electrode and the semiconductor layer. This configuration is named Electrolyte-Gated Field-Effect Transistor (EGOFET).

The functionalization of the top electrode is the sensing core of the device allowing the detection of dopamine as well as of protein biomarkers with ultra-low sensitivity.

Keywords:

Organic Field-Effect Transistors

Self-Assembled Monolayers

Charge Injection Organic Gauge

Dopamine

Biosensors

Index

Introduction and scientific background

The following chapter deals with a general introduction on Organic Electronics and on the charge injection mechanism through an organic semiconductor. The role of Self-Assembled Monolayers (SAMs) has been extensively elucidated as an elegant bottom-up approach for the development of new technological platforms.

1.1 Organic electronics

1.1.1 Introduction

Organic electronics is an emerging technology based on the physical-chemical properties of π-conjugated polymers or molecules. It is called 'organic' electronics because the polymers and small molecules exploited are carbon-based, as opposed to traditional electronics based on silicon, germanium etc. The seminal studies in this area date back to the late 19th century when Henry Letheby obtained a partly conductive material by anodic oxidation of aniline in sulfuric acid (probably polyaniline). In the 1950s, it was discovered that polycyclic aromatic compounds formed by semi-conducting charge-transfer complex salts with halogens. [1,2] This finding indicated that organic compounds were able to transport electrical current.
In a series of papers in 1963, DE Weiss and coworkers reported high conductivity in iodine-"doped" oxidized polypyrrole blacks. They achieved a conductivity equal to 1 S/cm. Likewise, an organic-polymer device was reported in the journal Science in 1974, which is shown in the "Smithsonian Chips" collection of the American Museum of History now. [3–6]
Applications of organic semiconductors started when conjugated polymers were successfully synthesized and their doping was well controlled. Alan J. Heeger, Alan G. MacDiarmid, and Hideki Shirakawa are credited for the "discovery and development" of conductive polymers and were jointly awarded by the Nobel Prize in Chemistry in 2000 because of their report (1977) on similarly- oxidized and iodine-doped polyacetylene. [7]
In 1982, the metal-oxide-semiconductor (MOS) structure was demonstrated by exploiting polyacetylene and polysiloxane as semiconductor and dielectric respectively. [8,9] Although the device has not reached an excellent performance, it was immediately clear the promising potential regarding to the future technology. A crucial step in the development of organic electronics technology was the demonstration in 1986 of the first Organic Field-Effect Transistor (OFET) or alternatively termed Organic Thin- Film Transistor (OTFT). [10] More recently, the development of organic heterojunction solar cell [11] and organic light emitting diode [12] were reported. Soluble organic semiconductors were developed paving the way towards printable circuits. Conjugated molecules, oligomers and polymer offer desirable features such as low cost, versatility of chemical synthesis, easy processing, and flexibility. The major disadvantage of organic electronics is the lower performances with respect to inorganic counterpart. As a result, charge carrier mobility (measured by OFET) of organic semiconductors is two/three orders of magnitude lower than crystalline silicon MOSFETs. For this reason, OFETs are not suitable for high-performance applications where high switching rate is a primary requirement. However OFET technology can compete with amorphous silicon technology, which is largely used on the backplane of LCD displays and other large area applications. In the last two decades, Organic Electronics has rapidly grown (Fig. 1.1) and, nowadays, it is possible to manufacture electronic devices with similar performances of

some inorganic ones, especially those made of amorphous Si. To resume, Organic Electronics is suitable for applications with structural flexibility, large-area processing, low-cost requirements. The OFET applications already demonstrated are: electronic papers [13,14], sensors [15] and memory devices (e.g. Radio Frequency Identification tags-RFIDs [16]).

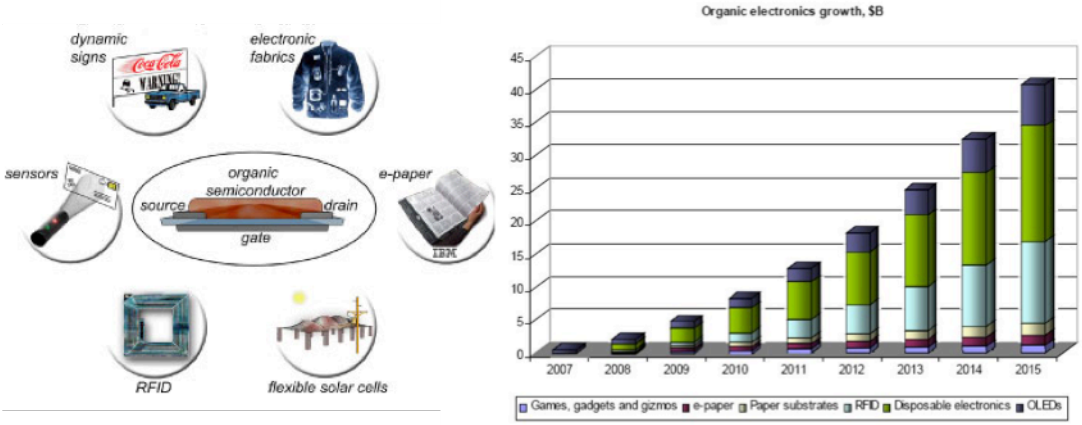

Fig. 1. 1 Some applications of Organic Electronic technology (left). Expected Organic electronic market growth (right).

1.1.2 Organic semiconductors

Organic semiconductors can be classified into two main categories: small molecules or oligomers and polymers. Low molecular weight materials and polymers are usually processed as thin-films by different techniques. For instance, small molecules can be deposited by high or ultra-high vacuum sublimation, while polymers are usually processed by wet chemical techniques, like spin-coating, drop-casting, and printing techniques. Usually semiconductor molecules show thermal and chemical stability and exhibit better OFET performance than polymers. Furthermore molecular materials can be grown as single crystals, which allows one to investigate the intrinsic charge transport properties guaranteed by the highest order and purity possible.
This class of materials presents some common features:
-They are semiconductor materials owning intermediate properties between conductor and insulator.
-They possess a carbon backbone in which each carbon is hybridized sp^2 (as show in Fig. 1.2).
-They have π-electron clouds delocalized over the entire structure.

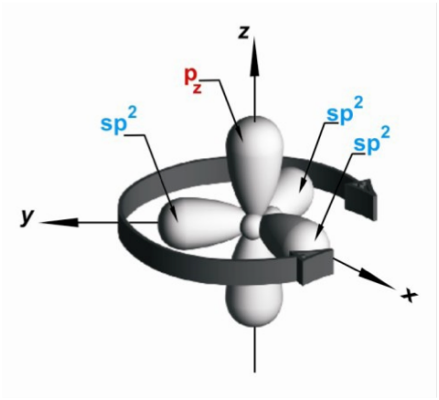

Fig. 1. 2 Scheme of the C atoms exhibiting the sp^2 hybridization geometry. The arrows around the atom indicates the plane on which the sp^2 orbitals lie.

In an organic semiconductor neighbouring C-atoms present sp^2-hybridization, the overlap of sp^2- sp^2 orbitals forms a strong covalent σ-bond, whereas the overlap of two p_z-orbitals orthogonal to the plane of molecule yields a π-bond. In terms of energy, the σ-bonds (representing the backbone of the molecules) are stronger than the π-bonds. These kinds of molecules, termed π- conjugated molecules, exhibit an electronic structure dominated by the energy band gap between the HOMO (Highest Occupied Molecular Orbital) and LUMO (Lowest Unoccupied Molecular Orbital) levels. These are the most relevant molecular orbitals for the optical and electronic properties (Fig. 1.3).

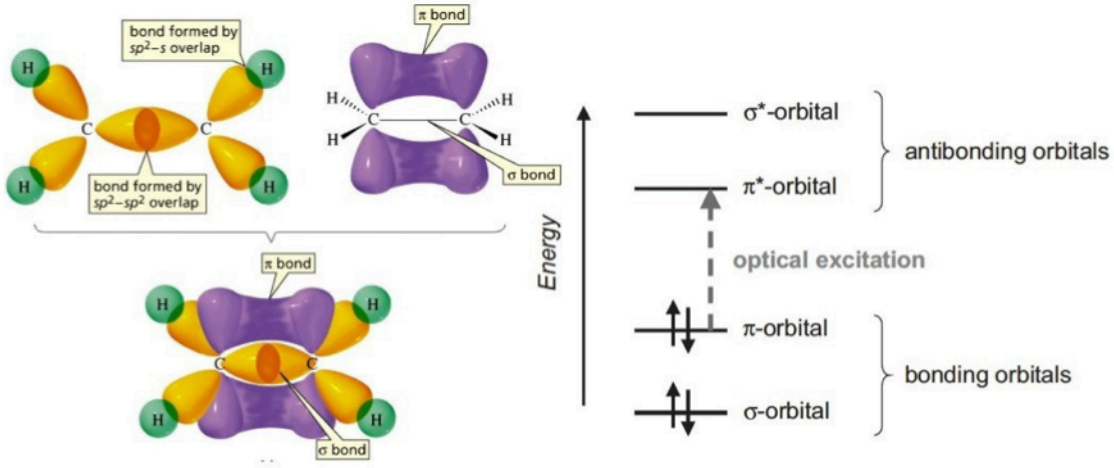

Fig. 1. 3 Ethylene molecule representations: the top view, shows the sp^2 orbitals of C-atom (the p_z orbitals are perpendicular to the page), and the σ orbitals of the H-atom; σ-bonds forms by the overlapping of sp^2 orbitals and π- bonds formed by the overlapping of p_z orbitals; the lower representation shows the whole hybridization; the right image depicts the energy levels.

In an isolated molecule, energy levels are discrete and they are the combination product of the atomic orbitals. Due to the weaker nature of the π- bond compared to σ-bond, the π-electrons are involved in electronic transitions, named π→π* between the HOMO and LUMO. As the conjugated network on a molecule becomes more spread out, the transition from HOMO to LUMO requires progressively lower energy (Fig. 1.4) and the energy band-gap, dividing the bonding and the antibonding orbitals, becomes smaller.

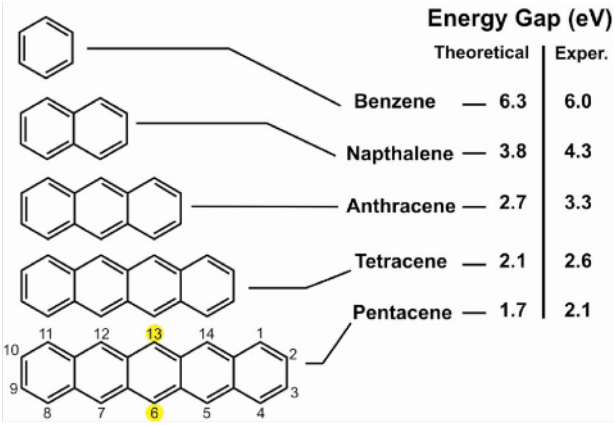

Fig. 1. 4 Molecular structure of the first five polyacenes and their HOMO-LUMO transitions (theoretical and measured). Note that the pentacene C-atom positions have been tagged. Positions 6,13 have been identified as they are the most exposed to oxidation.

1.1.3 Charge transport in organic semiconductors

In the Organic Crystals (OC) holding together molecules with the π-conjugated systems, electron can move via π-electron cloud overlaps, therefore they exhibit electrical conductivity. In an ideal scenario, HOMO and LUMO states are fully delocalized and show significant dispersion with calculated bandwidths of several eV, so for this reason the semiconducting properties are determined by these two molecular orbitals. Charge carriers can move from molecule to molecule due to weak interactions between molecules, typically Van der Waals forces [17] and this type of charge transport can be explained through the band transport model. Unfortunately, this ideal regime is valid only for semiconductor single crystals. This translates on the charge mobility to be up to 1-10 cm^2/Vs in the most perfect molecular crystals. In contrast, in inorganic crystalline semiconductors, charge carriers move as highly delocalized plane waves in wide energy bands with a very high mobility ($\sim 10^3\ cm^2/Vs$). In this case, the mobility is limited by lattice vibrations (phonons) that scatter the carriers and thus it is reduced as the temperature increases.

Organic Thin-Films have the great advantage to be fabricated at low cost with unconventional techniques; on the other hand, they show lower electrical performances than single crystals. In this case, band transport is not applicable, due to the presence of structural disorder, large number of defects and grain boundaries in thin films. As a result of the strong electron-phonon coupling and the disorder-induced finite conjugation length, charges strongly interact with molecular vibrations and are able to form localized polarons surrounded by a region of molecular distortion (Fig. 1.5).

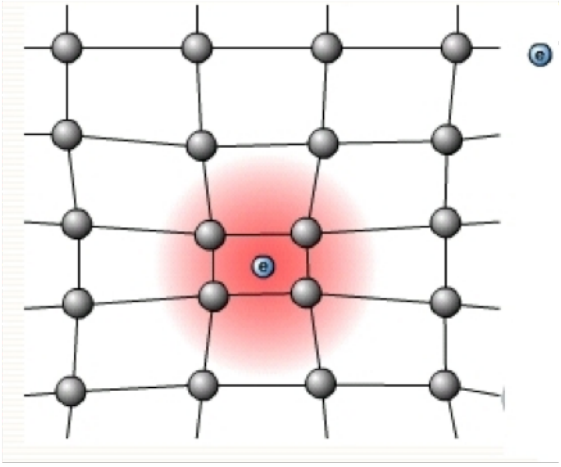

Fig. 1. 5 Schematic representation of a polaron. This is the combination of a particle and the interactions with the surrounding environment that it moves in.

The polaron is a quasiparticle formed when a charge within a molecular chain affects the local nuclear geometry, so that a cloud of phonons "dresses" the charge; this phenomenon is responsible for the generation of charge states with energies lying below LUMO and above HOMO levels. In the case of organic semiconductor, wherein the carriers are polarons, the intermolecular conduction process is determined by thermally assisted hopping between these localized polaron states [18].

In metals and inorganic single crystals semiconductors, charge transport occurs in delocalized states and it is limited by the carriers scattering, mainly on phonons that are thermally induced lattice deformations. Such model is no longer valid in low conductivity materials, like organic semiconductors, wherein a rough evaluation shows that the mean free path of carriers would become lower than the mean atomic distance. In these materials, transport takes place by hopping of charges between localized states [19,20]. The main difference between the delocalized and localized transport is the following: the former is limited by phonon scattering, whereas the latter is phonon assisted. Accordingly, the charge mobility decreases with temperature in conventional semiconductors, the reverse being true in most organic materials. Several models have been developed to rationalize hopping transport. In most cases, the temperature dependence of the mobility follows the law:

$$\mu = \mu_0 \, exp\left[-(T_0/T)^{1/\alpha}\right] \qquad \text{Eq. 1.1}$$

where α ranges from 1 to 4. The threshold between the localized and delocalized processes is usually taken at charge mobility values between 0.1 and 1 cm^2/Vs. In the highly ordered molecular crystals, the mobility is found to be in that limit. Furthermore charge carrier mobility is strictly connected to the thin-film order [17,21], and it is crucial to find the best conditions in order to enhance the long-range order and simultaneously minimizing defects in the film structure. [22,23]

Charge transport in organic semiconductors obeys a hopping mechanism. Most of organic semiconductors exclusively transport one type of charge carrier, either positive (called "holes") or negative (electrons), but not both; this interesting aspect can be explained by the density of states (DOS) of these disordered systems that is often asymmetrical and presents a non negligible barrier for the formation of one or another type of carrier. [18] For this reason,

organic semiconductors can also be divided into two categories depending on the type of charge carriers: a material is often referred to as a hole transporter (p-type semiconductor) when its ionization energy closely matches the Fermi level of the electrode, otherwise is an electron transporter (n-type semiconductor) when its electron affinity closely matches the Fermi level of the electrode. From a pure chemical point of view, a n-type molecule usually incorporates electron withdrawing groups (yielding an electron deficient conjugated core) in order to easily carry electrons, on the contrary for the p-type. In Fig. 1.6 are depicted the most common p-type and n- type organic semiconductors employed in OFET technology.

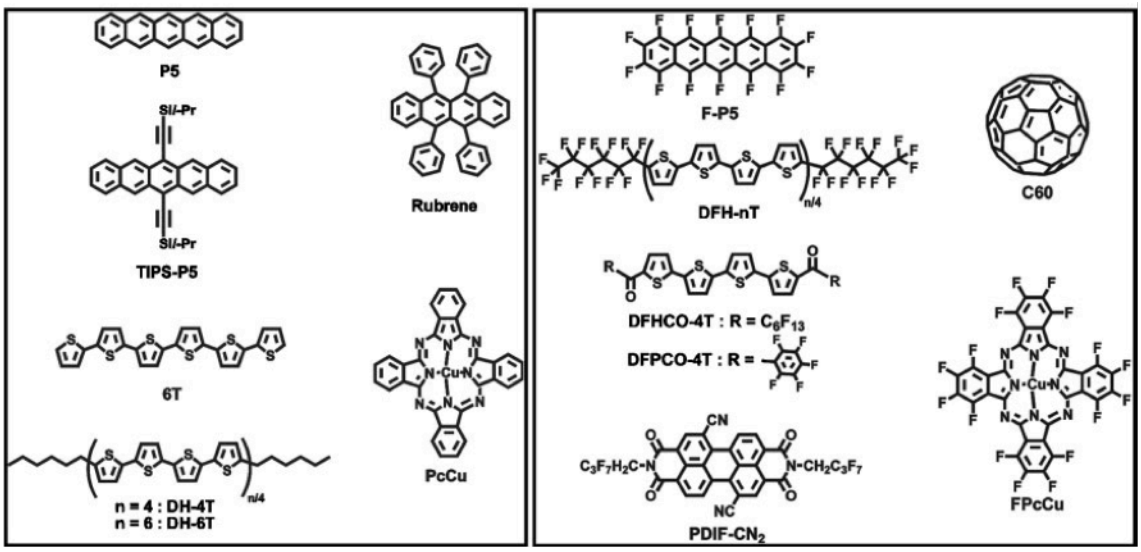

Fig. 1. 6 Examples of typical p-type (group on left), and n-type (group on right) small molecule organic semiconductors. [79]

Acenes are a class of organic compounds and polycyclic aromatic hydrocarbons made up of linearly fused benzene rings. Initial experiments on the transport properties of p-type organic semiconductors were performed with anthracene and tetracene. In the last two decades, pentacene has become one of the most extensively used organic semiconductors for OFETs applications. [24] Pentacene is commercially available and exhibits one of the highest hole mobility for a polycrystalline film: the value of 1.5 cm^2/V s was reported by Lin et al. [25]

1.2 Self-assembled Monolayers (SAMs)

1.2.1 Brief history

Self-assembly is a type of process in which disordered components organize themselves as a consequence of specific interactions and without external directions. When the constitutive components are molecules, the process is termed molecular self-assembly.
The history of self-assembly starts with the pioneering work of Zisman who in 1946 publish one of his first works about the assembly of a long chain alcohol, amine and carboxylic acid on glass and clean metal surfaces. [26]
The earliest mention of 'self-assembly' of thiols is reported in a U.S. patent 2,841,501 titled 'Silver Polish' published in 1958 [27]. The author describes, the assembly mechanism,

chemical reaction, stabilizing factors, and minimum chain length to form a stable self-assembled monolayer (SAM) on silver.
In 1980, Sagiv showed the possibility of producing chemically attached monolayers on silicon dioxide. Three years later, Nuzzo and Allara exploited the chemical interaction between sulphur atoms and noble metal to fabricate SAMs on Au. [28,29]
After the discovery of alkanethiol assembly on gold, there was a rush of papers characterizing the surfaces of alkanethiol monolayers. Due to their easy processability, SAMs have been used on a wide variety of substrates including gold, silver, copper, nickel, platinum, palladium, mercury, zinc and cadmium selenide. Several analytical methods were successfully used like Raman, XPS, FTIR, helium atom scattering, X-ray diffraction, contact angle goniometry, ellipsometry, AFM, STM, etc.
Other early studies of thiol SAMs focused on the structure and assembly mechanism of single and dual component monolayers on gold. [30–34] These and other studies led to the well-characterized structure of alkanethiol SAMs shown in Fig. 1.7 [35]

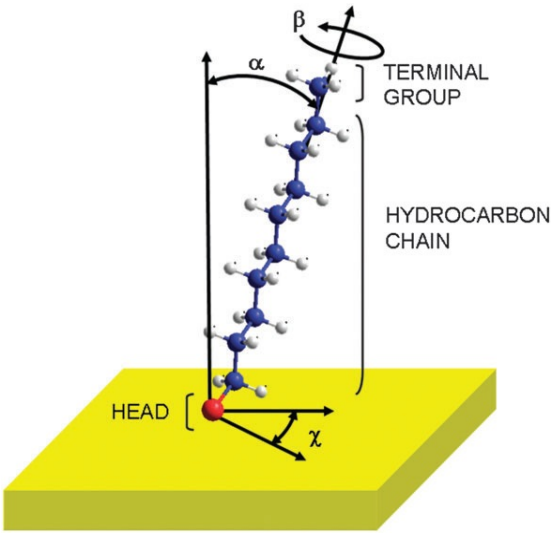

Fig. 1. 7 Scheme of decanethiol adsorbed on Au(111) (yellow) in a standing up configuration. Typical angles are α=30°, β=55° and χ=14°. Red: sulfur atom; blue: carbon atom; white: hydrogen atom.

Three main parts constitute the molecules: the head-group (linking group), the backbone (main chain) and the terminal (active) group. The head-group guides the self-assembly process on substrate, linking the hydrocarbon chain (of variable length) to the metal surface through a strong bond. The interactions among hydrocarbon chains (involving van der Waals and hydrophobic forces) ensure an efficient packing of the monolayer and contribute to stabilize the structures with increasing chain length. The terminal group confers specific properties to the surface (hydrophilic, hydrophobic), and can also be used to anchor different molecules, biomolecules or nanostructures by weak interactions or covalent bonds.
The SAM applications in nanotechnology are numerous and involve very different areas (Fig. 1.8).

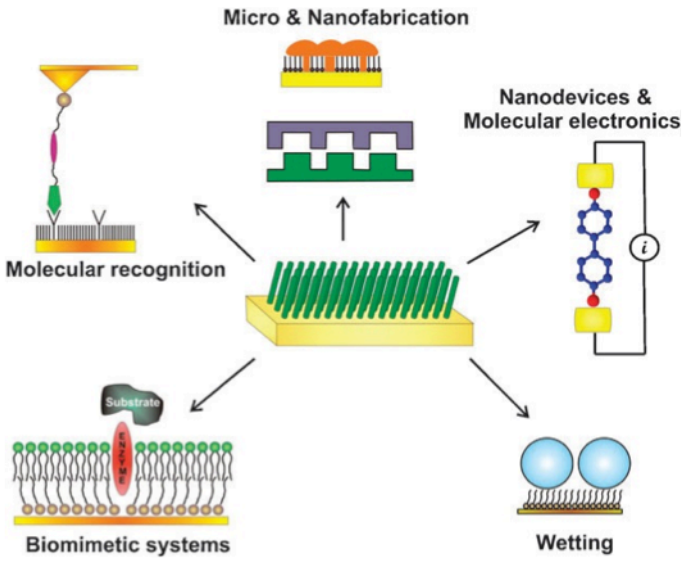

Fig. 1. 8 Some applications of self-assembled monolayer in nanotechnology.

Among them, they are used for stabilization and functionalization of nanosized objects (nanoparticles, nanorods and nanowires). Other important uses of SAMs are in the field of material protection, for instance the corrosion prevention [36–38], friction reduction, and anti-stiction coatings in MEMs fabrication [39]. In the area of device fabrication, SAMs are used as building blocks in sensors, biosensors, actuators, [40,41] and molecular motors. [42] They are also employed as active or passive elements in electronic devices, transistors and switches, and act as ‘‘nano-alligator clips’’ in single molecule circuits. [43] In nano/micro-fabrication, self-assembly molecules are employed as inks in micro-contact printing and dip pen lithography, as resists in photolithography and nano-shaving lithography, and as anti-adherent layers in nano-molding and nano-replication. [36,44] Within biological field and medicine, these molecules are used as building blocks for the design of biomolecule carriers, for bio-recognition assays, as coatings for implants, and as surface agents for changing cell and bacterial adhesion to surfaces [45,46]among many others uses. [36,47,48]

1.2.2 SAMs on oxides

SAMs of organosilane precursor ($RSiX_3$, with X= Cl, OMe and OEt) require hydroxylated surfaces as substrates for their formation including the technologically relevant surfaces of SiO_2, Al_2O_3 and tin-doped indium oxide (ITO). The driving force of this self-assembly resides on the *in-situ* formation of polysiloxane, which connects the precursor silane to the surface silanol (-Si-OH) groups via very strong Si-O-Si bonds.

High-quality SAMs of alkyltrichlorosilane derivatives require rigorous experimental conditions. The amount of water strongly affects the quality of the SAMs, because incomplete monolayers are formed in the total absence of water, [49,50] whereas excess of water leads uncontrolled polymerization in solution yielding polysiloxane-based stacks on the surface of interest. [51]

Fig. 1.9 illustrates the structure of commonly used silane precursors such as octyltrichlorosilane and octadecyltrichlorosilane (OTS and ODTS, respectively), 3-

mercaptopropyltrimethoxysilane (MPTMS), hexamethyildisilazane (HMDS) and various types of functionalized σ-π molecules.

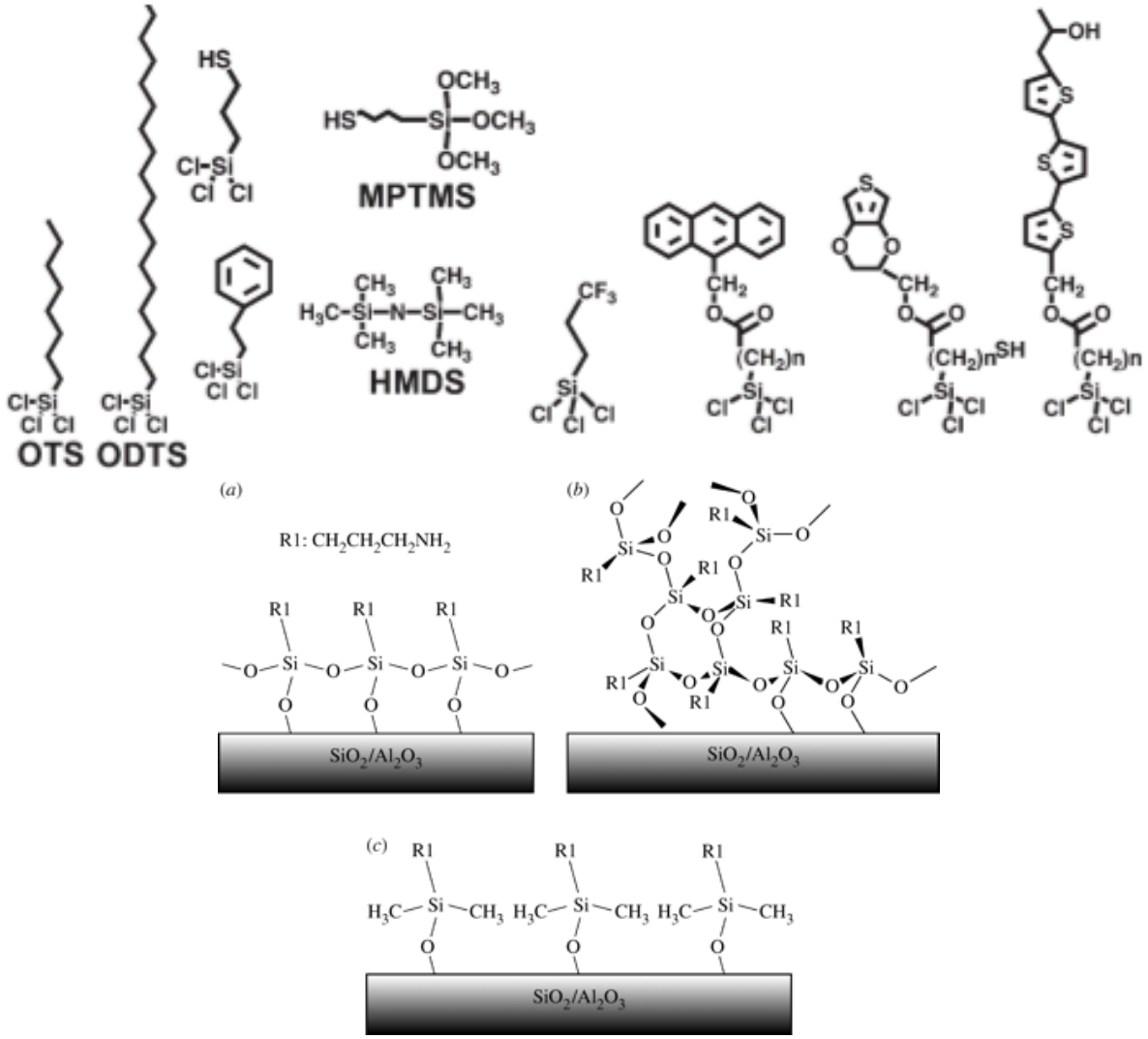

Fig. 1. 9 (top) Examples of silanes used for self-assembly on oxide surfaces [79]; (bottom) Schematics of (*a*) idealized APTES, (*b*) multilayered APTES and (*c*) idealized APDMES silane polymer films on silicon/SiO_2 and aluminium/Al_2O_3 substrates. Idealized film corresponds to a self-assembled monolayer.

The reproducibility of such kind of SAMs is still a problem, since the quality of the monolayer formed is very sensitive to experimental conditions, such as temperature. [52]

OTS and ODTS SAM formation on glass and silicon oxide are well documented in literature. Banga et al. [53] discover that OTS forms monolayers on mica by nucleating through isolated domains, whose fractal dimensions increase with increased surface coverage. Other studies on OTS growth onto siliconfirstly show large island and then the small voids are covered.

In 1998 Carraro et al. [54] elucidates the role of temperature in OTS growth-mode showing the existence of two critical temperature, θ_c and θ_d, defining three growth mode:

i) the expanded liquid (EL) mode, by formation of a homogeneous disordered monolayer, at high temperatures ($\theta > \theta_d$)

ii) the condensed liquid (CL) mode, by formation of dense and ordered islands, at low temperatures ($\theta < \theta_c$)

iii) the coexistence of those two growth modes (EL + CL) for intermediate temperatures ($\theta_c <$

$\theta < \theta_d$).
OTS is a widely known system but literature offers an exhaustive knowledge of the whole library of organosilane-based SAMs, because they are excellent coating layer and they are largely used in organic electronic.
Other classes of materials deposited on oxides surfaces include n-alkanoic acids and phosphonic acids. These compounds can form SAMs on different oxide surfaces like Al_2O_3, AgO, ITO and TiO_2 from both solvent and vapour deposition. [55]
Spontaneous adsorption of long-chain *n*-alkanoic acids ($C_nH_{2n+1}COOH$) involves an acid-base reaction, and the driving force is the formation of a interfacial salt between the carboxylate anion and a surface metal cation.
Organophosphonates and organophosphates are structurally similar (Fig. 1.10). These compounds have less rigorous conditions to be fulfilled with respect to organosilanes, thus it has attracted an ever-growing interest as an alternative to organosilane compounds.

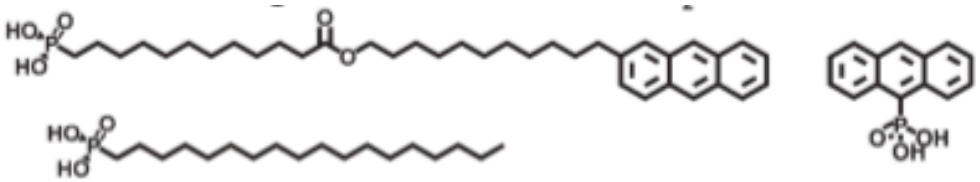

Fig. 1. 10 Examples of phosphonic acids used for self-assembly on oxide surfaces. [79]

Like thiols on gold, phosphonate-metal oxide SAMs form monolayers with a "tail-up" orientation and a tilt angle of the hydrocarbon chains of about 30° with respect to the surface normal.

1.2.3 SAMs on metals

The most extensively investigated types of SAMs are alkanethiols, $SH(CH_2)_nX$, on precious metal like gold, silver, platinum, copper and palladium. These compounds, such asthiols, disulphide and sulphide, spontaneously assemble upon exposure to the above-mentioned substrates. They are considered paradigm in terms of self-assembling blocks, which is commonly observed in a myriad of natural processes. The self-assembly is guided by the strong affinity of sulphur compounds toward transition metals that, as documented by Sellers, form multiple bonds with metal cluster. Despite the large number of organosulfur compounds, the most studied and most understood system remains the alkanethiolate monolayer on Au (111). Gold is largely employed as substrate materials because it is easy to deposit and pattern and it is relative inert to oxidation; the most common procedure for SAM formation require the immersion of the substrate in a dilute thiols solution for 12-18h.
These molecules form densely packed and well-ordered domains up to several hundred of nanometers following the scheme in Fig. 1.11.

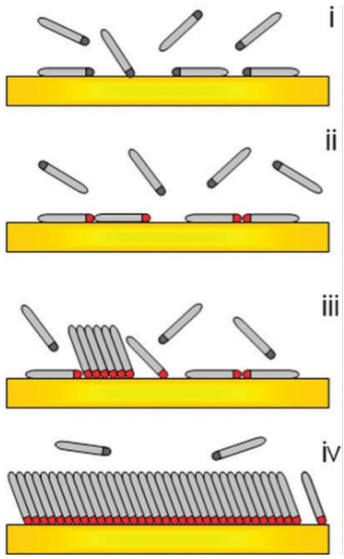

Fig. 1. 11 Scheme of the different steps taking place during the self-assembly of alkanethiol on Au(111): (i) physisorption,(ii) lying down phase formation, (iii) nucleation of standing up phase, (iv) completion of the standing up phase.

After physisorption, thiol molecules chemisorb on the Au(111) substrate through the S head-group, forming a strong covalent bond, in a process that takes at least some minutes. During the process, the thiol molecule loses the mercaptan H atom, transforming itself in a thiolate. We can describe the adsorption process as follows:

$$CH_3(CH_2)_nSH + Au \rightarrow (CH_3(CH_2)_nSH)_{phys}Au \qquad (1a)$$

$$(CH_3(CH_2)_nSH)_{phys}Au \rightarrow CH_3(CH_2)_nS{-}Au + 1/2H_2 \qquad (1b)$$

where reaction (1a) and (1b) correspond to thiol physisorption and chemisorption, respectively.

The nature and mechanism of reaction (1b) is not completely understood. It has been proposed that this reaction occurs via oxidative addition of RS–H bond to the metallic gold followed by a reductive elimination of the hydrogen. [32,55,56]

When a clean gold surface is used, the proton probably ends as a H_2 molecule. This can be deduced from the fact that monolayer can be formed from the gas phase [57–59] in the complete absence of oxygen:

$$R\text{-}S\text{-}H + Au_n^0 \qquad R\text{-}S^- Au^+ + Au_n^0 + 1/2H_2 \qquad (1c)$$

An extensive scientific literature confirmed an S-Au bond strength of 40 kcal mol^{-1} and a net energy for adsorption of alkanethiolates on gold of -5 kcal mol^{-1} (exothermic). [60]

Reaction (1c) was confirmed by detailed investigations and many analytical techniques like XPS, [31,61–63] Fourier transform infrared (FTIR) spectroscopy, [32] Fourier transform mass spectrometry, [64] electrochemistry, [65] and Raman spectroscopy [66,67], have demonstrated that the adsorbing species is the thiolates form (RS^-).

Scanning probe microscopy (SPM) including scanning tunneling microscopy (STM) [68–71] and atomic force microscopy (AFM), [72,73] have been widely used to probe the surface functionalized by alkanethiol and related monolayers on gold. Molecular scale images reveal that alkanethiol SAMs form a ($\sqrt{3}$ x $\sqrt{3}$) R30° hexagonal lattice compared to the underlying Au (111) surface. [74]

To minimize the free energy of the organic layer, the molecules adopt conformations that

allow high degrees of van der Waals interactions [75] (and in some cases hydrogen bonds [76–78]) with the neighbouring molecules;
Two parameters describe the variations in the orientation of the organic molecules in the SAM: the angle of tilt for the linear backbone of the molecule away from the surface normal (α) and the angle of rotation about the long axis of the molecule (β) (see Fig. 1.12).

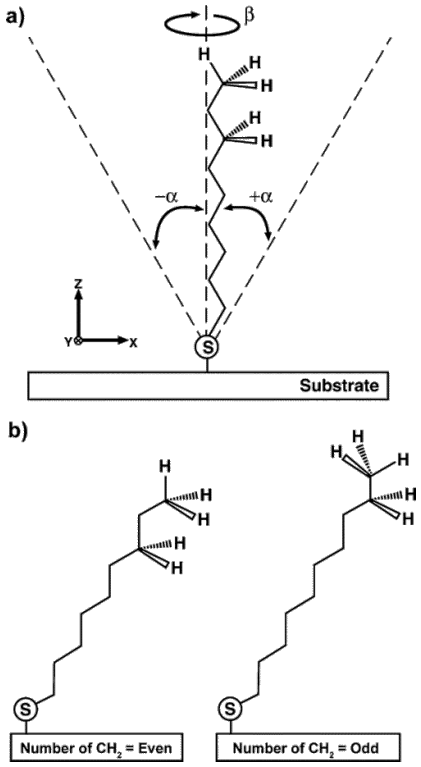

Fig. 1. 12 (a)Schematic view of an all-transconformer of a single, long-chain alkanethiolate adsorbed on a surface. The tilt angle (α) is defined with respect to the surface normal direction. The twist angle (β) describes the rotation of the CCC bond plane relative to the plane of the surface normal and the tilted chain. (b) Schematic views of single, long-chain alkanethiolates (with even and odd numbers of methylene groups) adsorbed on gold. The conserved value of R for each produces different projections of the terminal methyl group on the surface. [48]

For organothiolate SAM on gold α is equal to 30° and β lies near 50°.
The scheme usually found in literature where SAMs arranges onto a perfectly flat surface only depicts an idealized molecular assembly. Despite the gold-thiol bond being reasonably strong, the adsorbed alkanethiols still have the ability to move around of the gold surface. Different observations have confirmed this behaviour: first an exchange process occurs when a SAM-coated substrate is immersed in a different thiol solution [74] and second, thiols are able to heal gaps of exposed gold region due to their ability to diffuse across the surface.

1.2.4 SAMs applied to OTFT

Traditionally, OTFTs are fabricated using a thick SiO_x layer as gate dielectric and patterned gold contacts. Such devices usually suffer of poor stability, low charge carrier mobility and bias stress. Treatments of SiO_x dielectric with silane and phosponate SAMs had extensively studied in the past years for their beneficial influence on OTFTs performance. The control on the physical-chemical properties of the dielectric strongly influences the molecular

semiconductor/substrate interaction and affects thin-film morphology and the electronic properties of the semiconducting channel. [79]
This results in an improved device stability accompanied by the charge-carrier mobility, threshold voltage, sub-threshold slope and transfer characteristic hysteresis. [80]
A limiting drawback in OTFT operation is represented by the metal/semiconductor interface. In a real OFET the charge injection at this interface is non-ideal and is associated with a contact resistance R_c that arises from electronic and morphological effects: 1) the energy mismatch between the Fermi level of the metal and the HOMO/LUMO levels in the OS; 2) the structure and morphology of the OS at contact interfaces [81]; 3) a reduced electronic coupling across the interface.
One of the main effects of thiols SAMs on metal electrode is the alteration of the metal work function directly proportional to the surface dipole induced by the organic molecule.
The total work-function Φ of a metal surface is defined as the difference between the vacuum level at the surface V_{vac} and the Fermi level E_F of the metal, taken here as the zero energy level.

$$\Phi = V_{vac} - E_F \qquad \text{Eq. 1.2}$$

The SAM deposition has two consequences: (i) the ejected electron needs to overcome the additional potential step created by the dipolar molecular layer, ΔV_{vac}, to reach the vacuum level above the SAM; (ii) the bond formation between SAM and metal shifts the potential well of the SAM relative to E_F by BD. Thus the work function change can be decomposed into its contributing components [82]:

$$\Delta\Phi = \Delta V_{vac} + BD \qquad \text{Eq. 1.3}$$

where ΔV_{vac} is the potential energy change for the ejection of the electron and BD (bond dipole) is the potential energy shift due to the charge redistribution at the SAM/metal interface. The bond dipole is the step in potential energy at the interface and depends both on the docking chemistry between substrate and adsorbate and on the packing order of the monolayer itself. For the metal-thiols system, BD can be estimated as:

$$\Delta\rho = \rho_{SAM-met} - [\rho_{met} + (\rho_{SAM} - \rho_H)] \qquad \text{Eq. 1.4}$$

where $\rho_{SAM-met}$, ρ_{met}, ρ_{SAM} ρ_H are the plane averaged charge densities of the total SAM/metal system, the free gold surface and the free-standing radical SAM layer, the hydrogen atom that are removed upon adsorption, respectively. [82]
In a thin-film device the scenario is more complicated; in BG/BC device for example, OS isdeposited on polycrystalline gold electrodes coated with SAMs in a Metal/Insulator/Semiconductor (MIS) structure. Numerous studies have documented how SAM dipole moment ultimately mediates the charge conduction/injection at the metal/SAM/OS interface. [83–87]
SAMs of aliphatic chains are expected to be dielectric in nature otherwise SAMs of conjugated molecules are more widely used and there is an abundant literature on conduction mechanisms [88–91] and on charge transport in SAMs. [92–96]
Nonresonant tunnelling (through bonds) is the most common transport mechanism observed in molecular SAMs, [97] however for π-conjugated molecular SAMs, resonant tunneling (through the molecular orbitals) may also occur due to the smaller HOMO–LUMO gap. [98,99]
The simplest tunnelling model assumes a finite potential barrier at the metal–insulator interface and describes the finite probability for electrons to travel a short distance into the

SAM (or insulator) despite the lack of available energy levels. These processes are explained by the Simmons relation, which is expressed here in the simplest form for a rectangular barrier to demonstrate the exponential dependence of the current density (J_{DT}) on the thickness (d) and barrier height (ϕ) [92,95]

$$J_{DT} = \frac{q^2 V}{h^2 d}(2m\phi)^2 exp\left(\frac{-4\pi d}{h}(2m\phi)^{1/2}\right) \qquad \text{Eq. 1.5}$$

where q = electron charge, V = applied voltage, h = Planck's constant, and m= electron mass. At low voltages Eq. 1.5 can be simplified to $J_{DT} \propto \left(\frac{1}{d}\right) \exp(-\beta d)$ where the tunnelling decay parameter, β [100]

$$\beta = \frac{4\pi(2m\phi)}{h}\alpha \qquad \text{Eq. 1.6}$$

is accepted to be 0.6 Å^{-1} for saturated alkanes, and 0.2–0.6 Å^{-1} for conjugated molecules, and smaller β indicates more efficient tunnelling. [96]

α here is a unitless parameter indicating the symmetry of the potential profile (α is equal to 1 for rectangular barrier). Another interpretation considers the charge transport through SAM a thermally activated process. For a simple hopping, current density J, follow a classical Arrhenius relation: [91,101]

$$\sigma = \sigma_0 exp\left(\frac{-E_a}{kT}\right) \qquad \text{Eq. 1.7}$$

Despite the less frequent demonstrations of hopping transport in SAM compared to tunnelling, in this occasion the typical length investigated was greater than ≈2 nm. [102–104] Therefore theoretical works supported a transition between these transport mechanisms. Recently this transition was demonstrated in Au-molecule-Au junctions, where the electrical resistance of oligophenyleneimine (OPI) molecules of various lengths were measured with a conductive AFM tip. [105] Hopping transport was found in OPI molecules longer than 4nm, while molecules <4nm in length exhibited nonresonant tunnelling.

Chapter 3 is focused on OFETs in a BG/BC configuration where metal S/D electrodes are coated with different SAMs. This extensive study was performed with different kind of SAM differing in length or in terminal/anchoring groups and by monitoring current performances. It has been highlighted the role of SAM in these devices. Varying the molecular length of the charge injection barrier, we extracted different exponential decay factors of mobility and current density for different homologous set of molecules. These values are in good agreement with other techniques, such as scanning probe microscopy, nano-pores structures, hanging mercury drop, large-area molecular junctions etc.

References:

[1] H. Letheby, XXIX.-On the production of a blue substance by the electrolysis of sulphate of aniline, J. Chem. Soc. 15 (1862) 161–163.

[2] R.G. Harvey, Polycyclic Aromatic Hydrocarbons, Wiley-VCH: New York, 1997.

[3] R. McNeill, R. Siudak, J.H. Wardlaw, D.E. Weiss, Electronic Conduction in Polymers. I. The Chemical Structure of Polypyrrole, Aust. J. Chem. 16 (1963) 1056–1075.

[4] B.A. Bolto, D.E. Weiss, Electronic conduction in polymers. II. The electrochemical reduction of polypyrrole at controlled potential, Aust. J. Chem. (1963).

[5] B.A. Bolto, R. McNeill, D.E. Weiss, Electronic Conduction in Polymers. III. Electronic Properties of Polypyrrole, Aust. J. Chem. 16 (1963) 1090–1103.

[6] J. McGinness, P. Corry, P. Proctor, Amorphous Semiconductor Switching in Melanins, Sci. . 183 (1974) 853–855.

[7] A.J. Heeger, A.G. MacDiarmid, H. Shirakawa, The Nobel Prize in Chemistry 2000: Conductive Polymers, (2000).

[8] F. Ebisawa, T. Kurokawa, S. Nara, Electrical properties of polyacetylene/polysiloxane interface, J. Appl. Phys. 54 (1983).

[9] M. Pope, C.E. Swenberg, Electronic processes in organic crystals, Clarendon Press Oxford, 1982.

[10] A. Tsumura, H. Koezuka, T. Ando, Macromolecular electronic device: Field-effect transistor with a polythiophene thin film, Appl. Phys. Lett. 49 (1986).

[11] C.W. Tang, Two-layer organic photovoltaic cell, Appl. Phys. Lett. 48 (1986).

[12] C.W. Tang, S.A. VanSlyke, Organic electroluminescent diodes, Appl. Phys. Lett. 51 (1987).

[13] C.D. Sheraw, L. Zhou, J.R. Huang, D.J. Gundlach, T.N. Jackson, M.G. Kane, et al., Organic thin-film transistor-driven polymer-dispersed liquid crystal displays on flexible polymeric substrates, Appl. Phys. Lett. 80 (2002).

[14] J.A. Rogers, Z. Bao, K. Baldwin, A. Dodabalapur, B. Crone, V.R. Raju, et al., Paper-like electronic displays: Large-area rubber-stamped plastic sheets of electronics and microencapsulated electrophoretic inks, Proc. Natl. Acad. Sci. . 98 (2001) 4835–4840.

[15] Z.-T. Zhu, J.T. Mason, R. Dieckmann, G.G. Malliaras, Humidity sensors based on pentacene thin-film transistors, Appl. Phys. Lett. 81 (2002) 4643.

[16] D. Voss, Cheap and cheerful circuits, Nature. 407 (2000) 442–444.

[17] C.D. Dimitrakopoulos, P.R.L. Malenfant, Organic Thin Film Transistors for Large Area Electronics, Adv. Mater. 14 (2002) 99–117.

[18] H. Sirringhaus, Device Physics of Solution-Processed Organic Field-Effect Transistors, Adv. Mater. 17 (2005) 2411–2425.

[19] F. Amy, C. Chan, A. Kahn, Polarization at the gold/pentacene interface, Org. Electron. 6 (2005) 85–91.

[20] M.J. Małachowski, J. Żmija, Organic field-effect transistors, Opto-Electronics Rev. 18 (2010) 121–136.

[21] W. Brütting, Physics of organic semiconductors, John Wiley & Sons, 2006.

[22] I. Kymissis, Organic Field Effect Transistors: Theory, Fabrication and Characterization, Springer, 2008.

[23] Z. Bao, J. Locklin, Organic Field-Effect Transistors, CRC Press, Boca Raton, 2007.

[24] F.-J. Meyer zu Heringdorf, M.C. Reuter, R.M. Tromp, Growth dynamics of pentacene thin films, Nature. 412 (2001) 517–520.

[25] Y.-Y. Lin, D.J. Gundlach, S.F. Nelson, T.N. Jackson, Stacked pentacene layer organic thin-film transistors with improved characteristics, Electron Device Lett. IEEE. 18 (1997) 606–608.

[26] W.C. Bigelow, D.L. Pickett, W.A. Zisman, Oleophobic monolayers: I. Films adsorbed from solution in non-polar liquids, J. Colloid Sci. 1 (1946) 513–538.

[27] J.G. Murphy, Silver Polish, 1958.

[28] J. Sagiv, Organized monolayers by adsorption. 1. Formation and structure of oleophobic mixed monolayers on solid surfaces, J. Am. Chem. Soc. 102 (1980) 92–98.

[29] R.G. Nuzzo, D.L. Allara, Adsorption of bifunctional organic disulfides on gold surfaces, J. Am. Chem. Soc. 105 (1983) 4481–4483.

[30] C.D. Bain, E.B. Troughton, Y.T. Tao, J. Evall, G.M. Whitesides, R.G. Nuzzo, Formation of monolayer films by the spontaneous assembly of organic thiols from solution onto gold, J. Am. Chem. Soc. 111 (1989) 321–335.

[31] R.G. Nuzzo, F.A. Fusco, D.L. Allara, Spontaneously organized molecular assemblies. 3. Preparation and properties of solution adsorbed monolayers of organic disulfides on gold surfaces, J. Am. Chem. Soc. 109 (1987) 2358–2368.

[32] R.G. Nuzzo, B.R. Zegarski, L.H. Dubois, Fundamental studies of the chemisorption of organosulfur compounds on gold(111). Implications for molecular self-assembly on gold surfaces, J. Am. Chem. Soc. 109 (1987) 733–740.

[33] C.D. Bain, J. Evall, G.M. Whitesides, Formation of monolayers by the coadsorption of thiols on gold: variation in the head group, tail group, and solvent, J. Am. Chem. Soc. 111 (1989) 7155–7164.

[34] C.D. Bain, G.M. Whitesides, Formation of monolayers by the coadsorption of thiols on gold: variation in the length of the alkyl chain, J. Am. Chem. Soc. 111 (1989) 7164–7175.

[35] G.E. Poirier, M.J. Tarlov, H.E. Rushmeier, Two-Dimensional Liquid Phase and the px.sqroot.3 Phase of Alkanethiol Self-Assembled Monolayers on Au(111), Langmuir. 10 (1994) 3383–3386.

[36] O. Azzaroni, M. Cipollone, M.E. Vela, R.C. Salvarezza, Protective Properties of Dodecanethiol Layers on Copper Surfaces: The Effect of Chloride Anions in Aqueous Environments, Langmuir. 17 (2001) 1483–1487.

[37] G. Brunoro, A. Frignani, A. Colledan, C. Chiavari, Organic films for protection of copper and bronze against acid rain corrosion, Corros. Sci. 45 (2003) 2219–2231.

[38] C.M. Whelan, M. Kinsella, L. Carbonell, H.M. Ho, K. Maex, Corrosion inhibition by self-assembled monolayers for enhanced wire bonding on Cu surfaces, Microelectron. Eng. 70 (2003) 551–557.

[39] R. Maboudian, W.R. Ashurst, C. Carraro, Self-assembled monolayers as anti-stiction coatings for MEMS: characteristics and recent developments, Sensors Actuators A Phys. 82 (2000) 219–223.

[40] Y. Wang, Y. Zhou, J. Sokolov, B. Rigas, K. Levon, M. Rafailovich, A potentiometric protein sensor built with surface molecular imprinting method, Biosens. Bioelectron. 24 (2008) 162–166.

[41] H. Chen, C.K. Heng, P.D. Puiu, X.D. Zhou, A.C. Lee, T.M. Lim, et al., Detection of Saccharomyces cerevisiae immobilized on self-assembled monolayer (SAM) of alkanethiolate using electrochemical impedance spectroscopy, Anal. Chim. Acta. 554 (2005) 52–59.

[42] T.J. Huang, B. Brough, C.-M. Ho, Y. Liu, A.H. Flood, P.A. Bonvallet, et al., A nanomechanical device based on linear molecular motors, Appl. Phys. Lett. 85 (2004).

[43] L. Venkataraman, J.E. Klare, C. Nuckolls, M.S. Hybertsen, M.L. Steigerwald, Dependence of single-molecule junction conductance on molecular conformation, Nature. 442 (2006) 904–907.

[44] J.A. Rogers, R.G. Nuzzo, Recent progress in soft lithography, Mater. Today. 8 (2005) 50–56.

[45] X. Jiang, D.A. Bruzewicz, A.P. Wong, M. Piel, G.M. Whitesides, Directing cell migration with asymmetric micropatterns, Proc. Natl. Acad. Sci. United States Am. . 102 (2005) 975–978.

[46] S. Takeuchi, W.R. DiLuzio, D.B. Weibel, G.M. Whitesides, Controlling the Shape of Filamentous Cells of Escherichia coli, Nano Lett. 5 (2005) 1819–1823.

[47] J.L. Wilbur, G.M. Whitesides, Self-assembly and self-assembled monolayers in micro-and nanofabrication, in: Nanotechnology, Springer, 1999: pp. 331–369.

[48] J.C. Love, L.A. Estroff, J.K. Kriebel, R.G. Nuzzo, G.M. Whitesides, Self-Assembled Monolayers of Thiolates on Metals as a Form of Nanotechnology, Chem. Rev. 105 (2005) 1103–1170.

[49] S.R. Wasserman, Y.T. Tao, G.M. Whitesides, Structure and reactivity of alkylsiloxane monolayers formed by reaction of alkyltrichlorosilanes on silicon substrates, Langmuir. 5 (1989) 1074–1087.

[50] J.D. Le Grange, J.L. Markham, C.R. Kurkjian, Effects of surface hydration on the deposition of silane monolayers on silica, Langmuir. 9 (1993) 1749–1753.

[51] S. Brandriss, S. Margel, Synthesis and characterization of self-assembled hydrophobic monolayer coatings on silica colloids, Langmuir. 9 (1993) 1232–1240.

[52] S. Desbief, L. Patrone, D. Goguenheim, D. Guérin, D. Vuillaume, Impact of chain length, temperature, and humidity on the growth of long alkyltrichlorosilane self-assembled monolayers., Phys. Chem. Chem. Phys. 13 (2011) 2870–9.

[53] R. Banga, J. Yarwood, A.M. Morgan, B. Evans, J. Kells, FTIR and AFM Studies of the Kinetics and Self-Assembly of Alkyltrichlorosilanes and (Perfluoroalkyl)trichlorosilanes onto Glass and Silicon, Langmuir. 11 (1995) 4393–4399.

[54] C. Carraro, O.W. Yauw, M.M. Sung, R. Maboudian, Observation of Three Growth Mechanisms in Self-Assembled Monolayers, J. Phys. Chem. B. 102 (1998) 4441–4445.

[55] A. Ulman, Formation and Structure of Self-Assembled Monolayers, Chem. Rev. 96 (1996) 1533–1554.

[56] C. Vericat, M.E. Vela, G. Benitez, P. Carro, R.C. Salvarezza, Self-assembled monolayers of thiols and dithiols on gold: new challenges for a well-known system, Chem. Soc. Rev. 39 (2010) 1805–1834.

[57] M. Brust, M. Walker, D. Bethell, D.J. Schiffrin, R. Whyman, Synthesis of thiol-derivatised gold nanoparticles in a two-phase Liquid-Liquid system, J. Chem. Soc.{,} Chem. Commun. (1994) 801–802.

[58] R.C. Thomas, L. Sun, R.M. Crooks, A.J. Ricco, Real-time measurements of the gas-phase adsorption of n-alkylthiol mono- and multilayers on gold, Langmuir. 7 (1991) 620–622.

[59] O. Chailapakul, L. Sun, C. Xu, R.M. Crooks, Interactions between organized, surface-confined monolayers and vapor-phase probe molecules. 7. Comparison of self-assembling n-alkanethiol monolayers deposited on gold from liquid and vapor phases, J. Am. Chem. Soc. 115 (1993) 12459–12467.

[60] L.H. Dubois, B.R. Zegarski, R.G. Nuzzo, Molecular ordering of organosulfur compounds on Au(111) and Au(100): Adsorption from solution and in ultrahigh vacuum, J. Chem. Phys. 98 (1993).

[61] M.M. Walczak, C. Chung, S.M. Stole, C.A. Widrig, M.D. Porter, Structure and interfacial properties of spontaneously adsorbed n-alkanethiolate monolayers on evaporated silver surfaces, J. Am. Chem. Soc. 113 (1991) 2370–2378.

[62] M.D. Porter, T.B. Bright, D.L. Allara, C.E.D. Chidsey, Spontaneously organized molecular assemblies. 4. Structural characterization of n-alkyl thiol monolayers on gold by optical ellipsometry, infrared spectroscopy, and electrochemistry, J. Am. Chem. Soc. 109 (1987) 3559–3568.

[63] C.D. Bain, H.A. Biebuyck, G.M. Whitesides, Comparison of self-assembled monolayers on gold: coadsorption of thiols and disulfides, Langmuir. 5 (1989) 723–727.

[64] R.G. Nuzzo, L.H. Dubois, D.L. Allara, Fundamental studies of microscopic wetting on organic surfaces. 1. Formation and structural characterization of a self-consistent series of polyfunctional organic monolayers, J. Am. Chem. Soc. 112 (1990) 558–569.

[65] Y. Li, J. Huang, R.T. McIver, J.C. Hemminger, Characterization of thiol self-assembled films by laser desorption Fourier transform mass spectrometry, J. Am. Chem. Soc. 114 (1992) 2428–2432.

[66] C.A. Widrig, C. Chung, M.D. Porter, The electrochemical desorption of n-alkanethiol monolayers from polycrystalline Au and Ag electrodes, J. Electroanal. Chem. Interfacial Electrochem. 310 (1991) 335–359.

[67] M.A. Bryant, J.E. Pemberton, Surface Raman scattering of self-assembled monolayers formed from 1-alkanethiols: behavior of films at gold and comparison to films at silver, J. Am. Chem. Soc. 113 (1991) 8284–8293.

[68] L. Häussling, B. Michel, H. Ringsdorf, H. Rohrer, Direct Observation of Streptavidin Specifically Adsorbed on Biotin-Functionalized Self-Assembled Monolayers with the Scanning Tunneling Microscope, Angew. Chemie Int. Ed. English. 30 (1991) 569–572.

[69] C.A. Widrig, C.A. Alves, M.D. Porter, Scanning tunneling microscopy of ethanethiolate and n-octadecanethiolate monolayers spontaneously absorbed at gold surfaces, J. Am. Chem. Soc. 113 (1991) 2805–2810.

[70] C. Schoenenberger, J.A.M. Sondag-Huethorst, J. Jorritsma, L.G.J. Fokkink, What Are the "Holes" in Self-Assembled Monolayers of Alkanethiols on Gold?, Langmuir. 10 (1994) 611–614.

[71] R. Yamada, H. Wano, K. Uosaki, Effect of Temperature on Structure of the Self-Assembled Monolayer of Decanethiol on Au(111) Surface, Langmuir. 16 (2000) 5523–5525.

[72] G. Liu, M.B. Salmeron, Reversible Displacement of Chemisorbed n-Alkanethiol Molecules on Au(111) Surface: An Atomic Force Microscopy Study, Langmuir. 10 (1994) 367–370.

[73] K. Tamada, M. Hara, H. Sasabe, W. Knoll, Surface Phase Behavior of n-Alkanethiol Self-Assembled Monolayers Adsorbed on Au(111): An Atomic Force Microscope Study, Langmuir. 13 (1997) 1558–1566.

[74] G.E. Poirier, Characterization of Organosulfur Molecular Monolayers on Au(111) using Scanning Tunneling Microscopy, Chem. Rev. 97 (1997) 1117–1128.

[75] J.P. Bareman, M.L. Klein, Collective tilt behavior in dense, substrate-supported monolayers of long-chain molecules: a molecular dynamics study, J. Phys. Chem. 94 (1990) 5202–5205.

[76] M.K. Ferguson, E.R. Low, J.R. Morris, Well-Ordered Self-Assembled Monolayers Created via Vapor-Phase Reactions on a Monolayer Template, Langmuir. 20 (2004) 3319–3323.

[77] M.C. Gurau, G. Kim, S.-M. Lim, F. Albertorio, H.C. Fleisher, P.S. Cremer, Organization of Water Layers at Hydrophilic Interfaces, ChemPhysChem. 4 (2003) 1231–1233.

[78] R. Valiokas, M. Östblom, S. Svedhem, S.C.T. Svensson, B. Liedberg, Thermal Stability of Self-Assembled Monolayers: Influence of Lateral Hydrogen Bonding, J. Phys. Chem. B. 106 (2002) 10401–10409.

[79] S.A. DiBenedetto, A. Facchetti, M.A. Ratner, T.J. Marks, Molecular Self-Assembled Monolayers and Multilayers for Organic and Unconventional Inorganic Thin-Film Transistor Applications, Adv. Mater. 21 (2009) 1407–1433.

[80] K. Asadi, Y. Wu, F. Gholamrezaie, P. Rudolf, P.W.M. Blom, Single-Layer Pentacene Field-Effect Transistors Using Electrodes Modified With Self-assembled Monolayers, Adv. Mater. 21 (2009) 4109–4114.

[81] A. Kahn, N. Koch, W. Gao, Electronic Structure and Electrical Properties of Interfaces between Metals and π-Conjugated Molecular Films, J. Polym. Sci. Part B Polym. Physicslymer Sci. 41 (2003) 2529–2548.

[82] G. Heimel, L. Romaner, E. Zojer, J.-L. Bredas, The interface energetics of self-assembled monolayers on metals., Acc. Chem. Res. 41 (2008) 721–9.

[83] O. Gershewitz, M. Grinstein, C.N. Sukenik, K. Regev, J. Ghabboun, Cahen, Effect of Molecule−Molecule Interaction on the Electronic Properties of Molecularly Modified Si/SiOx Surfaces, J. Phys. Chem. B. 108 (2004) 664–672.

[84] Y.-J. Liu, H.-Z. Yu, Alkyl Monolayer Passivated Metal–Semiconductor Diodes: 2: Comparison with Native Silicon Oxide, ChemPhysChem. 4 (2003) 335–342.

[85] A. Scott, D.B. Janes, C. Risko, M.A. Ratner, Fabrication and characterization of metal-molecule-silicon devices, Appl. Phys. Lett. 91 (2007) -.

[86] S. Lenfant, C. Krzeminski, C. Delerue, G. Allan, D. Vuillaume, Molecular Rectifying Diodes from Self-Assembly on Silicon, Nano Lett. 3 (2003) 741–746.

[87] Kim, J.M. Beebe, Y. Jun, X.-Y. Zhu, C.D. Frisbie, Correlation between HOMO Alignment and Contact Resistance in Molecular Junctions: Aromatic Thiols versus Aromatic Isocyanides, J. Am. Chem. Soc. 128 (2006) 4970–4971.

[88] E.A. Weiss, R.C. Chiechi, G.K. Kaufman, J.K. Kriebel, Z. Li, M. Duati, et al., Influence of Defects on the Electrical Characteristics of Mercury-Drop Junctions: Self-Assembled Monolayers of n-Alkanethiolates on Rough and Smooth Silver, J. Am. Chem. Soc. 129 (2007) 4336–4349.

[89] J.J. O'Dwyer, The theory of electrical conduction and breakdown in solid dielectrics, Clarendon Press Oxford, 1973.

[90] J.G. Simmons, Conduction in thin dielectric films, J. Phys. D. Appl. Phys. 4 (1971) 613.

[91] S.M. Sze, K.K. Ng, Physics of semiconductor devices, John Wiley & Sons, 2006.

[92] D.K. Aswal, S. Lenfant, D. Guerin, J. V Yakhmi, D. Vuillaume, Self assembled monolayers on silicon for molecular electronics, Anal. Chim. Acta. 568 (2006) 84–108.

[93] M.L. Chabinyc, X. Chen, R.E. Holmlin, H. Jacobs, H. Skulason, C.D. Frisbie, et al., Molecular Rectification in a Metal−Insulator−Metal Junction Based on Self-Assembled Monolayers, J. Am. Chem. Soc. 124 (2002) 11730–11736.

[94] H.B. Akkerman, B. de Boer, Electrical conduction through single molecules and self-assembled monolayers, J. Phys. Condens. Matter. 20 (2008) 013001.

[95] R.L. McCreery, Molecular Electronic Junctions, Chem. Mater. 16 (2004) 4477–4496.

[96] A. Salomon, D. Cahen, S. Lindsay, J. Tomfohr, V.B. Engelkes, C.D. Frisbie, Comparison of Electronic Transport Measurements on Organic Molecules, Adv. Mater. 15 (2003) 1881–1890.

[97] B. Ulgut, H.D. Abruña, Electron Transfer through Molecules and Assemblies at Electrode Surfaces, Chem. Rev. 108 (2008) 2721–2736.

[98] A. Nitzan, M.A. Ratner, Electron Transport in Molecular Wire Junctions, Sci. . 300 (2003) 1384–1389.

[99] H.B. Akkerman, P.W.M. Blom, D.M. de Leeuw, B. de Boer, Towards molecular electronics with large-area molecular junctions., Nature. 441 (2006) 69–72.

[100] W. Wang, T. Lee, M. Reed, Mechanism of electron conduction in self-assembled alkanethiol monolayer devices, Phys. Rev. B. 68 (2003) 035416.

[101] N.I. Craciun, J. Wildeman, P.W.M. Blom, Universal Arrhenius Temperature Activated Charge Transport in Diodes from Disordered Organic Semiconductors, Phys. Rev. Lett. 100 (2008) 56601.

[102] E. Tran, C. Grave, G.M. Whitesides, M.A. Rampi, Controlling the electron transfer mechanism in metal–molecules–metal junctions, Electrochim. Acta. 50 (2005) 4850–4856.

[103] Y. Selzer, M.A. Cabassi, T.S. Mayer, D.L. Allara, Temperature effects on conduction through a molecular junction, Nanotechnology. 15 (2004) S483.

[104] D. Segal, A. Nitzan, M. Ratner, W.B. Davis, Activated Conduction in Microscopic Molecular Junctions, J. Phys. Chem. B. 104 (2000) 2790–2793.

[105] S. Ho Choi, B. Kim, C.D. Frisbie, Electrical Resistance of Long Conjugated Molecular Wires, Sci. . 320 (2008) 1482–1486.

Materials and experimental methods

2

In this chapter, all the materials and techniques used in the thesis are reported. Paragraphs 2.1, 2.2 and 2.3 discuss substrates, devices and organic semiconductor films. The last paragraph 2.4 describes the basics of each technique for characterizing surfaces and/or devices.

2.1 Substrates and Materials

For the thesis work, two kinds of devices have been used: i) transistors integrated on test patterns manufactured by FBK (Fondazione Bruno Kessler, Trento, Italy) [1], ii) prototype devices designed for the electrolyte-gated measurements of chapter 4. A brief description is given below.

2.1.1 Standard Test Pattern (TP)

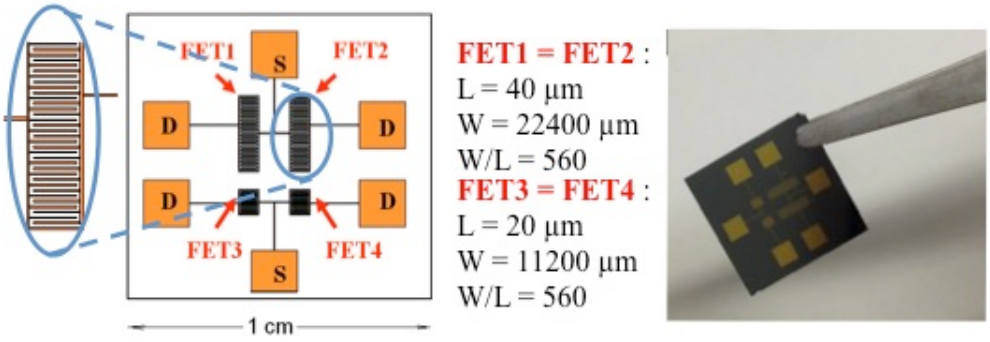

Fig. 2.1 Schematic layout of standard FBK test pattern used in our experiments; A1, B1, A2, B2 are the 4 active devices. The inset zooms out the interdigitated electrodes. (left); photograph of FBK test pattern (right).

Test patterns (TPs) are fabricated on Si <100> n-type (Sb-doped), 500 µm thick, with a resistivity of 0.01– 0.03 Ω x cm. The dielectric layer is 200 nm thick thermal SiO_2 (17.25 nF/cm^2). Au electrodes (125 ± 25 nm thick) are photolithographically patterned as interdigitated fingers onto SiO_2 by means of a chromium adhesive layer (3–5 nm).
Four transistors are available on each test pattern; two of them have channel width (*W*) and length (*L*) equal to 22400 µm and 20 µm respectively; the others maintain the same geometrical ratio (*W*/*L* equal to 560) with doubled rule, as shown in Fig. 2.1.
Prior to semiconductor deposition, TPs were cleaned with a standard procedure that involves the following three steps: (i) the removal of organic photoresist by rinsing with acetone, (ii) the elimination of organic contaminants by immersing the substrate in piranha solution (H_2SO_4:H_2O_2, 1:1) for 15 min and (iii) the flattening of the SiO_2 dielectric by dipping in HF 2% *v/v* solution for 5 seconds.

2.1.2 Prototype Test Pattern for EGOFET measurements

As reported in Chapter 4.3, electrolyte-gated measurements were performed using a prototype devices (see Fig.2.2a and Fig.2.2b) fabricated in our laboratory, starting from gold covered quartz slides (Phasis, Geneve; 50 nm of Au and 7 nm Ti as adhesion layer) [2]. Source and drain electrodes were patterned by laser ablation with a pulsed IR-laser (λ= 1064 nm) of the *ScribaR* Scriba Nanotecnologie S.r.l. (see Fig.2.2c)[3] laser scan machine. Best sensitivity and stability of the devices were obtained with layouts featuring an interdigitated structure of *W* of 27000 µm and *L* of 15 µm (*W*/*L* ratio of 1800).

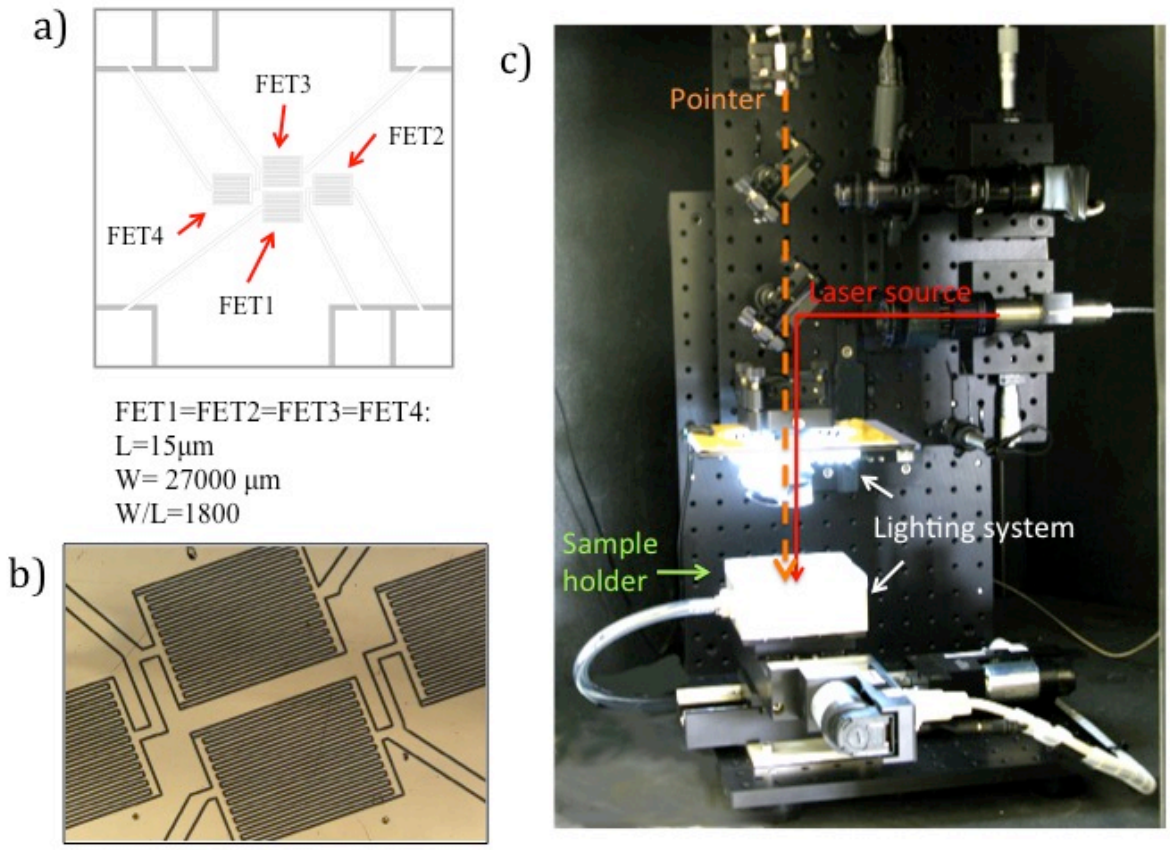

Fig. 2.2 a) Technical drawing of our prototype test pattern; b) Optical view of interdigitated structure; c) Photograph of *ScribaR* laser scan machine.

2.1.3 Gold standard substrate

Contact angle measurements were performed on standard gold thin films modified by SAMs . Such surfaces are purchased by Arrandee™ and they consist of a borosilicate glass (0.7 ± 0.1 mm) with a chromium layer (2.5 ± 1.5 nm) that ensures good adhesion of the top gold layer (250 ± 50 nm). [4]

2.1.4 Self- Assembled Monolayers (SAMs) protocol.

The use of SAMs integrated into organic electronic devices is presented in Chapter 3. The chemical backbone of the five sets of molecules are shown in Fig. 2.3. Commercial SAMs are purchased from Sigma-Aldrich and used without further purification. The Au functionalization was obtained by immersing the sample in 1 mM ethanol solution for 72h. The homolog series of oligothiophene SAM described in chapter 3 was synthesized by the group of Prof. S. Destri and W. Porzio at ISMAC-CNR, Milan [5,6]. The mono- and bi-dentate oligoarylenes (with the following acronyms TD, TBM, TBD, MTM, MTD, NTD and NTM) were synthesized by the group of Prof. G. Farinola of University of Bari [7–11]. These non-commercial SAMs are prepared as 0.1 mM solution with dichloromethane as solvent and the immersion time was 72h to yield a complete coverage of the gold surfaces.

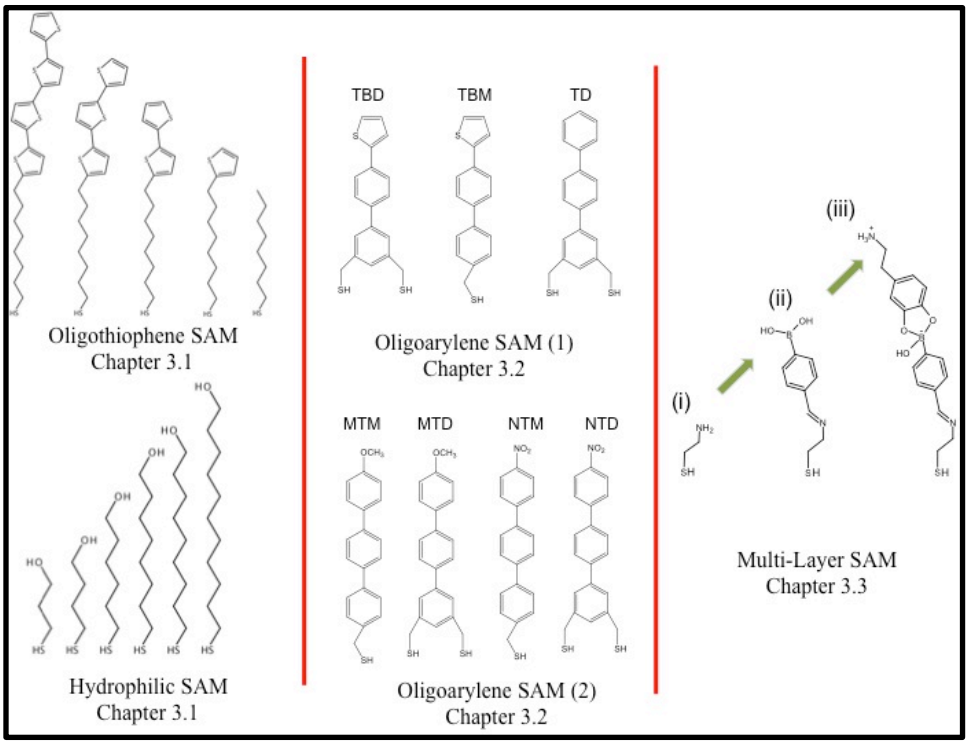

Fig. 2.3 Self-Assembled Monolayers presented in Chapter 3

The last part of chapter 3 is dedicated to a particular SAM composed by cysteamine (CA), 4-formilphenyl boronic (BA) and dopamine (DA). All the products are purchased from Sigma-Aldrich and the formation of this multi-layer SAM requires three functionalization steps: (i) the adsorption of CA on gold, (ii) the esterification of the boronic acid due to a Schiff's base formation and (iii) the dopamine condensation. The protocol was electrochemically verified by Shervedani R. K. *et al.* [12][13].

2.1.5 Semiconductor deposition

Semiconductor is the active component in an OFET device. Here two p-channel semiconductor materials are used: pentacene and P3HT, their chemical structures are shown in Fig. 2.4.

Pentacene

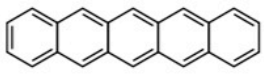

Properties
Molecular formula: $C_{22}H_{14}$
Molar mass: 278.36 g/mol
Appearance: dark powder
Density: 1.3 g/cm3
Melting point: >300°C; sublimes at 372°C

Poly(3-hexylthiophene-2,5-diyl)
P3HT

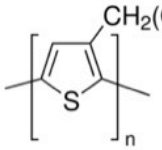

Properties
Molecular formula: $(C_{10}H_{14}S)_n$
Mol wt: average M_n 15.000-45.000 g/mol
Description: >98% head-to-tail regioregular, electronic grade.
Appearance: solid
M_w/M_n = <2.5
Melting point: 238°C

Fig. 2.4 Organic Semiconductor employed for OFET fabrication.

Pentacene was purchased from Sigma-Aldrich (*684848 Aldrich*) and it was deposited by vacuum sublimation at a pressure of 10^{-8} mbar at constant rate of 7.5 Å/min (nominally ½ ML/min) up to a thickness of 15 nm (10ML). Regio-regular poly-(3-hexyl-thiophene) (P3HT) was purchased from Sigma Aldrich (*698989 Aldrich*) and used without further purification. The molecular weight was

between 15000 and 45000 g/mol and the regio-regularity was >98%. P3HT was spin-coated from dichlorobenzene, with a concentration of typically 10mg/ml. The resulting film thickness was between 50 nm and 100nm depending on the concentration and spin-coating speed., The transistors were subsequently annealed at 150° for 1 hour, in order to remove any remaining solvent.

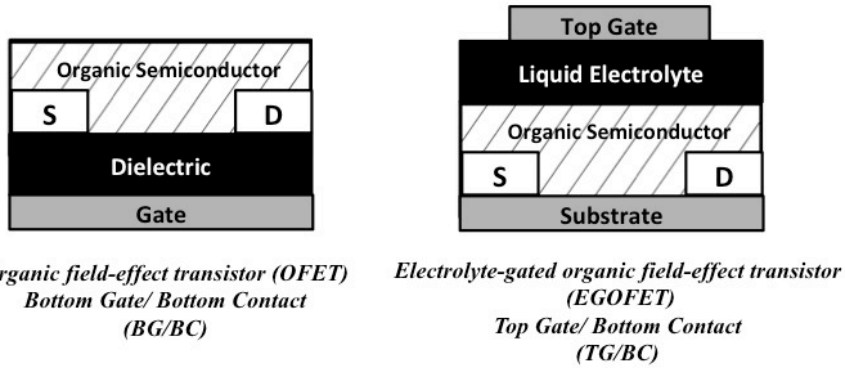

Fig. 2.5 OFET layouts; the standard bottom gate/bottom contact configuration on the left, top gate configuration for liquid measurements on the right.

2.2 Characterization techniques

2.2.1 Electrical measurements setup

The OFETs characterizations were performed in bottom gate/bottom contact configuration both in air and in vacuum (10^{-4} mbar). All the measurements in chapter 4 were performed in liquid with a top gate/bottom contact configuration, as depicted in Fig.2.5. The top gate is a polycrystalline Au wire placed in contact with a phosphate buffer (PBS) solution (100mM) that acts as electrolyte and it ensures electrical connection between gate electrode and the semiconductor channel. A plastic pool guarantees the confinement of the electrolyte as well as a better control of the volume.

The electrical characterization of OFET takes advantage of a home-built system, capable to perform vacuum measurements. All parts of this system were entirely designed and assembled at the CNR-ISMN laboratories, and some critical components were manufactured in CNR machine shop. The system is shown in Fig.2.6 (left). It consists of a HV chamber (1) with front entry (2); a top viewport for optical monitoring (3) of the inside through a video camera (4); feedthroughs for gases (controlled by leak valves) and the electrical connections. Air and liquid measurements were performed in an open-air probe station equipped with four manipulators (Swiss Microtech). Current-voltage measurements were performed using a dual channel SMU Keithley 2612 that is remotely controlled by dedicated software (Fig.2.6 (right)).

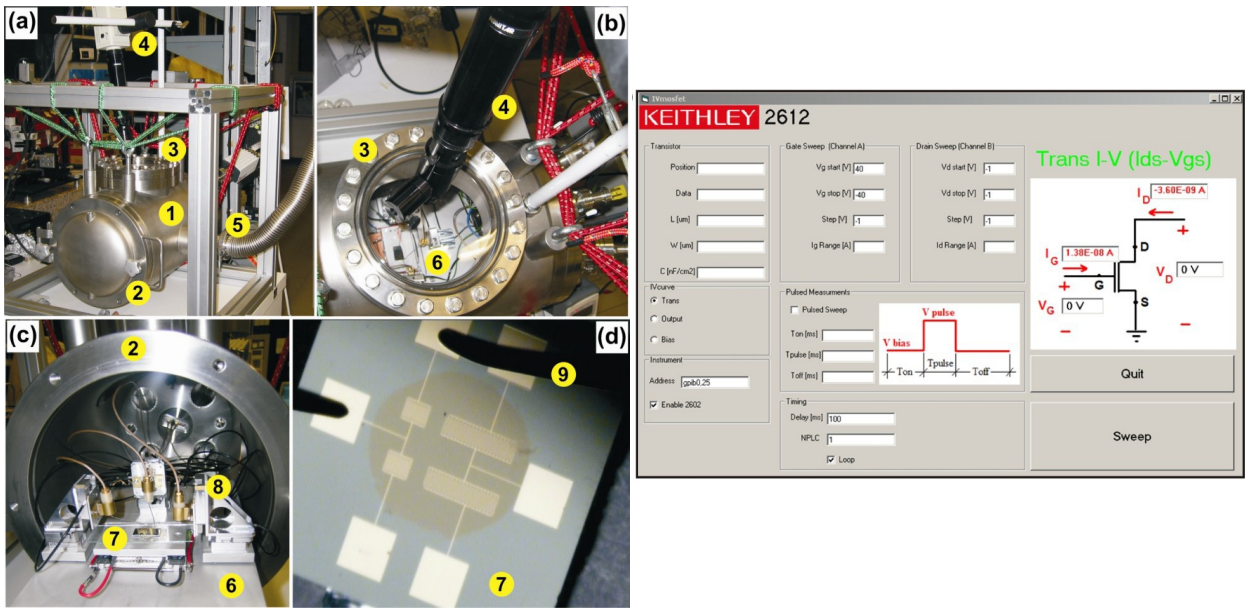

Fig. 2.6 (left) System for electrical measurements under controlled atmosphere. (a) Main view: (1) UHV chamber; (2) front entry; (3) viewport; (4) video camera; (5) pumping connection. (b) Top view. The sliding tray (6) is visible inside the HV chamber. (c) Interior view of the HV chamber showing the test pattern (7) and the piezoelectric motors (8). (d) View of a test pattern; the probes (9) which are connected to the piezoelectric motors are approached on the source and drain contacts by means of a videocamera-assisted joystick which moves the piezoelectric motors. (right) Visual interface of our personalized software.

2.2.2 Analysis of electrical response

The measured field-effect characteristics of these devices can be classified as transfer characteristics (Fig.2.7 (b)) and output characteristics (Fig.2.7 (a)).
The output characteristic graph is an overlay of I_{DS} versus V_{DS} (from 0 to 40 V) at different V_{GS} (from +10 V to -40 V with step of -5 V in our case). The transfer characteristics graph plots the I_{DS} versus V_{GS} for a fixed V_{DS}.
Output curve show the coexistence of two regimes operation of a field-effect transistor: the linear and saturation regimes (Fig3.7 (a)). Transfer curves are recorded separately for both regimes and modelled by the following equations:

$$I_{DS} = \frac{W}{L} C_i \mu \left(V_{GS} - V_{th} - \frac{V_{DS}}{2}\right) V_{DS} \qquad for\ V_{DS} < V_{GS} - V_{th} \qquad \text{Eq. 2.1}$$

$$I_{DS} = \frac{W}{2L} C_i \mu ((V_{GS} - V_{th})^2) \qquad for\ V_{DS} \geq V_{GS} - V_{th} \qquad \text{Eq. 2.2}$$

where W is the channel width, L the channel length, C_i (in units of F/m²) the capacitance per unit area of the insulating layer, V_{th} is the threshold voltage and μ is the field-effect mobility.
The analysis of the characteristics allows extracting the classical device parameters: mobility μ, threshold voltage V_{th}, sub-threshold slope (SS), on/off ratio and pinch-ON voltage (V_{ON}). The charge carrier mobility is referred to the majority carriers (holes in our case) in the semiconductor material and is expressed in units of cm^2/V·s. [14] Mobility is usually extracted

from the slope of the transfer curve in linear regime and from the slope of the linear trend of $\sqrt{I_{DS}}$ *vs* V_{GS} in saturation regime (Fig.2.7 (b) and (c)). [15][16]

The threshold voltage is defined as the gate voltage at which the field-effect takes place and the conductive channel within the OS is created. V_{th} is extracted as the intersection of the extrapolated linear part of the transfer characteristics and the V_{GS} axis. [17]

The semi-logarithmic plot (right axis of Fig.2.7 (b) and (c)) is useful for extracting V_{ON}, SS and the on/off ratio. V_{ON} is the voltage at which I_{DS} increases above the noise level of the off-current. The sub- threshold swing SS (expressed in mV/decade) is a measure of how rapidly the device switches from the off state to the on-state and is extracted from the steep region of the I_{DS} trend. [18] On/off ratio between the maximum and minimum value of the current I_{DS} is an estimate of the amplification. Both SS and on/off ratio are limited by the density of dopants and shallow traps.

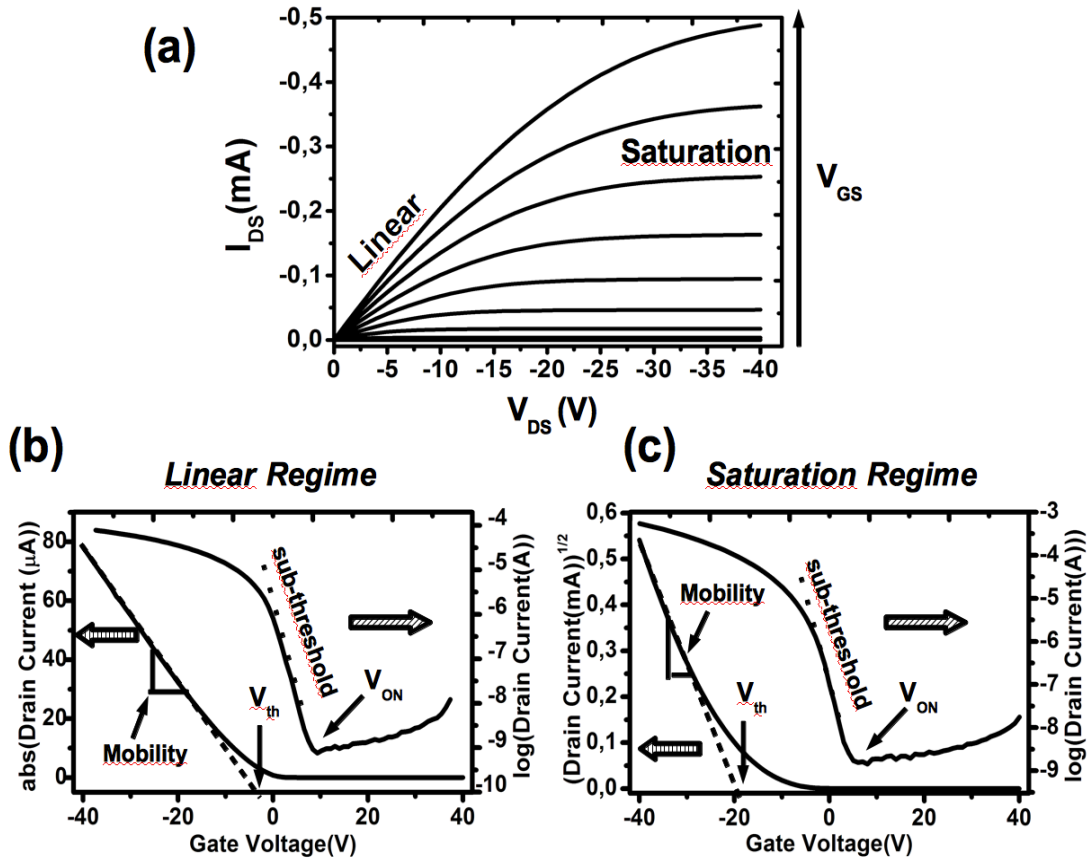

Fig. 2.7 Current-voltage characteristics of pentacene organic field-effect transistor: (a) Output characteristic indicating the linear and saturation regimes; (b), (c) transfer characteristic in the linear regime and saturation regime respectively; the linear graph indicates mobility (μ) and V_{th}, the log-lin curves the SS and V_{ON}

2.2.3 Atomic Force Microscopy (AFM) [19]

Atomic Force Microscopy is a high-resolution scanning probe microscopy developed in 1986 by Binnig, Quate and Gerber [20] when they tried to extend STM technique to non-conductive

samples. The first commercially available AFM was introduced in 1989 and today AFM is one of the foremost tools for imaging, measuring, and manipulating matter at the nanoscale.

AFMs operate by measuring force between a probe and the sample; the probe consists in a sharp tip at the end of a cantilever. The information is gathered by 'feeling' the surface with such kind of mechanical probes guided by piezoelectric elements that facilitate precise and accurate surface rastering. The piezoelectric scanner is constructed by combining independently biased electrodes for X, Y, and Z motion into an empty cylinder tube. Displacements as accurate as fraction of Å in x, y, and z can be controlled with voltages of a few mV.

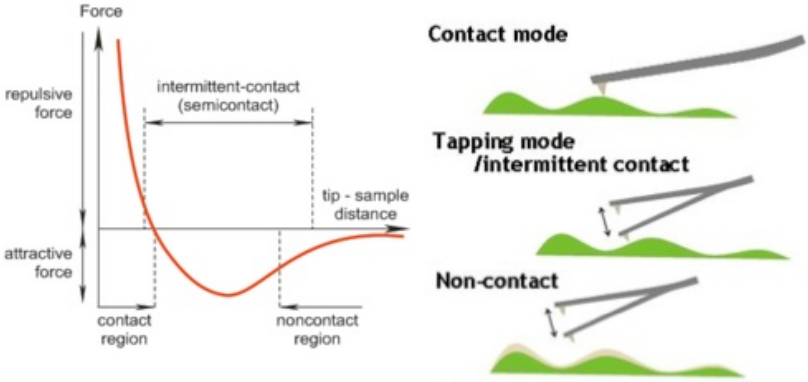

Fig. 2.8 Variation of interatomic force vs. tip-sample distance. In the contact regime the probe is held less than 1nm from the sample surface and the force is repulsive whereas in the non-contact regime the distance is 1-10nm and the forces are attractive.

The deflection of the probe is typically measured by the optical lever method. A semiconductor diode laser is bounced off the back of the cantilever onto a position-sensitive photodiode detector. This detector measures the bending of cantilever during the scan over the sample. The cantilever deflections are measured to generate a map of the surface topography.

There are several modes of operation with AFM depending on tip-sample separation during scanning: contact, non-contact and semi-contact (Fig. 2.8). In the contact mode, the probe tip directly touches the sample surface during scanning. In the non-contact mode, the probe is far enough and does not touch the surface. In the semi-contact mode, the tip is tapping onto the sample surface. The choice of the operation mode depends on experimental requirements and state of the sample.

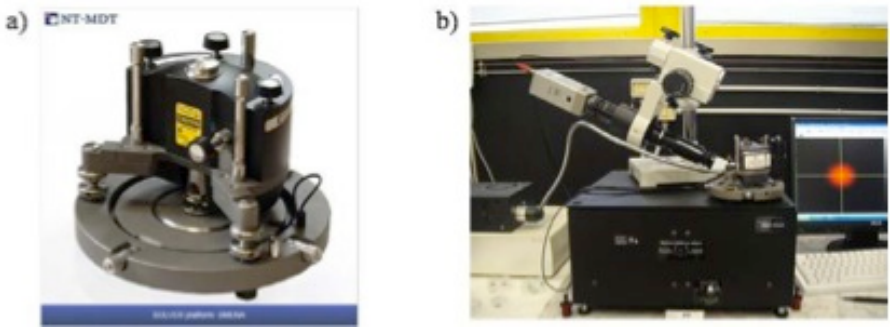

Fig. 2.9 NT-MDT ™ Standalone Smena, b) AFM setup used at ISMN-CNR Bologna-Italy.

Throughout this thesis, the morphological investigations are based on AFM operating in semi-contact mode. We used a Smena (NT-MDT, Zelenograd, Russia) [21] AFM consisting of standalone head with the piezo scanner positioned inside the head. The sample is fixed on a special sample holder, and the head is the only moving part. The microscope is equipped with a camera and placed on an anti-vibration stage (Fig. 2.9).

The tips are distributed by Molecular Devices and Tools for Nanotechnology (NT-MDT) and their specifications are: chip size 3.6x1.6x0.4 mm; tip height: 10-15 μm; tip angle: ≤ 22°; tip curvature radius: 10 nm; and resonant frequency: 190-325 kHz and 115-190 kHz. Fig. 2.10 shows typical AFM topography images of S/D electrodes and channel of our standard TP.

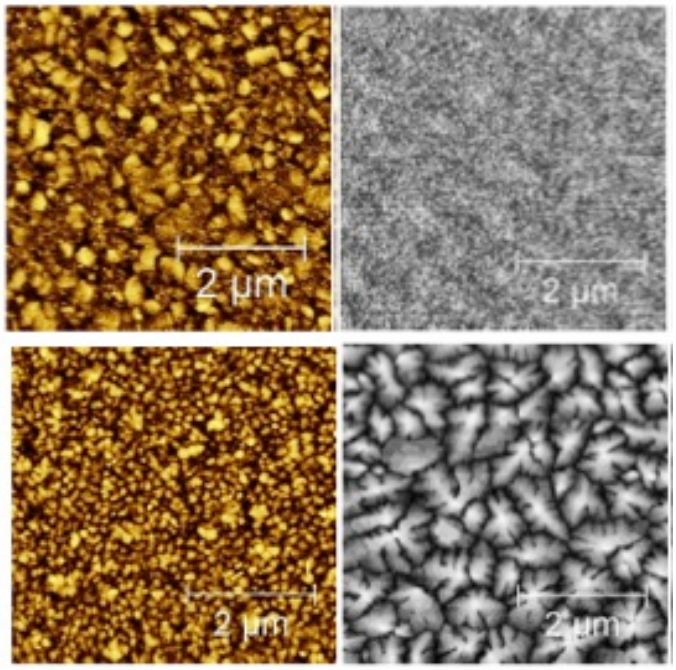

Fig. 2.10 Topographic AFM images (5x5 μm) of our standard test pattern; (a) bare S/D gold electrodes and SiO_x channel, (b) pentacene coated S/D electrode and channel.

AFM data is particularly suitable for further processing and analysis, and has some particular requirements, due to the three- dimensional nature of the date obtained. Proper use of image processing techniques is important in order to enable further analysis while accurately reflecting the real nature of the sample, and avoiding the introduction of errors. There are many powerful analysis routines for AFM data, which could be essential to extract the largest number of information from image data. In nanotechnology, the morphological study on the organic thin-film have an important role in understanding the properties of the film itself and its growth mechanism; the latter in fact, has a profound effect on all physical characteristic (electrical, mechanical, optical, etc...) of the film. [22][23]

As example surface roughness, σ_{rms}, is a measure of the texture of a surface. It is quantified by the vertical deviations of a real surface from its ideal form. If these deviations are large, the surface is rough; if they are small the surface is smooth.

Mathematically surface roughness is defined as the root mean square (σ_{rms}) of the roughness profile. [24]

$$\sigma_{rms}(L,t) = \sqrt{\frac{1}{L}\sum_{i=1}^{L}\left[h(1,t) - \bar{h}(t)\right]^2} \qquad \text{Eq. 2.3}$$

where *h(i,t)* is the height of point *i* at time *t* and *L* the number of points.

In case of thin-film morphology also correlation length, ξ, could provide important details by discriminating physical properties associated with a characteristic distance or purely random points. Among the large number of analysis tools, correlation functions evidence the presence of spatial correlations between two random variables as a function of distance in time or space. Concerning topographical studies of organic semiconductors, such statistical analysis can quantitatively inspect the characteristics of the surface morphology and the kinetic growth

process. In this thesis I have been using Gwyddion image analysis software [25] to extract the height-height correlation function from AFM images.
The height–height correlation function $H(\tau_x)$ is calculated along the fast scan direction (x direction) through the Eq. 2.4:

$$\mathrm{H}_x(\tau_x) = \frac{1}{N(M-m)} \sum_{l=1}^{N} \sum_{n=1}^{M-m} \left(z_{n+m,l} - z_{n,l}\right)^2 \qquad \text{Eq. 2.4}$$

where $z(n, l)$ denotes the topographical height of the surface measured by AFM at the point (n, l), N x M the total number of points at which the surface heights have been measured and m is defined as $\tau_x/\Delta x$ thus the function can be evaluated in a discrete set of values of τ_x separated by the sampling interval Δx. Fig. 2.11 depicts HHCF in log-log form extracted from AFM images:

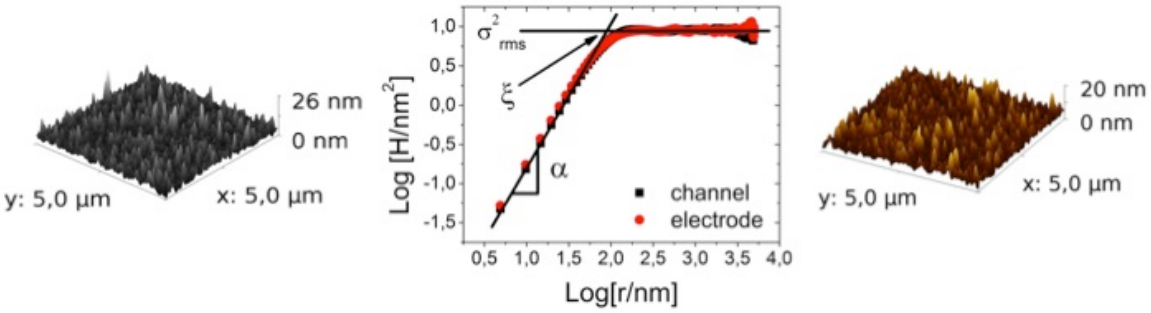

Fig. 2.11 AFM images and their height-height correlation function; on the left P3HT morphology on channel surface (black squares) and on the right P3HT morphology on electrode surface (red dots). Surprisingly the sample shows the same P3HT morphology in both channel and electrode. [26]

As highlighted in the graph, we have extracted three parameters from $H(\tau_x)$: (i) the saturated roughness, σ_{rms}, is the square root of the plateau of $H(\tau_x)$ [27], (ii) the roughness coefficient α, which is the slope of the τ-scaling branch [28] and (iii) the correlation length (ξ) that is the intersection between the plateau and τ-scaling branch projections.
σ_{rms}, as already described above, is a measure of the mean square fluctuations of the surface topography at large length scales; roughness exponent and correlation length could be correlated to grains features, in particular α is sensitive to grains shape [29] instead ξ to their lateral dimensions.

2.2.4 Electrochemical techniques [30]

Electrochemistry studies chemical reactions in solution at the interface between an electrode and an ionic conductor (i.e. the electrolyte). Electrochemical processes usually involve an electron transfer reaction between the electrode and an electrochemical-active molecule in solution.
Cyclic voltammetry is the most widely used technique for acquiring qualitative and quantitative information about electrochemical reactions. In presence of an electro-active probe in solution, cyclic voltammetry offers a rapid extraction of their redox potentials by sweeping a voltage and monitoring the flowing current (namely I-V graph). In case of a reversible electrochemical reaction, the CV recorded shows well-defined characteristics:
1.The voltage separation between the current peaks is 59 mV for a mono-electronic redox reaction.
2. The positions of peak voltage do not shift as a function of voltage scan rate.
3.The ratio of the peak currents is equal to one.

4. The peak currents are proportional to the square root of the scan rate as described by the Randles-Sevcik equation.

Fig. 2.12 illustrates the typical cyclovoltammogram of a reversible electrochemical process.

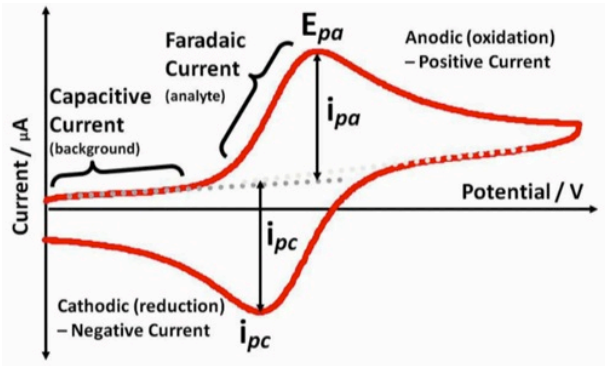

Fig. 2.12 Cyclic voltammetry of a completely reversible process.

Electrochemical techniques, like CV described above, are based on the application of a step-wise potential or current driving the system to non-equilibrium conditions.

An alternative approach is electrochemical impedance spectroscopy (EIS) that monitors the response of a system to a small AC signal thus avoiding strong perturbation to its stationary state. EIS has two main advantages:

1. The absence of a significant perturbation on the system allows longer experimental timescale and the collection of larger amount of data.
2. The I-V plot could be considered linear for low intensity perturbations.

EIS can be applied to a variety of electrochemical systems but sometimes its use is still limited by the complexity of systems itself and the complex interpretation of data that relies on models.

In the EIS we are interested in the response to the application of a sinusoidal signal, which for a linear system, will be a sinusoid at the same frequency but shifted in phase.

Let us consider an excitation potential in the form of Eq. 2.5:

$$E = E_0 \sin(\omega t) \qquad \text{Eq. 2.5}$$

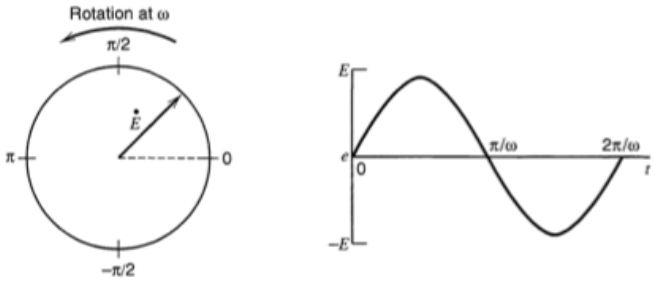

Fig. 2.13 Phasor diagram for an alternating voltage, $E = E_0 \sin(\omega t)$

where E_0 is the amplitude of the signal, and ω is the radial frequency (Fig. 2.13). The relationship between radial frequency ω (expressed in radians/second) and frequency f (expressed in hertz) is: $\omega = 2\pi f$.

The AC measurements imply sinusoidal signal of both current and voltage. They can be described as rotating phasors as a function of frequency.

As shown in Fig. 2.14, current will have a phase difference Φ with respect to voltage (Eq. 2.6):

$$I = I_0 \sin(\omega t + \phi) \qquad \text{Eq. 2.6}$$

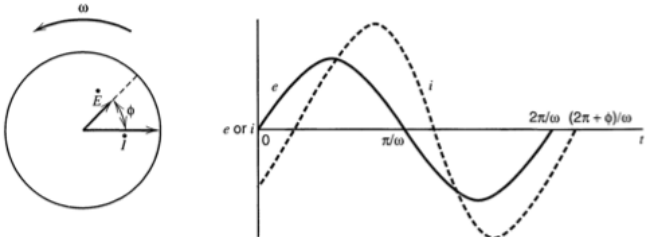

Fig. 2.14 Phasor diagram showing the relationship between alternating current and voltage signals at frequency ω.

Applying these concepts to the analysis of some simple circuits, we consider the AC response of a simple resistance:

$$I = E/R \sin(\omega t) \qquad \text{Eq. 2.7}$$

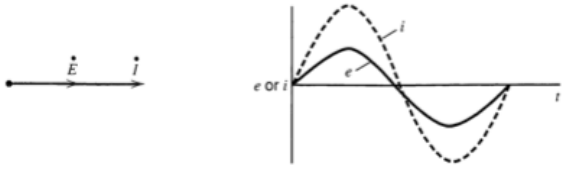

Fig. 2.15 Relationship between the voltage across a resistor and current through the resistor.

In this case the phase angle is 0 (Eq. 6) and the phasor diagram is represented in Fig. 2.15. Conversely, the AC response of a capacitor is governed by the following equations (Eq. 2.8 and Eq. 2.9):

$$q = CE \qquad \text{Eq. 2.8} \qquad\qquad I = C\,dE/dt \qquad \text{Eq. 2.9}$$

We can express the relationship between *I* and *E* as:

$$I = E/X_C \sin(\omega t + \pi/2) \qquad \text{Eq. 2.10}$$

Where *Xc* in Eq. 2.10 represent the capacitive reactance or $1/\omega C$.

Now the I-V phase shift is $\pi/2$ and this is useful to represent the phasors as complex notation by multiplying the ordinate component by $j=(-1)^{1/2}$ as depicted in Fig. 2.16. This representation is described by Eq. 2.11:

$$E = -jX_C I \qquad \text{Eq. 2.11}$$

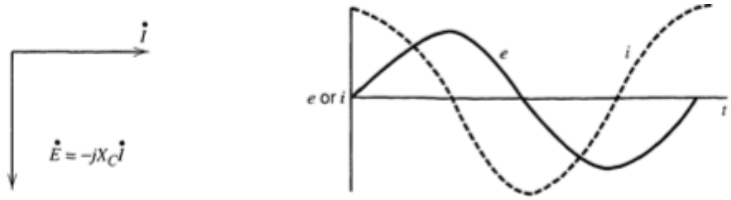

Fig. 2.16 Relationship between an alternating voltage across a capacitor and the alternating current through the capacitor.

In a more complex system, in which a capacitor and a resistance are in series, the final potential is given by the sum of each component (Eq. 2.12):

$$E = E_R + E_C = I(R + jX_C) = IZ \qquad \text{Eq. 2.12}$$

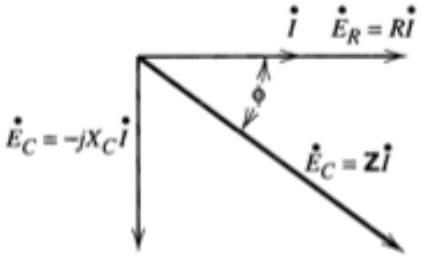

Fig. 2.17 Phasor diagram showing the relationship between the current and the voltages in a series *RC* network. The voltage across the whole network is *E,* and E_R and E_C are its components across the resistance and the capacitance,

where Z is the impedance of the circuit, whose module is equal to $(R^2+X_c^2)^{1/2}$ and phase angle: $tan\phi = X_C/R = 1/\omega RC$ (Fig. 2.17); thus Ohm equation can be re-written as: $E=ZI$.

The concept of impedance can be also applied to more complex circuits but a right combination of the circuit elements is required in order to obtain the correct interpretation of the output data.

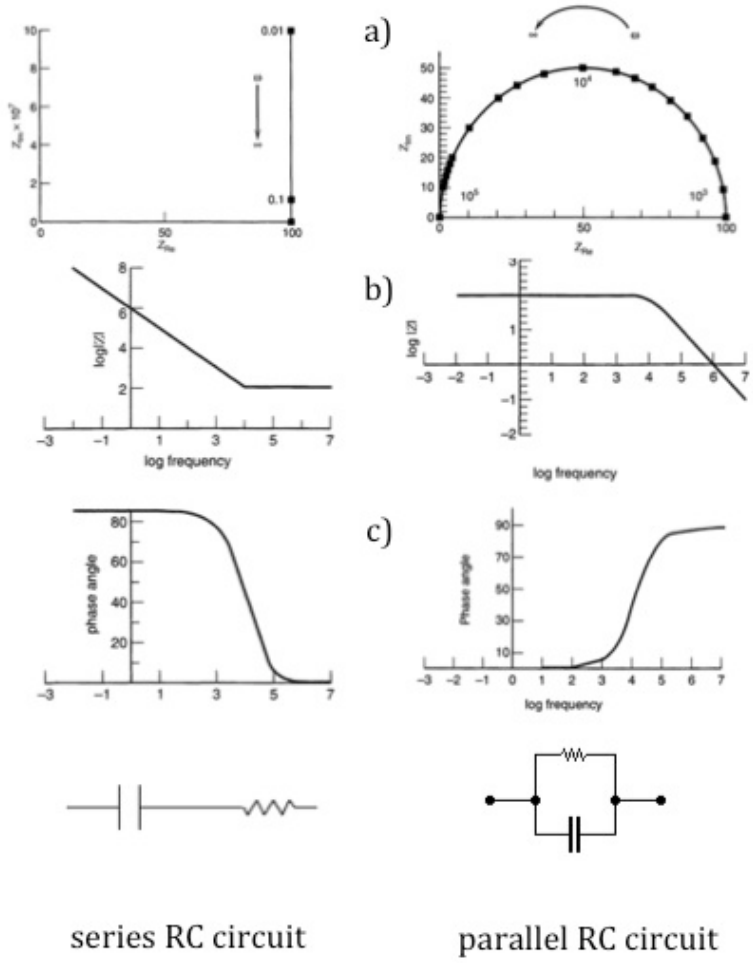

Fig. 2.18 Nyquist a) and Bode plots b) c) for a series RC circuit with R = 100Ω and C= 1μF; Nyquist a) and Bode plots b) c) for a parallel RC circuit with R = 100Ω and C= 1μF.

As a result, the experimental information must be carefully interpreted and manipulated with a correct equivalent circuit; this has to be a proper combination of different circuit elements, such as resistor, capacitance etc.

Output data (Fig. 2.18) can be visualized in a 3D plot composed by the real part (Re), the imaginary part (Im) and frequency (ω).

The most common representation for impedance data is the Nyquist Plot (Fig. 2.18 a)) that describes the imaginary part of impedance (product of capacitance and frequency) *vs* the real part (resistance). An alternative graph is the Bode diagram (Fig. 2.18 b) and c)) where ϕ or $log\ Z$ are displayed as a function of frequency ($log\ \omega_i$).

The electrochemical data presented in this thesis were obtained with a potentiostat/ galvanostat μ-Autolab III (Metrohm, Milan, Italy). This is able to perform DC and AC measurements with sensitivity up to nA. A 1 mm diameter polycrystalline gold wire was used as a working electrode (WE), whereas a Pt sheet and Ag/AgCl electrodes were chosen as counter electrodes (CE) and reference electrodes (RE) respectively. Other experimental specifications are given in each chapter.

2.2.5 Contact Angle Measurements

The sessile drop technique is a method used for the determination of solid surface energy. The main assumption of the method is that by placing a droplet of liquid on a solid surface, its shape (i.e. the contact angle) and its surface tension can be used to calculate the surface energy of the solid sample.

The contact angle is defined as the angle arising from the intersection of the liquid/solid interface and the liquid/air interface. The measurement of this angle is performed with a goniometer, which allows the user to define the contact angle by means of the optical visualization (Digidrop GBX Model DS) (Fig. 2.19). [31]

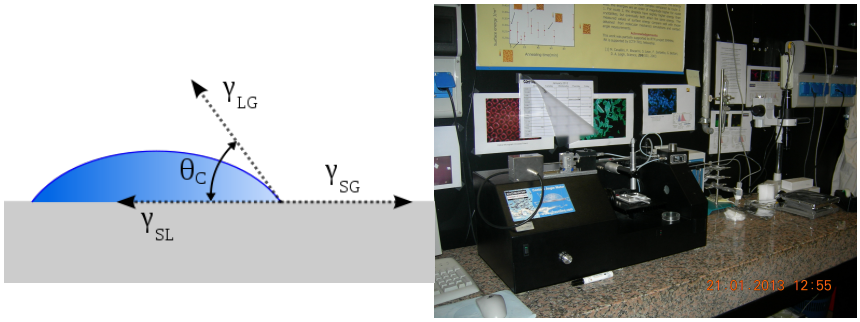

Fig. 2.19 (left) Schematic of a liquid drop showing the quantities in Young's equation; (right) contact angle setup used at ISMN-CNR Bologna-Italy.

One of the most common procedures to calculate the surface energy of a solid surface is the Zisman's method that defines the surface energy as being equal to the surface energy of the highest surface energy liquid that wets the solid completely.

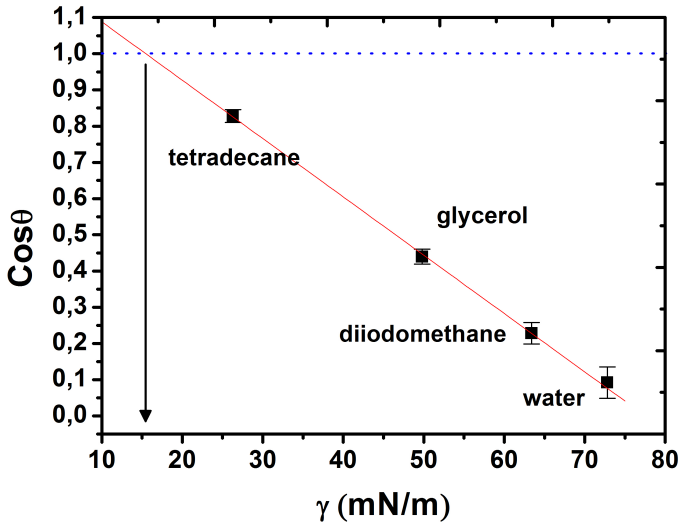

Fig. 2.20 Zisman's plot .

The method can be applied to sample with high surface energy. The method relies on the acquisition of the contact angle of different liquids (at least three) on the solid surface. The cosine of the contact angles are plotted against the known surface energy to yield the surface tension value as the extrapolated intercept of the straight line with $cos\theta$=1. This is the highest liquid surface energy, real or hypothetical, that would result in complete wetting of the sample with a contact angle of zero degrees. This value is considered an estimation of the solid surface energy. A typical Zisman's plot is shown in Fig. 2.20.

A more robust interpretation of contact angle data could be obtained by considering the work of adhesion of a solid surface. The work of adhesion [32] is defined as the work per unit area required to separate two substances in contact. Let's now consider a liquid in contact with a solid surface; the equilibrium free energy between them is well described by Duprè equation:

$$W_A = \gamma_{S^\circ} + \gamma_{LV^\circ} + \gamma_{SL} \qquad \text{Eq. 2.13}$$

where W_A is the work required to form a unit area of pure solid and pure liquid surface, γ_{S° is the specific surface energy of the pure solid measured in absolute vacuum, γ_{LV° is the specific surface energy of the pure liquid measured in its saturated vapour and γ_{SL} is the specific solid-liquid interfacial free energy.

The difficulties in measuring γ_{S° and γ_{SL} can be overcome by assuming Young equation (Eq. 2.14):

$$\gamma_{SA} = \gamma_{SL} + \gamma_{LA}\, cos\Theta \qquad \text{Eq. 2.14}$$

if the experiment is performed in vapour saturated atmosphere, Eq. 2.14 can be transformed as follows:

$$\gamma_{SV^\circ} = + \gamma_{SL} + \gamma_{LV^\circ} cos\Theta_E \qquad \text{Eq. 2.15}$$

where γ_{SA} is the surface energy at solid-air interface, γ_{SL} is the surface energy at solid-liquid interface, γ_{SV° is the surface energy at solid-liquid interface (at saturated pressure) and Θ_E is the equilibrium contact angle in saturated vapour.

When the vapour pressure of the liquid is less than the saturated pressure and the contact angle does not change with time, the '°' can be dropped, hence:

$$\gamma_{SV} = + \gamma_{SL} + \gamma_{LV} cos\Theta_E \qquad \text{Eq. 2.16}$$

By combining Eq. 2.16 with Duprè's equation (Eq. 2.13) we obtain:

$$W_A = \gamma_{S^\circ} - \gamma_{SV} + \gamma_{LV^\circ} (1+ \gamma_{LV}/\gamma_{LV^\circ} cos\Theta_E)$$

or

$$W_A = \pi + \gamma_{LV} (1+cos\Theta_E) \qquad \text{Eq. 2.17}$$

where $\pi = \gamma_{S^\circ} - \gamma_{SV}$ represent the surface spreading pressure and $\gamma_{LV} \cong \gamma_{LV^\circ}$ that is valid for low vapour pressure liquids.

For water and non-volatile liquids, the saturated pressure is so low that π become negligible, unless the adsorbents are hygroscopic, and last equation reduces to:

$$W_A = \gamma_{LV} (1+cos\Theta_E) \qquad \text{Eq. 2.18}$$

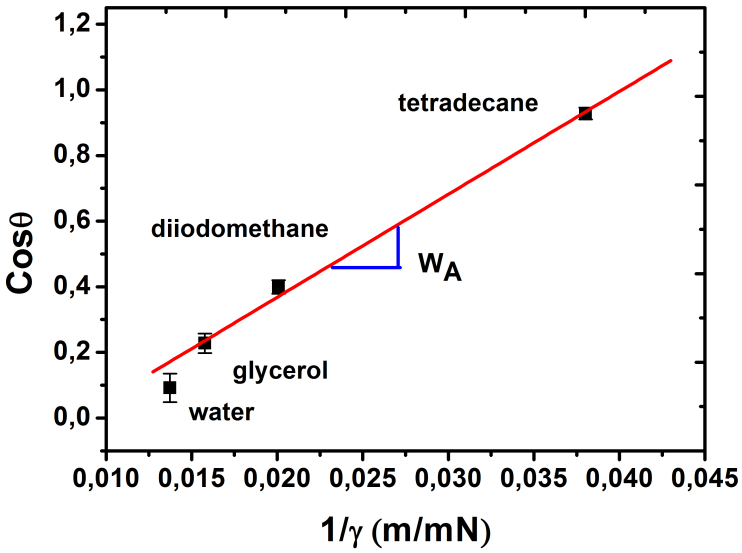

Fig. 2.21 Extraction of W_A.

The validity of the above relations depends on the validity of the assumptions made. The first assumption considers a system where the surface energy of the solid is comparable with the surface tension of the liquid. The second assumption takes into account the surface tension of the liquid in air, which has to be equal to the surface tension of the liquid in its saturated vapour.

Practical aspects of this theory are reflected in Fig. 2.21, where $1/\gamma_{LV}$ for at least three liquids are plotted against their $cos\Theta$, the slope of the linear fit represent W_A of the surface.

References:

[1] www.fbk.eu

[2] index @ www.phasis.ch

[3] www.scriba-nanotec.com

[4] www.arrandee.com,

[5] R. Michalitsch, A. Elkassmi, A. Yassar, F. Gamier, A practical synthesis of functionalized alkyl-oligothiophenes for molecular self-assembly, J. Heterocycl. Chem. 38 (2001) 649–653.

[6] S. Casalini, A. Shehu, S. Destri, W. Porzio, M.C. Pasini, F. Vignali, et al., Organic field-effect transistors as new paradigm for large-area molecular junctions, Org. Electron. 13 (2012) 789–795.

[7] A. Operamolla, O. Hassan Omar, F. Babudri, G.M. Farinola, F. Naso, Synthesis of S-Acetyl Oligoarylenedithiols via Suzuki−Miyaura Cross-Coupling, J. Org. Chem. 72 (2007) 10272–10275.

[8] O. Hassan Omar, F. Babudri, G.M. Farinola, F. Naso, A. Operamolla, Synthesis of S-Acetyl Oligo-p-aryleneethynylene Tetrathiols, European J. Org. Chem. 2011 (2011) 529–537.

[9] G. Bruno, F. Babudri, A. Operamolla, G. V Bianco, M. Losurdo, M.M. Giangregorio, et al., Tailoring Density and Optical and Thermal Behavior of Gold Surfaces and Nanoparticles Exploiting Aromatic Dithiols, Langmuir. 26 (2010) 8430–8440.

[10] S. Casalini, F. Leonardi, C.A. Bortolotti, A. Operamolla, O.H. Omar, L. Paltrinieri, et al., Mono/bidentate thiol oligoarylene-based self-assembled monolayers (SAMs) for interface engineering, J. Mater. Chem. 22 (2012) 12155–12163.

[11] S. Casalini, M. Berto, F. Leonardi, A. Operamolla, C.A. Bortolotti, M. Borsari, et al., Self-Assembly of Mono- And Bidentate Oligoarylene Thiols onto Polycrystalline Au, Langmuir. 29 (2013) 13198–13208.

[12] R.K. Shervedani, M. Bagherzadeh, Electrochemical Characterization of In Situ Functionalized Gold Cysteamine Self-Assembled Monolayer with 4-Formylphenylboronic Acid for Detection of Dopamine, Electroanalysis. 20 (2008) 550–557.

[13] R.K. Shervedani, S.A. Mozaffari, Copper(II) Nanosensor Based on a Gold Cysteamine Self-Assembled Monolayer Functionalized with Salicylaldehyde, Anal. Chem. 78 (2006) 4957–4963.

[14] M.J. Małachowski, J. Żmija, Organic field-effect transistors, Opto-Electronics Rev. 18 (2010) 121–136.

[15] C.D. Dimitrakopoulos, P.R.L. Malenfant, Organic Thin Film Transistors for Large Area Electronics, Adv. Mater. 14 (2002) 99–117.

[16] D. Braga, G. Horowitz, High-Performance Organic Field-Effect Transistors, Adv. Mater. 21 (2009) 1473–1486.

[17] G. Horowitz, R. Hajlaoui, H. Bouchriha, R. Bourguiga, M. Hajlaoui, The Concept of "Threshold Voltage" in Organic Field-Effect Transistors, Adv. Mater. 10 (1998) 923–927.

[18] J.P. Colinge, D. Flandre, F. Van de Wiele, Subthreshold slope of long-channel, accumulation-mode p-channel {SOI} {MOSFETs}, Solid. State. Electron. 37 (1994) 289–294.

[19] M. V. L., Foundamentals of Scanning Probe Microscopy, Moscow: Te, 2004.

[20] G. Binnig, C.F. Quate, C. Gerber, Atomic Force Microscope, Phys. Rev. Lett. 56 (1986) 930–933.

[21] 71b9fc8c3d6e4b57f6247c816188138c0be49246 @ www.ntmdt.com, (n.d.).

[22] J. KRIM, G. PALASANTZAS, EXPERIMENTAL OBSERVATIONS OF SELF-AFFINE SCALING AND KINETIC ROUGHENING AT SUB-MICRON LENGTHSCALES, Int. J. Mod. Phys. B. 09 (1995) 599–632.

[23] P. Viville, R. Lazzaroni, J.L. Brédas, P. Moretti, P. Samorí, F. Biscarini, The Influence of Thermal Annealing on the Morphology of Sexithienyl Thin Films, Adv. Mater. 10 (1998) 57–60.

[24] A.L. Barabasi, Fractal Concepts in Surface Growth, Cambridge University Press, 1995.

[25] www.gwyddion.net

[26] S. Casalini, F. Leonardi, T. Cramer, F. Biscarini, Organic field-effect transistor for label-free dopamine sensing, Org. Electron. 14 (2013) 156–163.

[27] F. Biscarini, P. Samorí, O. Greco, R. Zamboni, Scaling Behavior of Anisotropic Organic Thin Films Grown in High Vacuum, Phys. Rev. Lett. 78 (1997) 2389–2392.

[28] J. Krim, J.O. Indekeu, Roughness exponent: A paradox resolved, Phys. Rev. E. 48 (1993) 1576–1578.

[29] T.J. Oliveira, F.D.A. Aarão Reis, Roughness exponents and grain shapes, Phys. Rev. E. 83 (2011) 41608.

[30] A.J. Bard, L.R. Faulkner, Electrochemical Methods: Fundamentals and Applications, 2001.

[31] www.gbxonline.com

[32] W.A. Zisman, Advances in Chemistry Series 43, Washington, Am. Chem. Soc. (1964) 1.

OFET as charge injection organic gauge (CIOG)

3

This chapter briefly introduces Self-Assembled Monolayers (SAMs) and their applications in organic electronics. The control of charge injection across SAM is the main topic due to the surface engineering of S/D electrodes. As a result, a series of works are presented, in which OFETs respond as charge injection organic gauge by varying both tail/head groups and the chain length SAMs placed between S/D electrodes and the organic semiconductor.

3.1 Self-Assembled Monolayers (SAMs) in organic electronics

Self-assembled monolayers are molecular building blocks that are able to auto-organize into ordered 2D functional structure (Fig.3.1). SAMs are an excellent surface modification, and their rigidity, length, and terminal functional groups allow one to tune the interfacial features of the surface of interest. [1]

OFET architecture is a complex structure, which can hinders the ideal growth of the semiconductor. As a consequence, it is commonly observed the differential growth of the organic semiconductor at the charge-injection interface. SAMs could be an elegant strategy to overcome these technological drawbacks.

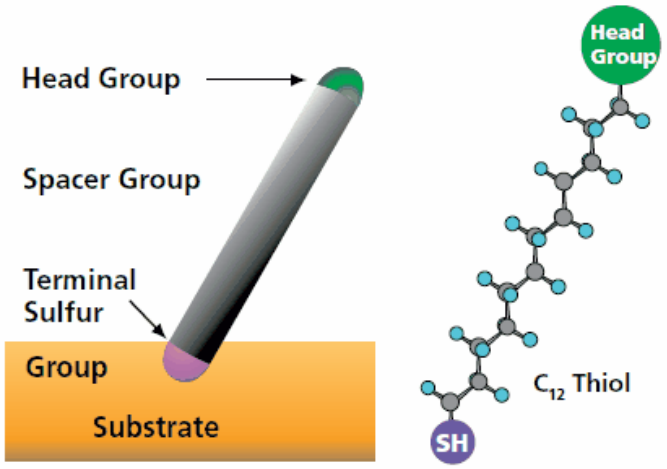

Fig.3. 1 Schematic view of SAM structure

The use of SAMs within OFET layout can affect the semiconductor orientation, its grain size as well as its crystallinity. Silanes are one of the most known classes of self-assembling molecules, such as n-octadecyltrichlorosilane (OTS) or hexamethyldisilazane (HMDS). They are able to functionalize the SiO_2 surface, a common dielectric material. Both silanes are covalently bonded onto SiO2 yielding a lower surface energy and consequently improving the crystallinity of various organic semiconductors (e.g., pentacene, C60, oligothiophenes). For example Kim and co-workers [2,3] have demonstrated two different orientations of P3HT (i.e. parallel and perpendicular to the insulator

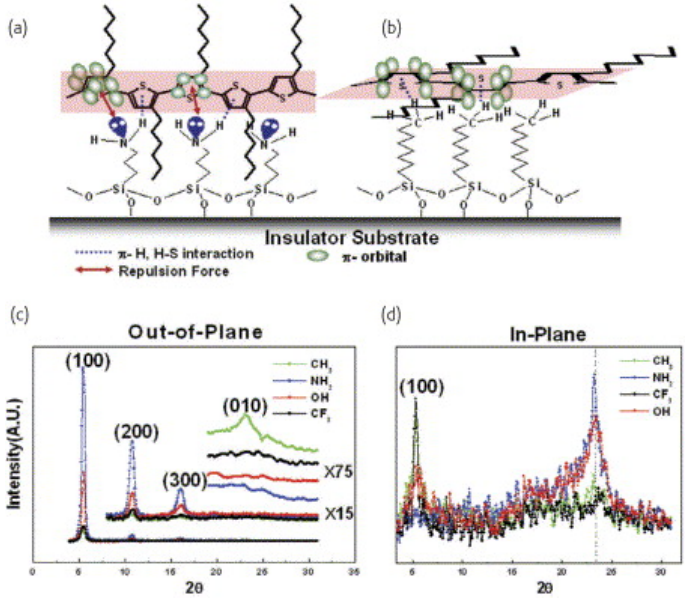

Fig.3. 2 Schematic of P3HT conformations, (a) edge-on and (b) face-on, according to interfacial characteristic. (c) Out-of-plane and (d) in-plane grazing incidence angle X-ray diffraction intensities as a function of the scattering angle 2Θ for regioregular P3HT thin film crystallized on insulator substrates modified with different SAMs. [2]

substrate),by using alkylsilane SAM on the channel. (Fig.3.2). Thus, they observe an increase of the field-effect mobilitiy by a factor of four, when the perpendicular orientation takes place on the dielectric.

The same considerations have to be taken into account once small molecules and oligomers, such as pentacene, are deposited by ultra high-vacuum deposition. [4–8]

Looking at the metallic contacts, others phenomena arise: the organic semiconducting molecules usually have different growth modes with respect to channel oxides. This leads to an intrinsic morphological disorder at this interface;, secondly the use of SAM can affect the metal work-function. De Boer and co-workers in 2005 used alkanethiols and perfluorinated ones to, respectively, decrease [9–12] and increase [9,13] the work-function- of metal contacts. This means that the metal work-function can be finely tuned by using SAMs which bears dipoles with different orientations and strength. An efficient charge injection occurs only when the metal work function matches the HOMO/LUMO level of the organic semiconductor.

For instance, the preferred orientation of pentacene molecules onto flat, inert substrate, like SiO_x, results almost perpendicular to the substrate, since the (001) plane in pentacene crystals has the lowest surface energy. On contrary, surfaces with high surface tension, like metals or SiOx properly functionalized, induce an opposite orientation. As a consequence, the interactions of pentacene molecules with the substrate become more dominant, and they lie flat on the surface. [14,15]

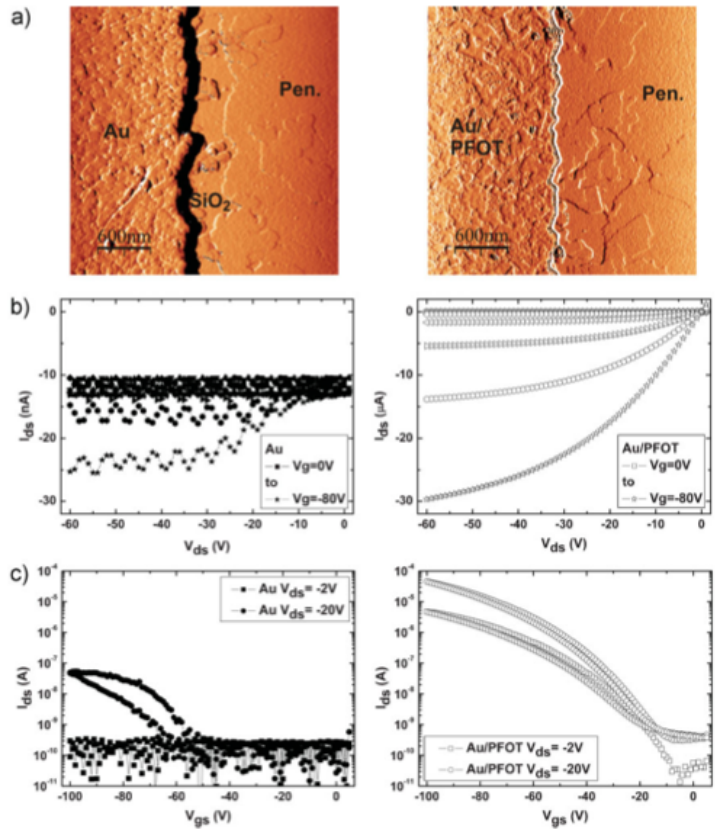

Fig.3. 3 AFM images (3x3µm²) of a monolayer of pentacene at the interface between gold and SiO_x a) bare gold, b) PFOT-modified gold. d) Output characteristics of transistor with Au (left) and Au-PFOT (right) electrodes. c) Transfer characteristics of the same transistor sas in b). [17]

Recent studies on metal/SAM/pentacene systems have shown that SAMs not only tune the metal work-function, but also alter the surface tension yielding a different OS morphology with respect to the bare metal (Fig.3.3). [16,17]

As shown in Fig.3.3, the SAM-modified metal electrodes improve the pentacene morphology at the interface between electrodes and channel leading to a clear improvement of the charge injection.

In organic device SAMs can act not only as a passive components but they can act as nanodielectrics (Self-assembled Nanodielectrics, SANDs). In 2000, Vuillaume's group in Lille, France, demonstrated that a single layer of carboxyl-terminated n-alkylsilanes on natively oxidized silicon could serve as a molecular dielectric layer in TFTs with a thickness of a few nanometers and with low leakage current. [18]

The most beneficial feature of this approach is the low operational voltage due to the larger capacity ($C \approx 0.4–0.7$ F μcm^{-2}) of the nanodielectric layer compared with the usual dielectrics.
A further excellent exploitation of SAMs applied to OFET is the so-called SAMFETs, in which SAMs act directly as semiconducting material due to their high aromaticity.
Three main examples came out: (i) silane-bonded oligothiophenes (4T and 5T) on AlO_x, (ii) hexabenzocoronenes (HBCs) covalently bonded on SiO_x, and (iii) poly- or functional oligothiophenes assembled (*via* the PA anchor group) on ZnO surfaces. [19–24]
In conclusion molecular self-assembly is a powerful tool for creating functional films in organic electronics due to the wide library of self-assembling molecules provided by the organic chemistry. SAMs represent an elegant and straightforward approach to combine complex functionalities in organic devices and they pave the way towards smart applications in molecular electronics.

3.2 Study of tunnelling across self-assembly monolayer

Charge transport across alkanethiol SAMs has been widely investigated in a variety of Au/molecule/metal junctions, where the metal counter-electrode is made with either vacuum-sublimed Au films,[25] conductive scanning probes,[26] mercury droplets,[27][28] or by mechanically controlled break junctions.[29]

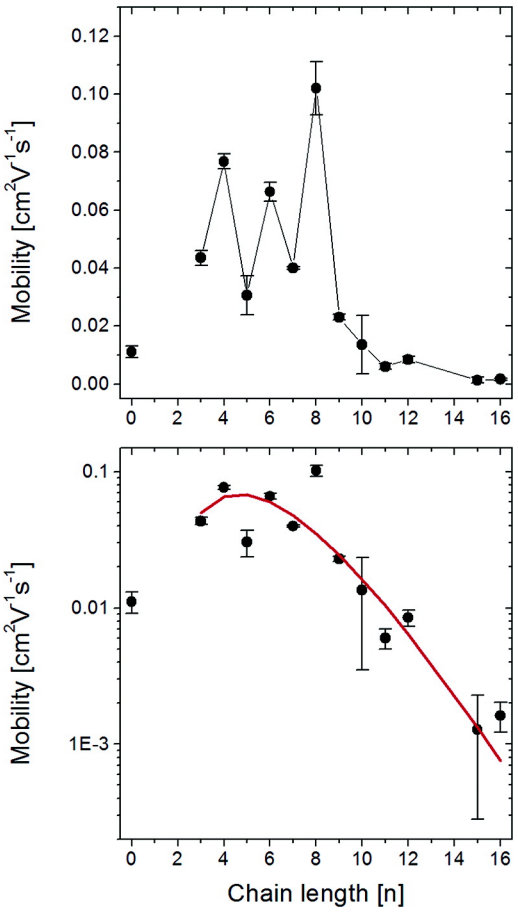

Fig.3. 4 (top) Charge mobility of pentacene FETs vs alkanethiol chain length *n* as obtain in saturation regime. (bottom) The same data in a semilog plot. [30]

In all these experiments, the conductance of the monolayer junction decays exponentially versus the chain length *n* (expressed as the number of C atoms in the alkyl chain, or methylene units) as $exp(-\beta n)$. The measured inverse decay rate lies in the range 0.5-1 $Å^{-1}$ for aliphatic SAM and 0.2-0.5 $Å^{-1}$, suggesting a resonant through-bond tunneling.
In 2007, Stoliar P. et al. [30] systematically investigate the influence of *n*-alkanethiol monolayers, with chain length ranging between 3 and 16 units, on the response of a real organic FET. The insertion of an alkanethiol spacer between pentacene and gold electrode clearly affects the charge carrier mobility.
As shown in Fig.3.4 (top), the field-effect mobility vs. *n* shows the so-called "odd-even effect" for intermediate chain-length (namely up to 9 carbon atoms). The μ behaviour reveals an exponential dependence as a function of the chain length (see Fig.3.4), following this phenomenological fit function:

$$\mu(n) = \mu_l \, n^{\alpha} \, e^{-\beta n} \qquad \text{Eq. 3.1}$$

where *n* is the number of homolog units, α is a scaling factor and β is the decay exponent, representing the inverse decay length of the charge tunnelling. The

global fit of the data exhibits an exponential decay rate β equal to 0.90 ± 0.19 (odd) and 0.72 ± 0.20 (even) inverse methylene units (CH_2^{-1}). The β values were in agreement with the values reported for the current across single alkanethiol molecule junctions (0.5-1 $Å^{-1}$). [31]

Not only the electrical behaviour, but also the pentacene morphology depends on the surface because the use of SAMs alters the surface energy and consequently it changes the pentacene growth mode [17]

The rationale of Stoliar et al introduced the new concept of charge-injection lengthscale, λ, which took into account three competing effects: (i) the thickness of the "geometrical" barrier that was systematically increased from 3 to 16 carbon atoms, [31](ii) the decrease of the hole injection barrier with n; (iii) the decreasing interfacial disorder with *n*. All these effects were merged together in the interfacial length scale λ:

$$\lambda = constant + (n\text{-}1)l + \zeta(n) \qquad \text{Eq. 3.2}$$

where the first two terms on the right side add to the thickness of the alkanethiol, being the constant equal to the sum of the equilibrium distance $r_{Au\text{-}S}$ between Au and S in the thiolate, the S-C bond length $r_{S\text{-}C}$, and the equilibrium distance of pentacene on the alkanethiol layer, r_{Pen}.

Fig.3.5 shows the overall behaviour of λ that displays two regimes of short and long chain lengths ruled by different dominating effects.

The overall perspective coming from these results is that FETs are extremely sensitive to tiny differences at the interface especially to the tilt angle of the last σ bond.

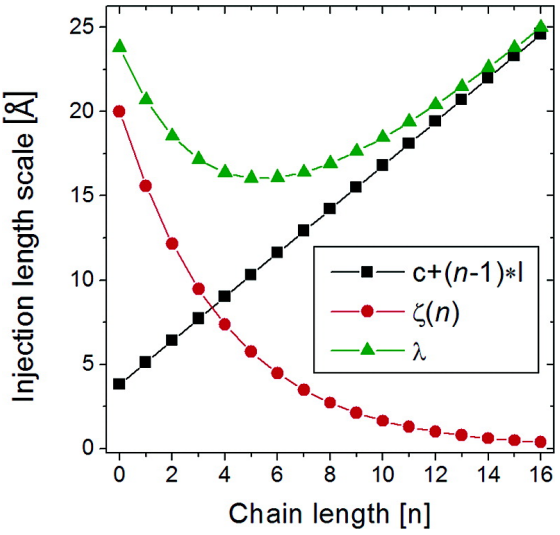

Fig.3. 5 Terms contributing to the effective length scale for injection λ (green triangles). The values for the *c+(n-1)l* term (black squares) were taken from [39] and *ξ(n)* term is modelled by an exponential decay (red circles). [30]

Asadi and co-workers in 2012 [32] combine the electrical measurements of large-area molecular junctions and OFETs to demonstrate the real effect of SAM in the field-effect mobility of a transistor.

The total resistance of the transistor is the sum of the channel resistance and the contact resistance; a SAM-functionalized OFET can be treated as a metal–insulator–semiconductor (MIS) tunnel junction and it can be approximated as a metal-insulator-metal (MIM) tunnel junction at high gate bias, like the large-area molecular junctions. For this reason, they add the absolute value of the SAM resistance, calculated with two terminal

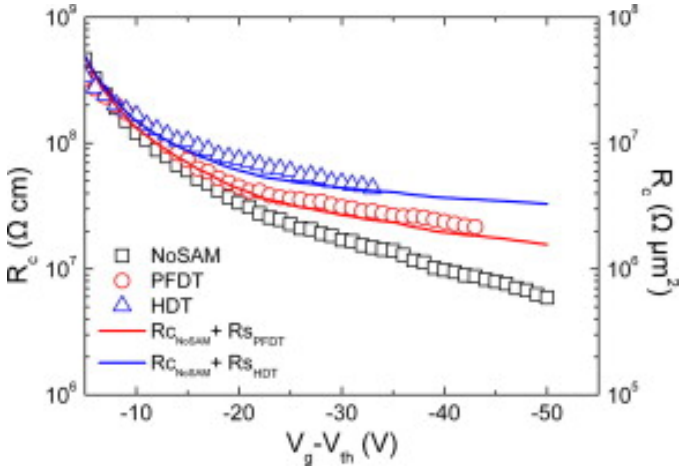

Fig.3. 6 Contact resistance of BG/BC transistors with bare Au Au/PFDT treated electrode as a function of gate bias. The experimental points derive from transmission line measurements using various channel lengths and corrected for threshold voltage shift. The solid lines represent the summation of the tunnel resistance of the corresponding SAM in molecular junction with the contact resistance of the transistor with bare Au electrodes. [32]

large-area molecular junctions, as a series resistance to the total resistance of a BG/BC untreated transistor (calculated with TLM using various channel lengths).
As shown in Fig.3.6; the validity of the above mentioned analysis is confirmed by the good agreement between experimental data (red triangles and blue circles) and the calculated solid lines. This unambiguously demonstrates that SAM acts as tunnelling resistances coupled to the channel resistance.
Within this context, we use pentacene-based OFET in BG/BC configuration as test-beds for the electrical characterization of SAM sandwiched between Au electrodes and the organic semiconductor.
Different sets of SAM were tested; each of them was designed varying one of the following criteria: (i) the chain-length, (ii) the head or tail groups.

3.3 OFETs as charge injection organic gauge applied to Oligothiophene SAMs

Here, we have investigated how the charge injection is affected by the presence of the oligothiophene-based SAMs in a real device and we experimentally proved that the exponential decay β measured from OFET is in agreement with other systems, such as molecular junctions (metal–insulator–metal).
This first set of molecule (Fig.3.7) are π- conjugated alkanethiol, Tn-C8-SH, with an increasing number of thienyl units from n = 1 to n = 4 bound to an octane-1-thiol tail.

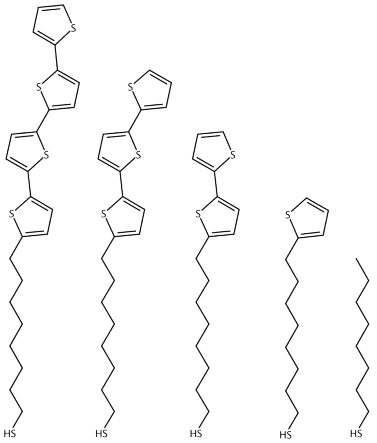

Fig.3. 7 Chemical structure of oligothiopene SAM

3.3.1 Electrical characterizations

The typical transfer characterization is displayed in Fig.3.8 and gives a complete view on the electrical performances of the corresponding OFETs.
The pristine and C8-SH functionalized OFETs are not contact-limited and they show smaller I_{DS} errors with respect to ones modified by Tn-C8-SH (n = 1. . .4. Transfer characteristics show a progressive decrease of I_{DS} current by increasing thiophene units together with a shift of the turn-on voltage and a decrease in *SS*. The linear region of the output characteristics shows a progressive worsening of the ohmic behaviour and T4-C8-SH-induces even hysteresis.

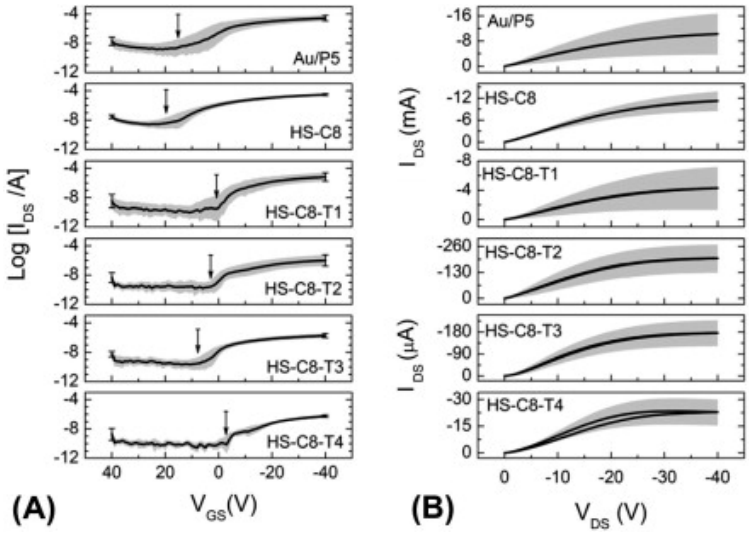

Fig.3. 8 Transfer and Output characteristic dataset. Continuous lines are mean trends.

As previously mentioned, the exponential dependence of parameters, like field-effect mobility, is the main focus of this activity. Fig. 3.9 shows the μ values extracted from the transfer characteristics in linear and saturation regime as a function of the number of thienyl units. It clearly exhibits an exponential decay from C8-SH (n = 0) to T4-C8-SH (n = 4). The exponential decay factor, β, was extracted from the slope of the linear fitting of the log-lin plot (see Fig. 3.9).

The inverse length scale β turns out to be 0.24(±0.01) Å^{-1} in the linear regime and 0.17(±0.02) Å^{-1} in saturation regime.

This is consistent with the data in literature [31,33] for π-conjugated molecules (0.2 to 0.6 Å^{-1}) confirming the through-bond charge tunneling mechanism.

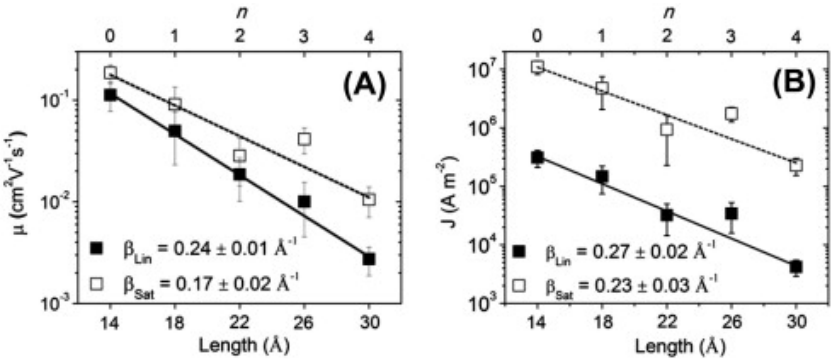

Fig.3. 9 Exponential decay *vs* SAM thickness (bottom axis) and number *n* of thienyl units of the chain (top axis). The molecular length has been calculated by the sum of the C8-SH (14 Å) plus 4 Å for each thienyl units calculated by dividing the length of sexithienyl by six.[59,60](A) Field-effect mobility and (B) current density; full squares and empty squares correspond in both cases to linear and saturation regimes respectively.

The absence of a clear odd–even effect suggests that straight oligothienyl linear chains dominate, sigma bond isomerization is negligible within the molecules in the SAM, and there are no substantial differences in tilt angle along the homolog series.

As comparison, we have extracted from the output characteristics the current density J, by dividing the I_{DS} current (in both regimes) by the effective injection area A_{eff}.

This is calculated by multiplying the channel width W by the pentacene thickness h (4.5 nm according to [34])effectively involved in charge transport.

The current density is estimated at V_{GS} = -40 V, for V_{DS} = -1 V and V_{DS} = -40 V corresponding to linear and saturation regimes respectively. The exponential decay β measured from the current density for both regimes matches the values extracted from the charge mobility (0.27 and 0.23 Å^{-1} for linear and saturation regime respectively).

The FET current (I_{DS}) depends on three in-series resistors arising from source and drain interfaces with the organic semiconductor (R_{SD}), and from the resistance of the channel (R_{ch}),

$R = R_{ch} + R_{SD}$ Eq. 3.3

There are different ways for the extraction of the contact resistance, viz. transfer line method (TLM)[35], gated four-probe measurements [36] and local potentiometry.[37]

We have evaluated the effective resistivity of our devices through the relationship:

$R \times W = (V_{DS}/I_{DS}) \times W$ Eq. 3.4

In linear regime, the contact resistance will be larger compared with the saturation regime.. As shown in Fig. 3.10, the trend of the effective resistivity is clearly exponential. In order to extract the parameter, we fit the resistivity according to two schemes:

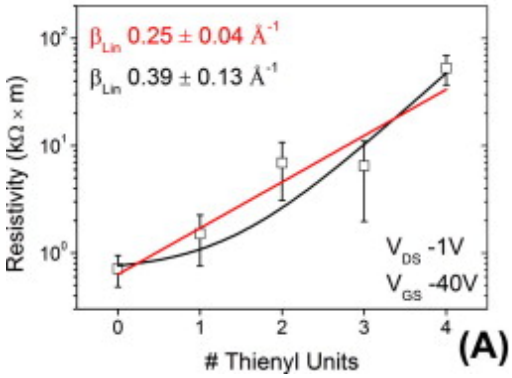

Fig.3. 10 Plot of the resistivity vs SAM length. The red line correspond to the exponential fit, the black one is an exponential fitting with an offset as described in the text.

(i) with an exponential function $R \times W = R_0 \exp(\beta n)$, where R_0 is the resistivity related to n = 0. This first approach yields R_0 x W=0.6(±0.2) kΩ m and β=0.25± 0.04 Å^{-1} matching the value extracted from both the mobility μ and the current density J *vs* number of thienyl units. This kind of fit however, cannot allow us to identify the two distinct contributions of source and drain electrodes.

(ii) with the phenomenological fit function $R \times W = R_{ch} + R_0 \exp(\beta n)$. Here R_{ch} can be estimated as $R_{ch} = L/[W \mu_{lin} C_d (V_{GS}-V_{th})]$ where the pentacene charge mobility μ_{lin} should be taken in the absence of the electrodes. For μ_{lin} = 0.1–1 cm^2/(V s), R_{ch} x $W \approx$ 0.05–0.5 kΩ m. The best fit of the data in Fig. 3.10 yields: R_{ch} x W = 0.7(±0.3) kΩ m, R_0 x W = 0.08(±0.2) kΩ m and β = 0.4(±0.1) Å^{-1}. Such β value is in agreement with the other measurements and it is a direct evidence of the control exerted by the charge injection interfaces on the overall current.

3.3.2 Wettability measurements and AFM analysis

A contact angle study on SAMs-treated surface was our first assessment of SAMs quality. Using different solvents such as bi-distilled water, ethylene glycol and nitromethane, it has been extracted the adhesion work, W_A, which has been plotted vs. the number of thienyl units (as you can see in Fig. 3.11).

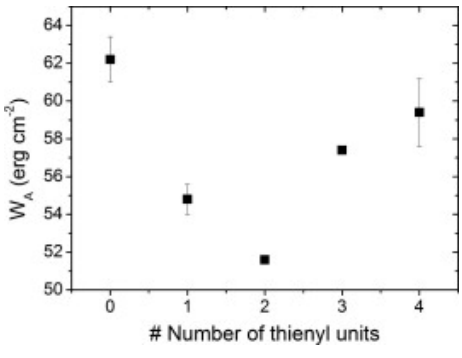

Fig.3. 11 Work of adhesion plotted against the number of thienyl units.

An abrupt decrease of W_A occurs to the addition of the first thienyl group (from n = 0, C8-SH, to n = 1, T1-C8-SH). Looking at the overall plot, it is shown a non-monotonic behaviour featuring a minimum centered at n = 2 (T2-C8-SH) and a maximum at n = 0 (C8-SH).

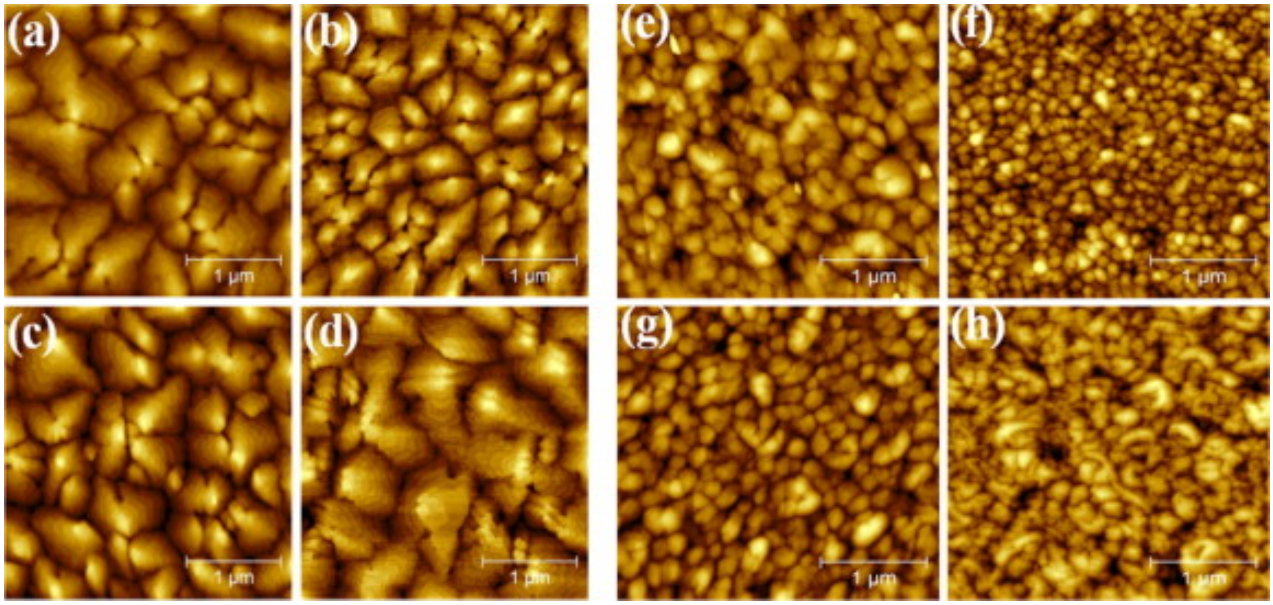

Fig.3. 12 Morphology of pentacene 10 ML thick. (a-d) pentacene on channel, (e-h) pentacene on Au electrodes. (a)(e) T1-C8-SH, (b)(f) T2-C8-SH, (c)(g) T3-C8-SH and (d)(h) T8-C8-SH.

The morphology of the pentacene thin-film has been verified on SAM-functionalized electrodes and on gate dielectric (Fig.3.12).

The images were analysed by means of HHCF ($H(\tau)$) where τ is the distance between two points of the image and we plot the saturated roughness σ_{rms}, the roughness exponent α and the correlation length ξ *vs* the number of thienyl units (as described in Chapter 2.2.3); the graphs are shown in Fig.3.13.

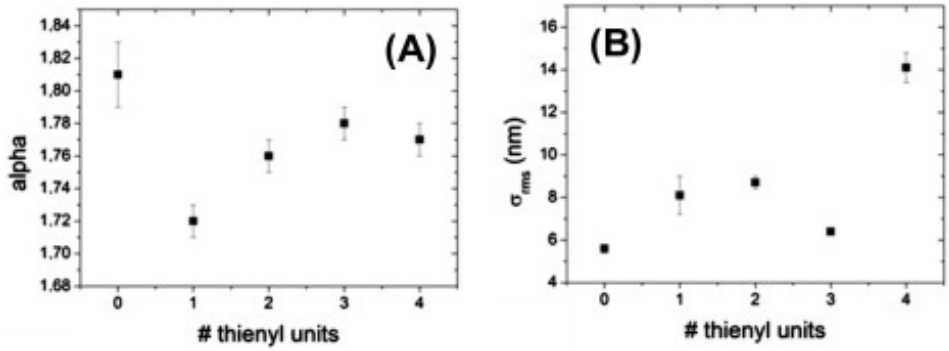

Fig.3. 13 Alpha coefficient (A) and saturated roughness (B) plotted vs thienyl units.

The first two parameters turn out to be dependent on the different SAMs, on contrary ξ does not resolve the different SAMs due to high deviation standards.

The pentacene morphology in the channel is invariant for all the devices, because the oligothiophene molecules are not able to modify the silicon oxide surface.

3.4 OFETs as charge injection organic gauge applied to hydrophilic SAMs

A second homolog series of organic molecules was employed onto S/D electrodes of OFETs in order to study the charge injection at metal/SAM/OS interface. We used a set of linear alkanethiols terminated with a hydroxyl group ($HS(CH_2)_n$ OH with n = 3, 4, 6, 8, 9, 11) in order to change in a systematic way the thickness of the charge injection barrier (Fig.3.14).

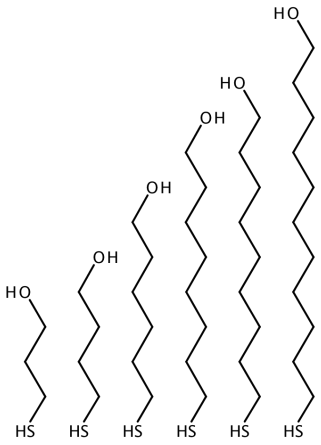

Fig.3. 14 Chemical structure of hydrophilic SAM series

3.4.1 Electrical characterizations

All devices have been electrically characterized *ex-situ* in both vacuum and air. Pristine TFTs (indicated as n = 0, bare Au contacts) have been taken as benchmark.

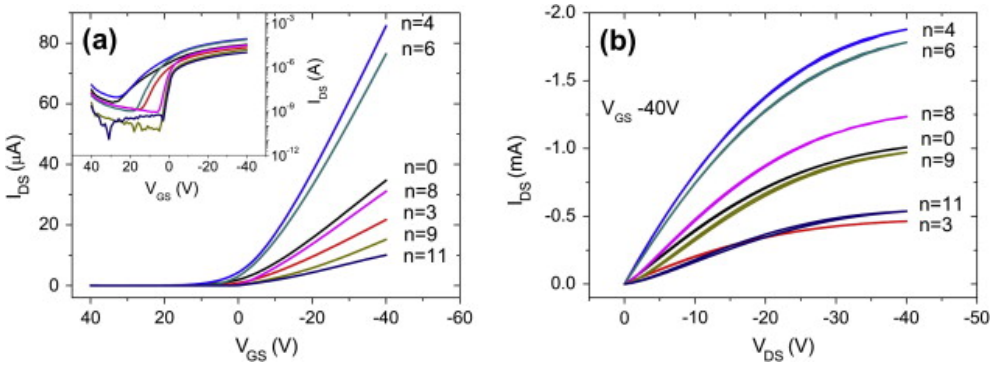

Fig.3. 15 Transfer (a) and output (b) characteristics of OTFTs with S/D electrodes modified by hydrophilic SAMs

The shortest SAM (n = 3) worsens the electrical performances of the device, as shown in either the I–V transfer or the output characteristics (Fig.3.15). Conversely, SAMs with four and six methylene units (n = 4 and n = 6) yield ohmic contacts and consequently improve the I_{DS}.

For n > 6, the electrical behaviour worsens likely due to the systematic thickening of the charge-injection barrier. The non-linear trend of I–V output characteristics [14] for low V_{DS} (<5 V) suggests the presence of contact resistances for n = 0, 3, 8, 9, 11.

As previouslyshown for both alkanethiol [30]and oligothienyl-based [38] SAMs, μ could be fitted by Eq. 3.1.

The same non-monothonic trend is shown in Fig.3.16 for the current density (J) and the total resistivity (ρ). We calculated J as reported in the previous paragraph for oligothiophene series, whereas the total resistivity, ρ, is

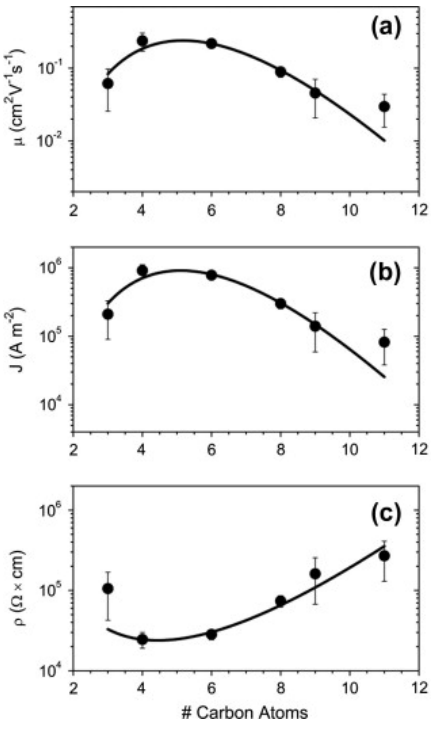

Fig.3. 16 Log-lin plot for (a) mobility, (b) current density and (c) resistivity *vs* number of CH_2 units in linear regime (V_{DS} = -1)

calculated using the relationship: $V_{DS}/(Jh)$.

The exponent β is 1.1(±0.3) Å^{-1}, 1.2(±0.3) Å^{-1} and 0.7(±0.2) Å^{-1} for mobility (β_μ), current density (β_J) and total resistivity (β_ρ), respectively. They are calculated by fixing the length of a CH_2 unit to 1.2 Å^{-1} [39]. Within the experimental error, β_μ, β_J and β_ρ are in agreement with the values reported for a series of hydroxyl-terminated alkanethiols (β = 0.75 Å^{-1}) [40].

Pentacene is moderately stable to oxygen and humidity [41–43] and thus several humidity sensor based on pentacene-TFT are reported in literature [44]. As shown in Fig. 3.17, the reference device exhibits a charge mobility drop equal to $\mu_d = (\mu_{vac}-\mu_{air})/\mu_{vac}$ when exposed to ambient conditions (relative humidity of 45%). The drop ranges from 50% to 60% for linear and saturation regimes, respectively. The integration of the hydrophilic SAMs gives rise to a non-monotonic trend: intermediate SAM lengths (n =4 and 6) appear less sensitive to the humidity ($\mu_d \approx 30\%$), with respect to the shorter and longer SAM lengths (n = 3, 8, 9 and 11) where μ_d ranges from 55% to 80%.

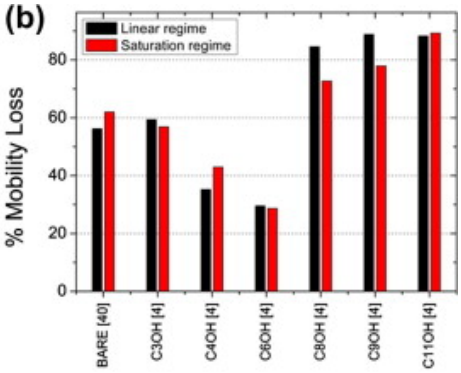

Fig.3. 17 Percentage drop of the charge mobility in devices exposed to 45.6% relative humidity. Black and red bars refers to linear and saturation regimes.

As suggested by Horowitz et al.[45], the I_{DS} current can be corrected by the contact resistance using Eq. 3.5:

$$I_{DS} = \frac{W}{L} C_i \mu (V_{GS} - V_{th})(V_{DS} - I_{DS}R_C) \qquad \text{Eq. 3.5}$$

where R_C is the in-series contact resistance and all the other parameters have the usual meanings.

Fig. A1 in Appendix A shows the R_C behavior for the homolog series of hydrophilic SAMs and it is independent to the V_{GS} except for the lower ones. The R_C values extracted from the linear fit for high V_{GS} (> -10V) are listed in Table 3.1.

Molecules	R_C **(Ω)**
Bare	1.06 (±0.04) x 10^6
C3OH	1.90 (±0.04) x 10^6
C4OH	4.3 (±0.1) x 10^5
C6OH	5.2 (±0.1) x 10^5
C8OH	1.2 (±0.4) x 10^6
C9OH	2.2 (±0.1) x 10^6
C11OH	3.2 (±0.2) x 10^6

Table 3. 1 R_C values extracted as reported by Horowitz et al. [45]

The R_C behavior for C4OH and C6OH accounts for the highest mobility values reported previously.

3.4.2 Electrochemical measurements and AFM analysis

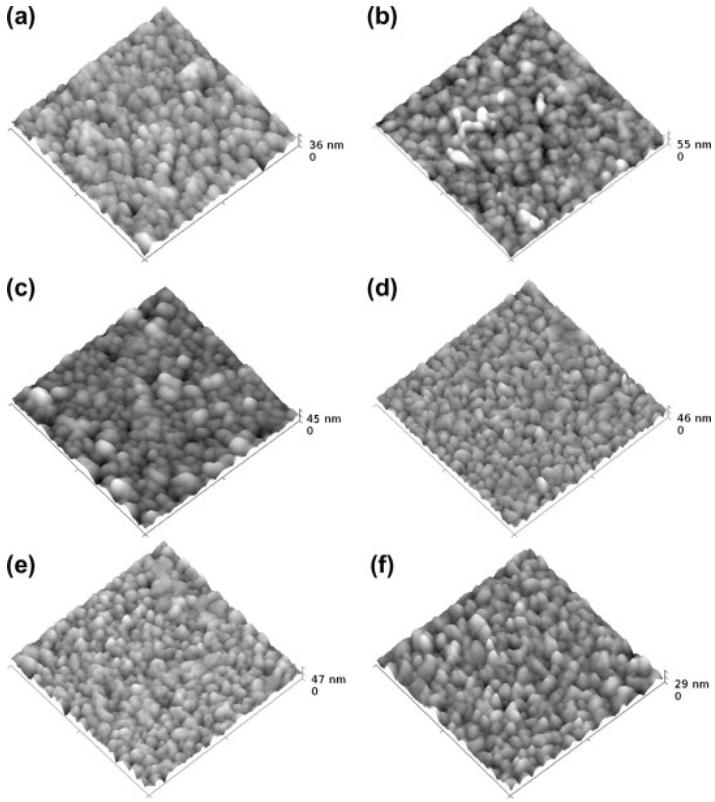

Fig.3. 18 AFM images of pentacene thin-film on Au electrodes functionalized with $HS(CH_2)_nOH$ with n=3 (a), n=4 (b), n=6 (c), n=8 (d), n=9 (e) and n=11 (f).

The improved stability towards humidity showed by intermediate SAMs (n=4 and 6), was investigated also through AFM imaging (Fig.3.18). In literature, sensing mechanism of pentacene-TFT is usually associated with grains density and shape in the channel whereas the morphology of electrode is neglected. By the usual HHCF analysis, we have extracted three morphological descriptors: σ_{rms}, α and ξ. Pentacene films on SAM-coated electrode have constant σ_{rms} equal to 5.0±0.3 nm, and they are composed by small grains. Accordingly to the literature, bigger grains means lower amount of grain boundaries by conferring higher stability to the device towards air exposure [46][47]. ξ is intrinsecally associated to the grain size, because it depends on alkanethiols. In our experiments, ξ shows a maximum value for n=4 and 6 (Fig. 3.19). The roughness exponent α has high values, proving that the pentacene film on gold is rather rough. [48]

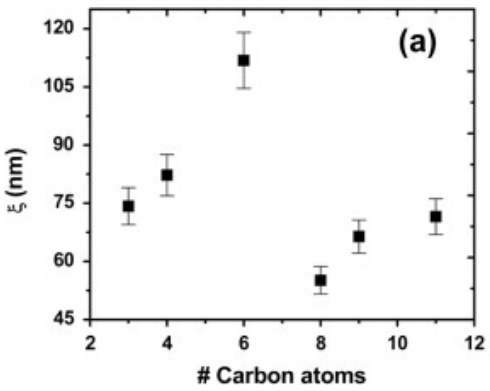

Fig.3. 16 Lateral correlation length is plotted vs the number of methylene units.

Regarding to electrochemical characterization, cyclic voltammetry shows a progressive distortion of the ferricyanide redox signal by increasing the SAM thickness due to a better coverage and packing. As a result, the ΔE_p ranges from 71 mV to 569 mV for n = 3 up to n = 8 respectively. The peak-to- peak distance relative to thicker SAMs is not available because of the complete quenching of the ferricyanide signal (see Fig. 3.20(a)). Accordingly, the impedance spectroscopy shows a

progressive increase of the charge transfer resistance R_{CT} between our redox probe, $[Fe(CN)_6]^{3-/4-}$ and Au electrode.

The Nyquist plots have been successfully fitted thanks to an equivalent circuit, composed by a solution resistance (R_S), a constant phase element (CPE), a charge transfer resistance (R_{CT}) and the Warburg element (W), as shown in the inset of Fig. 3.20(b). The charge transfer resistance progressively rises as a function of the SAM thickness.

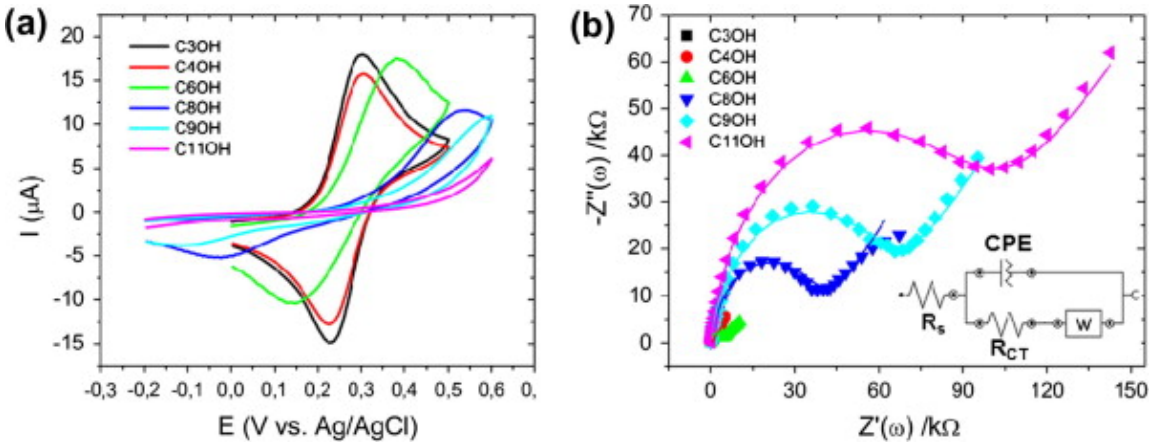

Fig.3. 17 Cyclic voltammetry (a) and impedance spectroscopy (b) for each functionalization in a 5mM $[Fe(CN)_6]^{3-/4-}$ and 2M KCl

3.5 OFETs as charge injection organic gauge applied to Oligoarylenes SAMs (I)

The CIOG sensitivity was well demonstrated with the above-mentioned works (viz. alkanethiols [30], hydroxyl terminated ones [49] and oligothiophene set [38]) This further work, in conjunction with other extensive investigations reported in literature, is based on the systematic investigation of structural and electronics properties of SAMs bearing different anchoring/terminal groups (see Fig.3.21)..

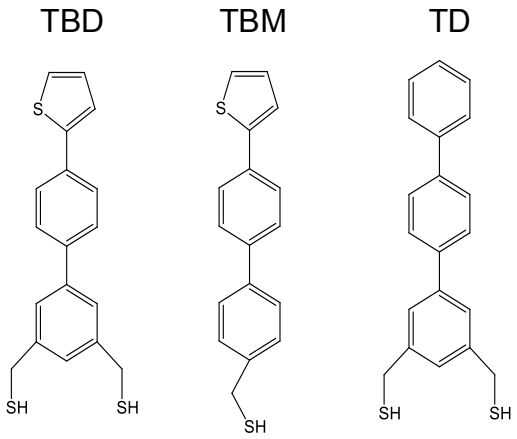

Fig.3. 21 Chemical structure of the three oligoarylenes SAM.

The molecules are three linear oligoarylenes featuring different functional groups at both ends (Fig. 3.21). We synthesized and characterized self-assembled monolayers of (40-(Thiophen-2-yl)Biphenyl-3,5-diyl) Dimethanethiol (TBD), (40-(Thiophen-2-yl)Biphenyl-4-yl)Methanethiol (TBM), and ([1,10;40,100]Terphenyl-3,5-diyl)Dimethanethiol (TD).

3.5.1 Electrical characterization

A complete electrical characterization was performed on more than 40 bare devices and more than 10 devices modified by these SAMs. From the transfer characteristics (see Fig. 3.22), we extracted charge mobility μ, and threshold voltage V_{th} in vacuum and in air (Table 3.2).

SAM	μ (cm²/V s)	V_{th} (V)
Bare Gold	0.11 (±0.06)	−3(±4)
TBD	0.011(±0.08)	−21(±3)
TBM	0.06(±0.04)	−12(±1)
TD	0.06(±0.03)	−17(±3)

Table 3. 2 Electrical parameters extracted from transfer characteristics for the untreated device and for the three devices modified by oligoarylene SAM.

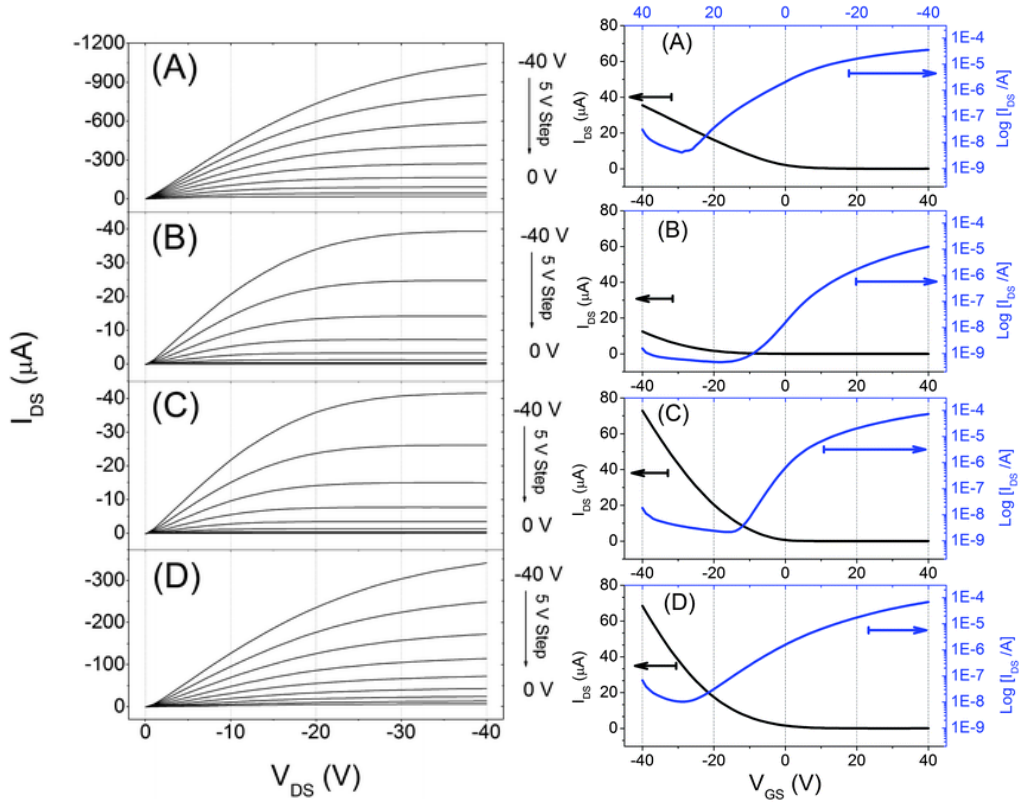

Fig.3. 22 Output (left) and transfer (right) characteristics for the bare device (A) and for the three functionalizations: TBD (B), TBM (C) and TD (D). Transfer characteristics are in linear regime at V_{DS} =-1V for bare and V_{DS} = -5V for treated OTFTs.

OTFTs performance were evaluated by defining two OTFTs benchmarks: (1) bare electrodes for assessing the SAMs effect on the electrical performances and (2) electrodes functionalized by the TBD-based SAM, for evaluating the electrical differences induced by the anchoring/ terminal group replacement (TBM and TD SAMs respectively).

The charge-mobility is constant within the error bars to different SAMs but V_{th} undergoes a marked negative shift for each SAM with respect to the bare Au. These first results are insufficient to unravel the actual role of the SAM since extrinsic effects related to the different steps of surface treatment might enter into play.

The output characteristics (see Fig. 3.22) are very helpful to get insights about the electrical contacts between the electrodes and the organic semiconductor. The highest drain–source current I_{DS} (measured for V_{GS} and V_{DS} equal to −40 V) reaches 1 mA for OTFT with bare gold contacts, whilst for OTFTs with TBD and TBM get to some tens of mA and the TD about 300 μA. Marked I_{DS} distortion can be observed for all SAMs in a linear regime. Such I_{DS} ripple and drift depend on the increased contact resistances rising from the SAM functionalization of electrodes.

A quantitative description of the interface (metal–SAM– organic semiconductor) can be provided by calculating the current density *J* through the source–drain electrodes (see Fig. 3.23).

Other experimental measurement setups, such as large-area molecular junctions, scanning probe microscopies or hanging mercury drop electrode junctions [50] have been used to calculate the current density through self-assembled monolayers. For instance, in large-area molecular junctions the current density, *J*, is measured as a function of the SAM thickness. [51] To extract this last parameter, I_{DS} of the output characteristics (Fig. 3.22) for each V_{GS} value (from 0 V to −40 V with steps of −5 V in our experiments) was divided by the size of the charge injection area (4.5 nm thick [34], hence the charge injection areas are 50 and 100 μm² for the two test pattern geometries).

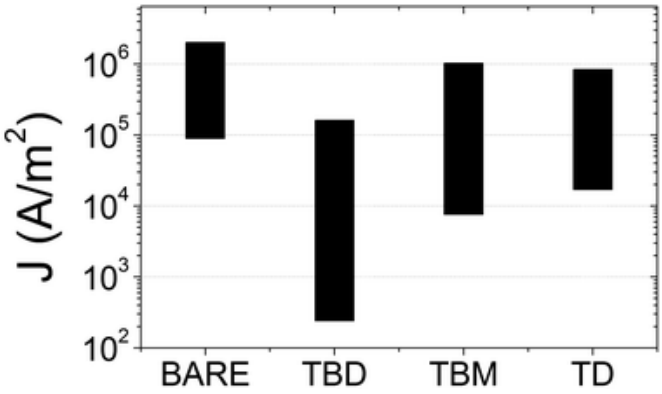

Fig.3. 23 The current density vs different functionalizations is shown.

In this experiment, the SAM thickness is kept constant; therefore *J* is affected only by the nature of the anchoring and/or capping groups. Compared to the OTFT with bare electrodes, the one functionalized by TBD-based SAM allows a fine tuning of ultra-low current densities spanning more than two orders of magnitude. TBM and TD show narrower current ranges, featuring values closer to the bare OTFT, which means a progressive loss of control relative to the ultra-low currents.

As already described in literature, the BG/BC architecture is usually affected by higher contact resistances compared to the BG/TC architecture. [52] Although this phenomenon is one of the most important drawbacks for technological applications, it offers the possibility to get important insights about our SAMs effect on the electrical behaviour. Here, we have extracted the total resistance *R,* namely the sum of both channel and contacts resistances, from the output characteristics, varying the gate–source voltage from +5 V to −40 V (with steps of 5 V) at a fixed drain–source voltage of −5 V for each functionalization.

The general trend, displayed in Fig.3.24 in terms of resistivity, features an exponential transition from a high resistive behaviour ($V_{GS} > V_{th}$ relative to an off state) and a low resistive one ($V_{GS} < V_{th}$ relative to the on state).

This trend can be phenomenologically fitted by an exponential equation:

$$R = R_{max}\, exp[-(V_{GS} - V_{max})/V_c] \qquad \text{Eq. 3.6}$$

where R_{max} is the maximum resistance at the voltage V_{max}, and V_c is the critical voltage at which the total resistance is reduced to 63% of the initial value (i.e. R_{max}).

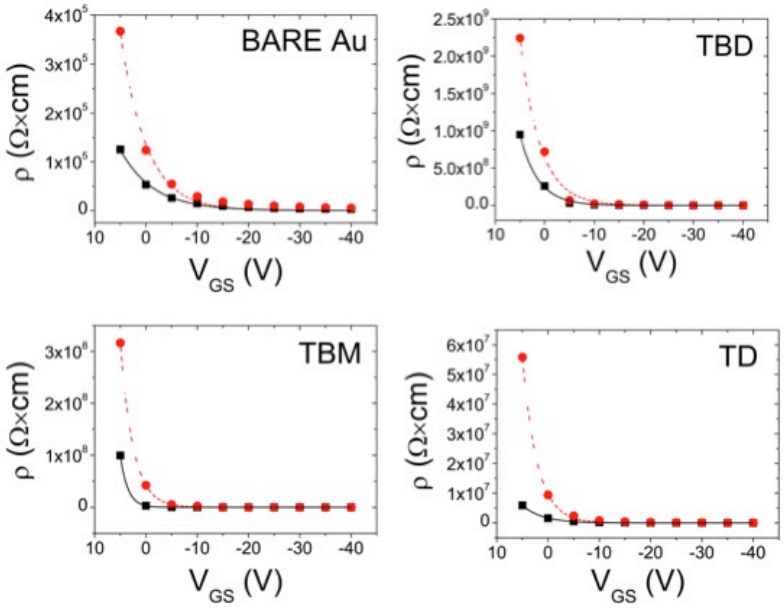

Fig.3. 24 Resistivity *vs* V_{GS} behaviour for each kind of device. Black squares and red dots are relative to L = 20 μm and L = 40 μm.

The transition from depletion to accumulation regime can be experimentally quantified by the resistance drop (ΔR) at the critical voltage (viz. $R_{max}\ exp\ [-1 + (V_{max}/V_c)]$). Table 3.3 summarizes the parameters for the two device geometries. The OTFT functionalized with TBD-coated electrodes compared to the OTFT with bare ones shows marked increase of 3 orders of magnitude in the ΔR (from MΩ x cm to GΩ x cm), whereas TBM and TD show a progressive decrease induced by the structural changes.

SAM	$\Delta R_{L=20}$ (Ω x cm)	$\Delta R_{L=40}$ (Ω x cm)	$V_{c\ L=20}$ (V)	$V_{c\ L=40}$ (V)
None	$1.3\ (\pm0.1)\times10^{5}$	$3.7\ (\pm0.2)\times10^{5}$	-6.5 (±0.4)	-5.1 (±0.3)
TBD	$9.4\ (\pm0.4)\times10^{8}$	$2.2\ (\pm0.2)\times10^{8}$	-3.6 (±0.1)	-4.0 (±0.2)
TBM	$9.9\ (\pm0.3)\times10^{7}$	$3.2\ (\pm0.1)\times10^{8}$	-1.44 (±0.03)	-2.48 (±0.02)
TD	$5.9\ (\pm0.2)\times10^{6}$	$5.6\ (\pm0.1)\times10^{7}$	-3.9 (±0.1)	-2.9 (±0.1)

Table 3. 3 Resistive drop ΔR and critical voltage values obtained from the analysis.

3.5.2 Wettability measurements and AFM analysis

As previously reported for oligothiophene, contact angle investigations were carried out on SAM-coated Au surfaces. The adhesion work, W_A was extracted from the plot of $\cos\vartheta$ *vs* $1/\gamma$, in which γ is the surface energy. W_A results sensitive to the change of the terminal group (thienyl or phenyl group) and this proves the compact ordering of the three SAMs regardless of the

number of anchoring groups (Table 3.4).

SAM	W_A (erg cm^{-2})
None	55 (±2)
TBD	47 (±2)
TBM	48 (±2)
TD	53 (±1)

Table 3. 4 Work of adhesion measured for each SAM on polycrystalline gold.

The morphology of pentacene grown on Au electrodes has been directly investigated by AFM on the device electrodes (see Fig. 3.25) and was performed the same morphological analysis based on $H(\tau_x)$. Table 2 shows relevant morphological parameters extracted.

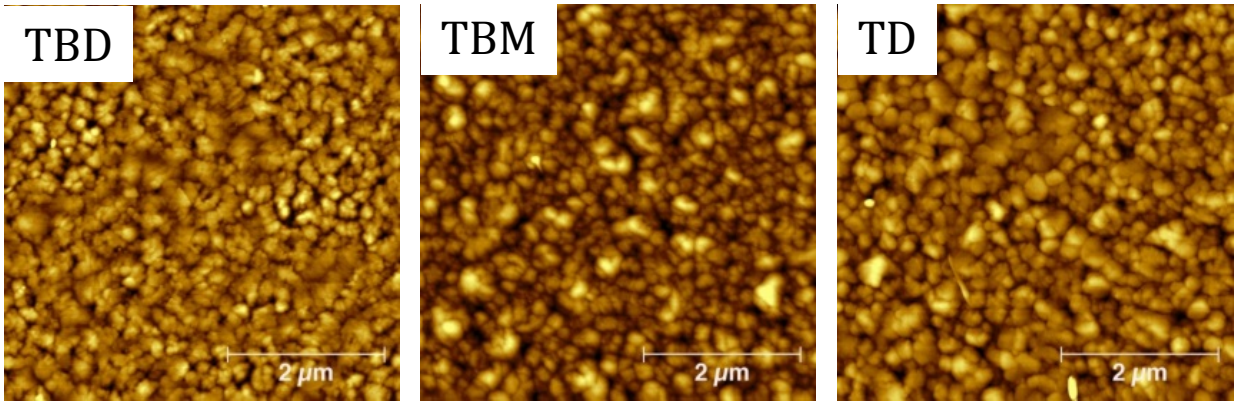

Fig.3. 18 AFM images of pentacene thin-film on SAM-coated electrodes.

Firstly, on bare Au the pentacene film is morphologically characterized by small grains with high aspect ratio. This film has comparable ξ_1 (70 ± 10 nm) with respect to the film grown on TBD-coated Au (70 ± 20 nm). Notably, the latter one turns out to be smoother, as indicated by the lower σ_{rms} and a higher α_1, respectively, than the film grown on bare Au. [48]
Moving from TBD to TBM/TD, a marked increase of the grain size in both bi- and tridimensional direction can be observed (see also Table 3.5). This effect leads to a decrease of α_1 and an increase of σ_{rms}. In addition, pentacene grown on these two SAMs shows a second correlation length (ξ_2) of around 5 nm (Table 4).

SAM	σ_{rms} (nm)	α_1	ξ_1 ($\times 10^{-8}$ m)	α_2 (nm)	ξ_2 (nm)
None	9.3(±0.5)	0.79(±0.01)	7(±1)	/	/
TBD	7.7(±0.3)	0.90(±0.01)	7(±2)	/	/
TBM	11.6(±0.5)	0.85(±0.01)	10(±3)	0.67(±0.01)	5(±9)
TD	12.9(±0.7)	0.77(±0.01)	10(±3)	≈0	5(±2)

Table 3. 5 Scaling parameters for the AFM images relative to P5 thin-film on SAM-coated Au electrodes.

3.5.3 Electrochemical measurements

Comparing the electrochemical behaviour of a redox couple between a bare electrode and a SAM-coated electrode, important information on SAM packing and on its ability to block the

redox reaction can be extracted.

Fig. 3.26 shows the cyclic voltammograms recorded for the $Fe(CN)_6^{3-/4-}$ couple on a bare gold electrode and on the same electrode functionalized with the three SAM at increasing incubation time.

After 7h cathodic and anodic signals disappears completely and similar behaviour was obtained for TD and TBM SAMs proving the high quality of the monolayers.

The three SAMs show different kinetic behaviour, therefore TBM and TBD slow down the Au passivation compared to TD SAM probably due to the presence of the sulphur atom at the terminal group.

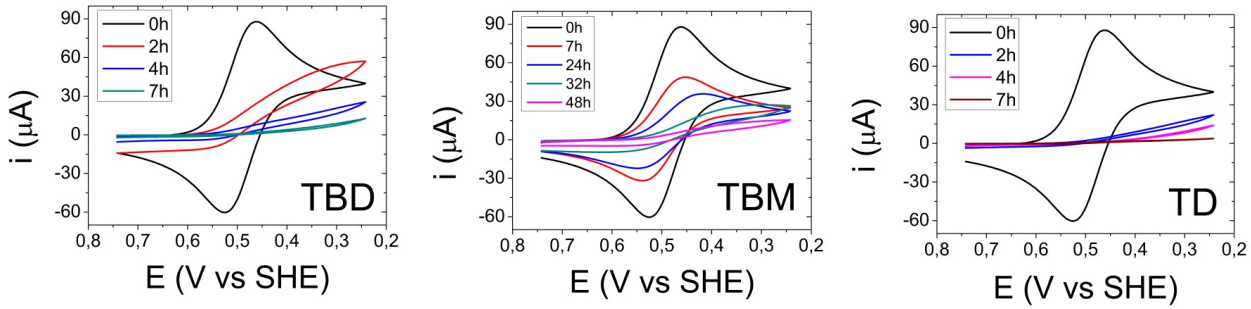

Fig.3. 26 Cyclic voltammograms for each SAM as a function of the incubation time. CV are obtained at 0.02 V s-1 for 5 mM $Fe(CN)_6^{3-/4-}$ and 2M KCl

3.6 OFETs as charge injection organic gauge applied to Oligoarylene SAMs (II)

Another set of linear oligoarylenes (Fig.3.27) featuring different functional groups was studied: (i) 4-methoxy-terphenyl-4′′-methanethiol (MTM), (ii) 4-methoxy- terphenyl-3′′,5′′-dimethanethiol (MTD), (iii) 4-nitro-terphen- yl-4′′-methanethiol (NTM), and (iv) 4-nitro-terphenyl-3′′,5′′- dimethanethiol (NTD). They share the main backbone (three phenyl rings) and they different for head/tail groups.

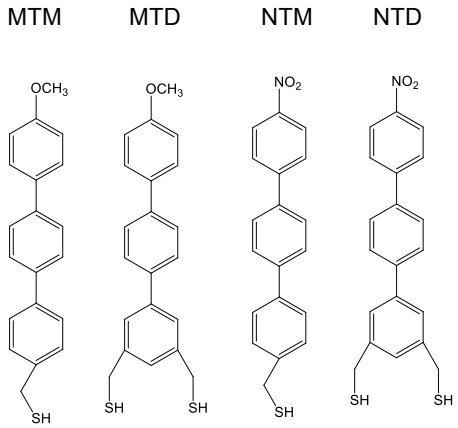

Fig.3. 27 Chemical structure of MTM, MTD, NTM and NTD SAMs.

3.6.1 Electrical characterization

OFETs have been prepared by the following protocol: i) a first treatment with hexamethyldisilazane (HMDS) vapours overnight i to passivate the SiO_x dielectric surface and ii) the usual protocol described in the paragraph 2.1.4.

Devices with only HMDS functionalization were taking as references and they show mobility of 0.41 (±0.04) $cm^2\ V^{-1}\ s^{-1}$, threshold voltage of 7 (±2) V, and a negligible bias stress. SAMs deposition lasts 72h and devices only immersed in CH_2Cl_2 were studied to verify the solvent effect. The organic solvent treatment slightly decreases the electrical performances, featuring a mobility of 0.13 (±0.03) $cm^2\ V^{-1}\ s^{-1}$ and threshold voltage of 0 (±1) V. This is probably due to the introduction of traps within the channel (Fig.3.28).

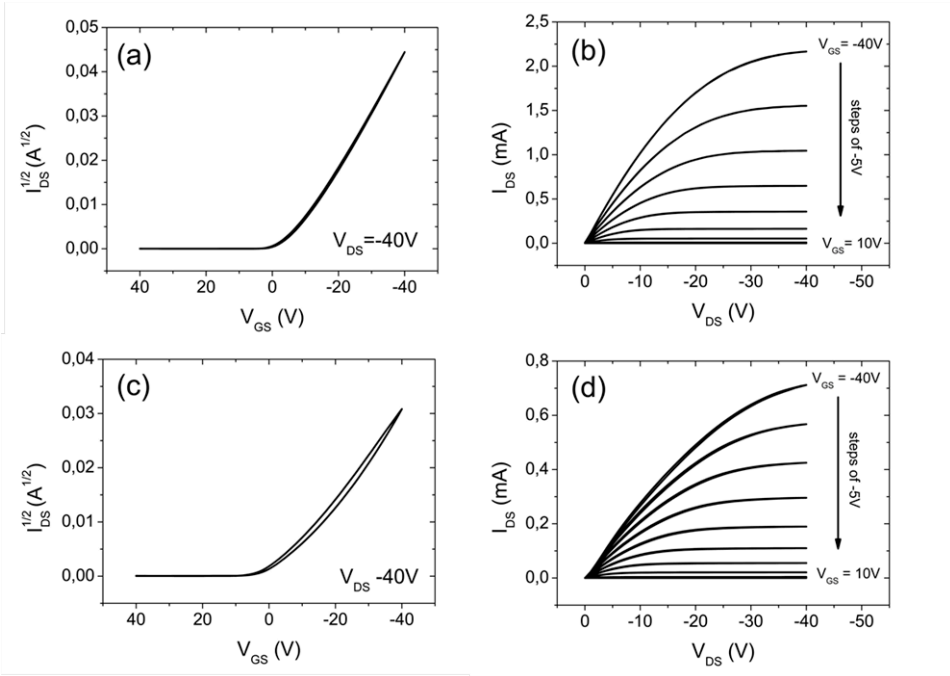

Fig.3. 28 Transfer (a and c) and output (b and d) characteristics of reference OFET (a and b) and after CH_2Cl_2 immersion (c and d).

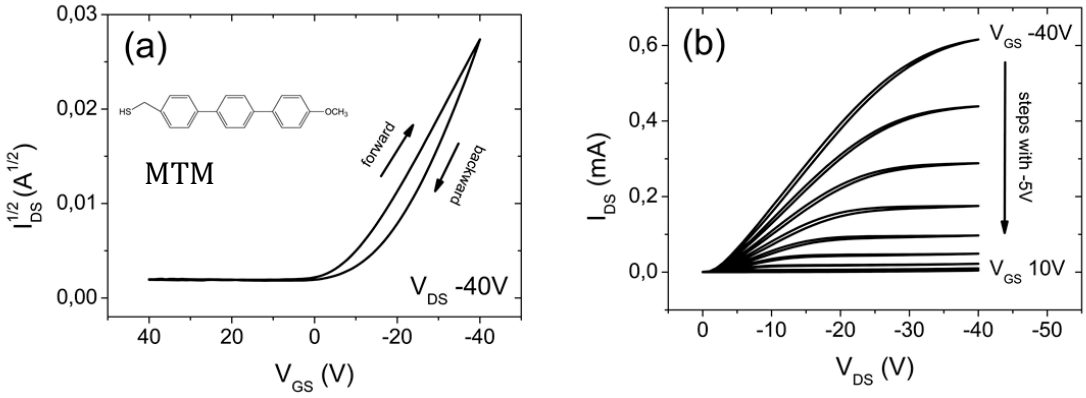

Fig.3. 29 Transfer (a) and output (b) characteristics for OFET functionalized by MTM.

The output characteristics of the MTM-coated OFETs clearly display how the insertion of SAM at the metal-organic interface worsens the charge-injection and affects the ohmic behaviour in the linear regime of the output characteristics. Fig.3.29 shows the electrical performances for MTM SAM (MTD, NTM and NTD are not shown).

Mobility is not enough sensitive to discriminate the different SAMs, except for MTD that shows μ values almost 2 orders of magnitude lower than the other ones. However, threshold voltage is sensitive to the chemical nature of the head group at the charge injection interface. As a result, NTM and NTD molecules positively shift the threshold voltage according to an increase of the holes density (Table 3.6). This is ascribable to the electron-withdrawing feature of the NO_2 group with respect to the $-OCH_3$ one. [53]

As previously done for the oligoarylene series, we quantified the resistive drop, ΔR (equal to 63% of R), in terms of the critical voltage, V_c [54] with Eq. 3.6.

The resistive behaviour for NTD SAM is shown in Fig.3.30 and the V_c data for the whole set of oligoarylene are reported in Table 3.6:

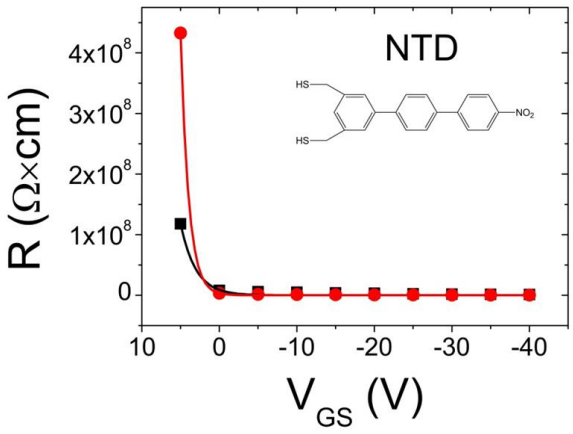

Fig.3. 30 Resistive for OFET functionalized by NTD SAM for smaller (red) and bigger (black) geometry.

SAM	μ ($cm^2V^{-1}s^{-1}$)	V_{th} (V)	$V_{c\ L\ =\ 20\mu m}$ (V)
MTM	0.13 (±0.04)	-6 (±1)	0.91(±0.05)
MTD	0.08 (±0.03)	-9 (±1)	1.22(±0.04)
NTM	0.13 (±0.03)	2.2 (±0.4)	1.4(±0.1)
NTD	0.002 (±0.001)	2 (±2)	1.9(±0.3)

Table 3. 6 μ, V_{th} and V_c are reported for each oligoarylenes

3.6.2 Wettability measurements and AFM analysis

The adhesion work W_A shows highest values for the double-capped thiols (MTD = 55 erg cm^{-2} and NTD = 59 erg cm^{-2}) compared with SAMs having one thiolated legs (MTM = 46 erg cm^{-2} and NTM = 48 erg cm^{-2}) while the nature of the tail group seems do not affect this parameter. Fig. 3.29 shows the W_A plot for NTM and NTD SAMs.

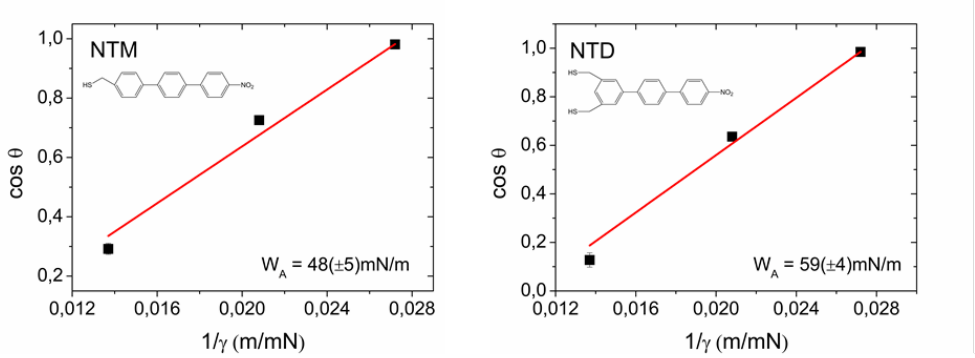

Fig.3. 31 W_A extraction for the two nitro-terminated SAM.

As previously demonstrated, the pentacene morphology is strongly influenced by different SAMs on electrodes..

HHCF analysis of AFM images (Fig. 3.32) provides our usual morphological descriptors of OS growth: the root- mean-square roughness, σ_{rms}, (ii) the lateral correlation length, ξ, and (iii) the roughness exponent, α.

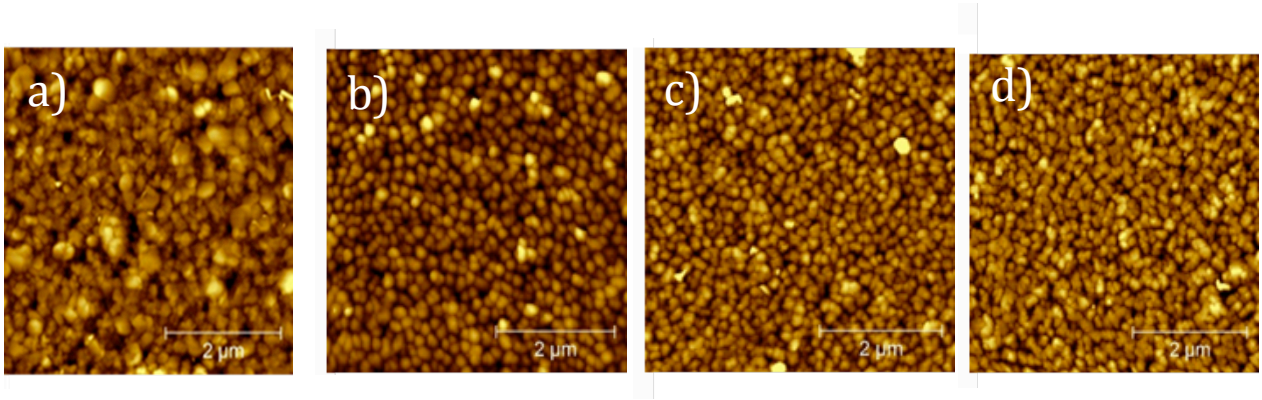

Fig.3. 32 AFM images (5x5 µm²) of pentacene thin-film on S/D electrodes: a)MTM, b) MTD, c) NTM and d) NTD.

All the estimated parameters are listed in Table 3.7 and the main result is the appearance of a second correlation length for NTM and MTM, which hints two characteristic length scales for SAMs that have lower W_A.

These evidences also suggest that bidentate SAMs yield pentacene morphology with a single level of order (namely a unique lateral correlation length). The contribution of different head groups emerges from α_2 values, which are higher for NTM than MTM. This means smoother pentacene morphology for $-NO_2$-terminated SAMs than $-OCH_3$- terminated ones.

SAM	σ_{rms} (nm)	α_1	ξ_1 (x 10^{-8} m)	α_2	ξ_2 (nm)
MTM	15.5 ±0.4	0.90 ± 0.01	6.6 ± 0.9	-	-
MTD	10.9 ± 0.1	0.73 ± 0.02	5 ± 2	0.33 ± 0.01	8 ± 7
NTM	11.1 ± 0.2	0.83 ± 0.01	7.2 ± 0.9	-	-
NTD	11.3 ± 0.2	0.72 ± 0.02	9 ± 3	0.58 ± 0.01	4 ±3

Table 3. 7 Scaling parameters extracted from AFM images for the four oligoarylenes.

3.6.3 Electrochemical measurements

As previously done for TBM, TDM and TD SAMs, we monitored the changes in the faradaic current of $[Fe(CN)_6]^{3-/4-}$ as a function of increasing incubation time of the Au electrode. Again a progressive distortion and decrease of the faradaic current relative to redox reaction of the $[Fe(CN)_6]^{3-/4-}$ is observed as a distinctive feature of Au surface passivation (Fig.3.33).

We have adopted an empirical approach to quantify the passivation mechanism occurring at the Au surface by determining an apparent constant k_{pass} by using:

$$\ln i = \ln i_0 - k_{pass}\, t \qquad \text{Eq. 3.7}$$

where t is the incubation time, i_0 and i are the current intensity at a fixed potential value for bare and functionalized Au at time t, respectively. This procedure was repeated for each investigated molecule and the corresponding passivation rate constants, k_{pass}, are reported in Table 3.8

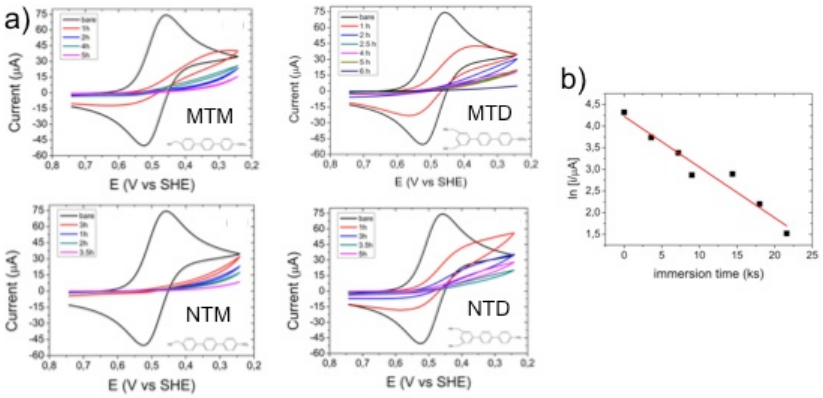

Fig.3. 33 a) CV of the four SAM as a function of immersion time. b) Exponential dependence of the cathodic peak *vs* immersion time.

By comparing k_{pass} of MTM and NTM to MTD and NTD respectively, it is clear that the presence of two −SH groups instead of one slows down the Au passivation.

Considering wettability analysis and electrochemical results, it is reasonable to assume that the presence of two anchoring groups instead of one acts as an additional constraint inducing a different packing arrangement on the surface for mono- and bidentate molecules.

EIS measurements (shown in Fig.3.34) are recorded in 100 mM $NaClO_4$ and 5 mM of $[Fe(CN)_6]^{3-/4-}$, sweeping the frequency from 10^5 Hz up to 10^{-1}Hz, at a potential centered at the E_0 value of ferricyanide with an amplitude of 10 mV.

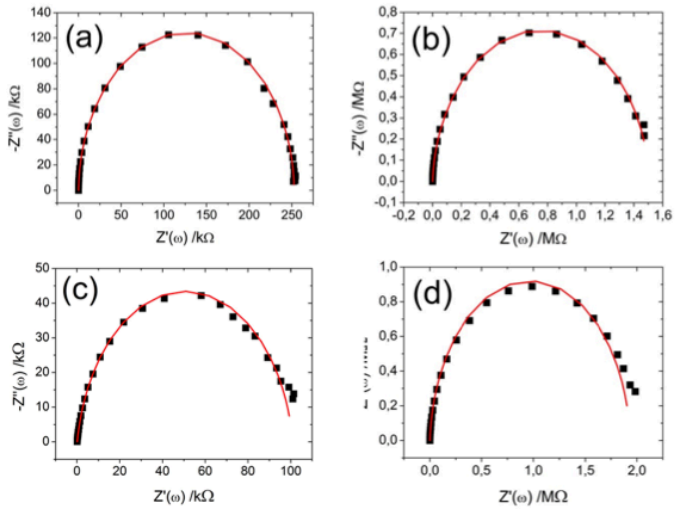

Fig.3. 34 Electrochemical impedance curve for the four oligoarylenes

The equivalent circuit used to fit the Nyquist plots (shown in Fig.3.32) requires only 3 elements: (i) the solution resistance (R_S), (ii) the charge transfer resistance (R_{CT}), and (iii) a constant phase element (CPE), which can be directly translated to the capacitance of the SAM. As already observed for adhesion work and k_{pass}, the R_{CT} values are clearly affected by the number of the anchoring group. In fact, a systematic increase of 1 order of magnitude (namely from hundreds of kΩ to units of MΩ) moving from methanethiol to dimethanethiol is observed.

By exploiting the method of Porter et al. [55][56] (see Appendix B for details), we have used electrochemical desorption measurements to calculate SAMs surface coverage, Γ, the values are listed in Table 3.8

	MTM	**MTD**	**NTM**	**NTD**
k_{pass} (s^{-1})	1.6 (±0.1)×10^{-4}	1.2 (±0.1)×10^{-4}	2.0 (±0.6) ×10^{-4}	0.70 (±0.06)×10^{-4}
C (μF/cm²)	5.0 (±0.3)	5.0 (±0.2)	6.3 (±0.3)	5.9 (±0.3)
Γ x10^{-10} (mol/cm²)	5.3 (± 0.4)	4.8 (± 0.2)	6.0 (± 0.2)	6.1 (± 0.02)

Table 3. 8 K_{pass}, C and Γ values for each SAM obtaine by CV and EIS experiments.

References:

[1] A. Ulman, Formation and Structure of Self-Assembled Monolayers, Chem. Rev. 96 (1996) 1533–1554.

[2] D.H. Kim, Y.D. Park, Y. Jang, H. Yang, Y.H. Kim, J.I. Han, et al., Enhancement of Field-Effect Mobility Due to Surface-Mediated Molecular Ordering in Regioregular Polythiophene Thin Film Transistors, Adv. Funct. Mater. 15 (2005) 77–82.

[3] D.H. Kim, Y. Jang, Y.D. Park, K. Cho, Layered Molecular Ordering of Self-Organized Poly(3-hexylthiophene) Thin Films on Hydrophobized Surfaces, Macromolecules. 39 (2006) 5843–5847.

[4] J. Veres, S. Ogier, G. Lloyd, D. de Leeuw, Gate Insulators in Organic Field-Effect Transistors, Chem. Mater. 16 (2004) 4543–4555.

[5] R. Ruiz, D. Choudhary, B. Nickel, T. Toccoli, K.-C. Chang, A.C. Mayer, et al., Pentacene Thin Film Growth, Chem. Mater. 16 (2004) 4497–4508.

[6] S. Lukas, G. Witte, C. Wöll, Novel Mechanism for Molecular Self-Assembly on Metal Substrates: Unidirectional Rows of Pentacene on Cu(110) Produced by a Substrate-Mediated Repulsion, Phys. Rev. Lett. 88 (2001) 28301.

[7] F.-J. Meyer zu Heringdorf, M.C. Reuter, R.M. Tromp, Growth dynamics of pentacene thin films, Nature. 412 (2001) 517–520.

[8] P. Guaino, D. Carty, G. Hughes, P. Moriarty, A.A. Cafolla, Scanning tunneling microscopy study of pentacene adsorption on Ag/Si(1 1 1)-($\sqrt{3} \times \sqrt{3}$)R30°, Appl. Surf. Sci. 212–213 (2003) 537–541.

[9] I.H. Campbell, S. Rubin, T.A. Zawodzinski, J.D. Kress, R.L. Martin, D.L. Smith, et al., Controlling Schottky energy barriers in organic electronic devices using self-assembled monolayers, Phys. Rev. B. 54 (1996) R14321–R14324.

[10] R.W. Zehner, B.F. Parsons, R.P. Hsung, L.R. Sita, Tuning the Work Function of Gold with Self-Assembled Monolayers Derived from X−[C6H4−C:C−]nC6H4−SH (n = 0, 1, 2; X = H, F, CH3, CF3, and OCH3), Langmuir. 15 (1999) 1121–1127.

[11] S.D. Evans, E. Urankar, A. Ulman, N. Ferris, Self-assembled monolayers of alkanethiols containing a polar aromatic group: effects of the dipole position on molecular packing, orientation, and surface wetting properties, J. Am. Chem. Soc. 113 (1991) 4121–4131.

[12] S.D. Evans, A. Ulman, Surface potential studies of alkyl-thiol monolayers adsorbed on gold, Chem. Phys. Lett. 170 (1990) 462–466.

[13] D.M. Alloway, M. Hofmann, D.L. Smith, N.E. Gruhn, A.L. Graham, R. Colorado, et al., Interface Dipoles Arising from Self-Assembled Monolayers on Gold: UV−Photoemission

Studies of Alkanethiols and Partially Fluorinated Alkanethiols, J. Phys. Chem. B. 107 (2003) 11690–11699.

[14] C.B. France, P.G. Schroeder, J.C. Forsythe, B.A. Parkinson, Scanning Tunneling Microscopy Study of the Coverage-Dependent Structures of Pentacene on Au(111), Langmuir. 19 (2003) 1274–1281.

[15] K. Ihm, B. Kim, T.-H. Kang, K.-J. Kim, M.H. Joo, T.H. Kim, et al., Molecular orientation dependence of hole-injection barrier in pentacene thin film on the Au surface in organic thin film transistor, Appl. Phys. Lett. 89 (2006) -.

[16] B. de Boer, A. Hadipour, M.M. Mandoc, T. van Woudenbergh, P.W.M. Blom, Tuning of Metal Work Functions with Self-Assembled Monolayers, Adv. Mater. 17 (2005) 621–625.

[17] K. Asadi, Y. Wu, F. Gholamrezaie, P. Rudolf, P.W.M. Blom, Single-Layer Pentacene Field-Effect Transistors Using Electrodes Modified With Self-assembled Monolayers, Adv. Mater. 21 (2009) 4109–4114.

[18] J. Collet, O. Tharaud, A. Chapoton, D. Vuillaume, Low-voltage, 30 nm channel length, organic transistors with a self-assembled monolayer as gate insulating films, Appl. Phys. Lett. 76 (2000).

[19] M. Mottaghi, P. Lang, F. Rodriguez, A. Rumyantseva, A. Yassar, G. Horowitz, et al., Low-Operating-Voltage Organic Transistors Made of Bifunctional Self-Assembled Monolayers, Adv. Funct. Mater. 17 (2007) 597–604.

[20] E.C.P. Smits, S.G.J. Mathijssen, P.A. van Hal, S. Setayesh, T.C.T. Geuns, K.A.H.A. Mutsaers, et al., Bottom-up organic integrated circuits, Nature. 455 (2008) 956–959.

[21] S.G.J. Mathijssen, E.C.P. Smits, P.A. van Hal, H.J. Wondergem, S.A. Ponomarenko, A. Moser, et al., Monolayer coverage and channel length set the mobility in self-assembled monolayer field-effect transistors, Nat Nano. 4 (2009) 674–680.

[22] X. Guo, M. Myers, S. Xiao, M. Lefenfeld, R. Steiner, G.S. Tulevski, et al., Chemoresponsive monolayer transistors, Proc. Natl. Acad. Sci. . 103 (2006) 11452–11456.

[23] G.S. Tulevski, Q. Miao, M. Fukuto, R. Abram, B. Ocko, R. Pindak, et al., Attaching Organic Semiconductors to Gate Oxides: In Situ Assembly of Monolayer Field Effect Transistors, J. Am. Chem. Soc. 126 (2004) 15048–15050.

[24] A.L. Briseno, T.W. Holcombe, A.I. Boukai, E.C. Garnett, S.W. Shelton, J.J.M. Fréchet, et al., Oligo- and Polythiophene/ZnO Hybrid Nanowire Solar Cells, Nano Lett. 10 (2010) 334–340.

[25] W. Wang, T. Lee, M.A. Reed, Mechanism of electron conduction in self-assembled alkanethiol monolayer devices, Phys. Rev. B. 68 (2003) 35416.

[26] D.J. Wold, C.D. Frisbie, Formation of Metal–Molecule–Metal Tunnel Junctions: Microcontacts to Alkanethiol Monolayers with a Conducting AFM Tip, J. Am. Chem. Soc. 122 (2000) 2970–2971.

[27] R.E. Holmlin, R. Haag, M.L. Chabinyc, R.F. Ismagilov, A.E. Cohen, A. Terfort, et al., Electron Transport through Thin Organic Films in Metal–Insulator–Metal Junctions Based on Self-Assembled Monolayers, J. Am. Chem. Soc. 123 (2001) 5075–5085.

[28] W. Wang, T. Lee, M.A. Reed, Electron tunnelling in self-assembled monolayers, Reports Prog. Phys. 68 (2005) 523.

[29] M.A. Reed, C. Zhou, C.J. Muller, T.P. Burgin, J.M. Tour, Conductance of a Molecular Junction, Sci. . 278 (1997) 252–254.

[30] P. Stoliar, R. Kshirsagar, M. Massi, P. Annibale, C. Albonetti, D.M. de Leeuw, et al., Charge Injection Across Self-Assembly Monolayers in Organic Field-Effect Transistors: Odd–Even Effects, J. Am. Chem. Soc. 129 (2007) 6477–6484.

[31] A. Salomon, D. Cahen, S. Lindsay, J. Tomfohr, V.B. Engelkes, C.D. Frisbie, Comparison of Electronic Transport Measurements on Organic Molecules, Adv. Mater. 15 (2003) 1881–1890.

[32] K. Asadi, I. Katsouras, J. Harkema, F. Gholamrezaie, E.C.P. Smits, F. Biscarini, et al., Organic field-effect transistors as a test-bed for molecular electronics: A combined study with large-area molecular junctions, Org. Electron. 13 (2012) 2502–2507.

[33] W. Wang, T. Lee, M.A. Reed, Elastic and Inelastic Electron Tunneling in Alkane Self-Assembled Monolayers, J. Phys. Chem. B. 108 (2004) 18398–18407.

[34] A. Shehu, S.D. Quiroga, P. D'Angelo, C. Albonetti, F. Borgatti, M. Murgia, et al., Layered Distribution of Charge Carriers in Organic Thin Film Transistors, Phys. Rev. Lett. 104 (2010) 246602.

[35] J. Zaumseil, K.W. Baldwin, J.A. Rogers, Contact resistance in organic transistors that use source and drain electrodes formed by soft contact lamination, J. Appl. Phys. 93 (2003).

[36] K.P. Puntambekar, P. V Pesavento, C.D. Frisbie, Surface potential profiling and contact resistance measurements on operating pentacene thin-film transistors by Kelvin probe force microscopy, Appl. Phys. Lett. 83 (2003).

[37] P. V Pesavento, R.J. Chesterfield, C.R. Newman, C.D. Frisbie, Gated four-probe measurements on pentacene thin-film transistors: Contact resistance as a function of gate voltage and temperature, J. Appl. Phys. 96 (2004).

[38] S. Casalini, A. Shehu, S. Destri, W. Porzio, M.C. Pasini, F. Vignali, et al., Organic field-effect transistors as new paradigm for large-area molecular junctions, Org. Electron. 13 (2012) 789–795.

[39] M.D. Porter, T.B. Bright, D.L. Allara, C.E.D. Chidsey, Spontaneously organized molecular assemblies. 4. Structural characterization of n-alkyl thiol monolayers on gold by optical

ellipsometry, infrared spectroscopy, and electrochemistry, J. Am. Chem. Soc. 109 (1987) 3559–3568.

[40] C. Miller, P. Cuendet, M. Graetzel, Adsorbed .omega.-hydroxy thiol monolayers on gold electrodes: evidence for electron tunneling to redox species in solution, J. Phys. Chem. 95 (1991) 877–886.

[41] Y. Qiu, Y. Hu, G. Dong, L. Wang, J. Xie, Y. Ma, H2O effect on the stability of organic thin-film field-effect transistors, Appl. Phys. Lett. 83 (2003).

[42] S. Hoshino, M. Yoshida, S. Uemura, T. Kodzasa, N. Takada, T. Kamata, et al., Influence of moisture on device characteristics of polythiophene-based field-effect transistors, J. Appl. Phys. 95 (2004).

[43] D. Li, E.-J. Borkent, R. Nortrup, H. Moon, H. Katz, Z. Bao, Humidity effect on electrical performance of organic thin-film transistors, Appl. Phys. Lett. 86 (2005) -.

[44] Z.-T. Zhu, J.T. Mason, R. Dieckmann, G.G. Malliaras, Humidity sensors based on pentacene thin-film transistors, Appl. Phys. Lett. 81 (2002).

[45] G. Horowitz, R. Hajlaoui, D. Fichou, A. El Kassmi, Gate voltage dependent mobility of oligothiophene field-effect transistors, J. Appl. Phys. 85 (1999).

[46] T. Someya, A. Dodabalapur, J. Huang, K.C. See, H.E. Katz, Chemical and Physical Sensing by Organic Field-Effect Transistors and Related Devices, Adv. Mater. 22 (2010) 3799–3811.

[47] C. Bartic, G. Borghs, Organic thin-film transistors as transducers for (bio) analytical applications, Anal. Bioanal. Chem. 384 (2006) 354–365.

[48] J. Krim, J.O. Indekeu, Roughness exponents: A paradox resolved, Phys. Rev. E. 48 (1993) 1576–1578.

[49] S. Casalini, A. Shehu, F. Leonardi, C. Albonetti, F. Borgatti, F. Biscarini, Hydrophilic self-assembly monolayers for pentacene-based thin-film transistors, Org. Electron. 14 (2013) 1891–1897.

[50] H.B. Akkerman, B. de Boer, Electrical conduction through single molecules and self-assembled monolayers, J. Phys. Condens. Matter. 20 (2008) 13001.

[51] H.B. Akkerman, P.W.M. Blom, D.M. de Leeuw, B. de Boer, Towards molecular electronics with large-area molecular junctions, Nature. 441 (2006) 69–72.

[52] I. Kymissis, C.D. Dimitrakopoulos, S. Purushothaman, High-performance bottom electrode organic thin-film transistors, Electron Devices, IEEE Trans. 48 (2001) 1060–1064.

[53] D.J. Gundlach, L.L. Jia, T.N. Jackson, Pentacene TFT with improved linear region characteristics using chemically modified source and drain electrodes, Electron Device Lett. IEEE. 22 (2001) 571–573.

[54] S. Casalini, F. Leonardi, C.A. Bortolotti, A. Operamolla, O.H. Omar, L. Paltrinieri, et al., Mono/bidentate thiol oligoarylene-based self-assembled monolayers (SAMs) for interface engineering, J. Mater. Chem. 22 (2012) 12155–12163.

[55] M.M. Walczak, D.D. Popenoe, R.S. Deinhammer, B.D. Lamp, C. Chung, M.D. Porter, Reductive desorption of alkanethiolate monolayers at gold: a measure of surface coverage, Langmuir. 7 (1991) 2687–2693.

[56] C.A. Widrig, C. Chung, M.D. Porter, The electrochemical desorption of n-alkanethiol monolayers from polycrystalline Au and Ag electrodes, J. Electroanal. Chem. Interfacial Electrochem. 310 (1991) 335–359.

[57] R.K. Shervedani, M. Bagherzadeh, Electrochemical Characterization of In Situ Functionalized Gold Cysteamine Self-Assembled Monolayer with 4-Formylphenylboronic Acid for Detection of Dopamine, Electroanalysis. 20 (2008) 550–557.

[58] R.K. Shervedani, S.A. Mozaffari, Copper(II) Nanosensor Based on a Gold Cysteamine Self-Assembled Monolayer Functionalized with Salicylaldehyde, Anal. Chem. 78 (2006) 4957–4963.

[59] W. Porzio, S. Destri, M. Mascherpa, S. Brückner, Structural aspects of oligothienyl series from X-ray powder diffraction data, Acta Polym. 44 (1993) 266–272.

[60] P. Ostoja, S. Guerri, S. Rossini, M. Servidori, C. Taliani, R. Zamboni, Electrical characteristics of field-effect transistors formed with ordered α-sexithienyl, Synth. Met. 54 (1993) 447–452.

OFET as biosensor

Bioelectronics is one of the latest branches of Organic Electronics. It has received considerable attention in the last years due to the urgent necessity to couple electronic devices with biology. This chapter introduces the basics of bioelectronics and deals with its applications as sensors. A brief description of SAM deployed todevices is given, including our recent results on dopamine sensing. The final part of the chapter illustrates our novel immunosensor for cytokines detection.

4.1 Bio-sensing by means of Self-Assembled Monolayers

Compared to the bulk matter, surfaces differ for many chemico-physical features such as chemical reactivity, work-function, electronic states, morphology and surface tension. Complex structures, such as organic field-effect transistors, are greatly influenced by the different interface reactivities and consequently their electrical performances. Self-assembled monolayers provide a convenient, flexible and a easy-to-use approach for tailoring the interfacial properties of metals, metal oxides and semiconductors.
Over the last decade, SAMs have gained attention for their potential application like anti-corrosion coatings and sensor technology.
First investigations were made on SAMs able to sense pH by noting that SAM capacitance is strongly affected by protonation/deprotonation of the adsorbate itself. Crooks et al. reported pH titrations of mercapto-pyridine and aminothiophenol SAMs. [1]

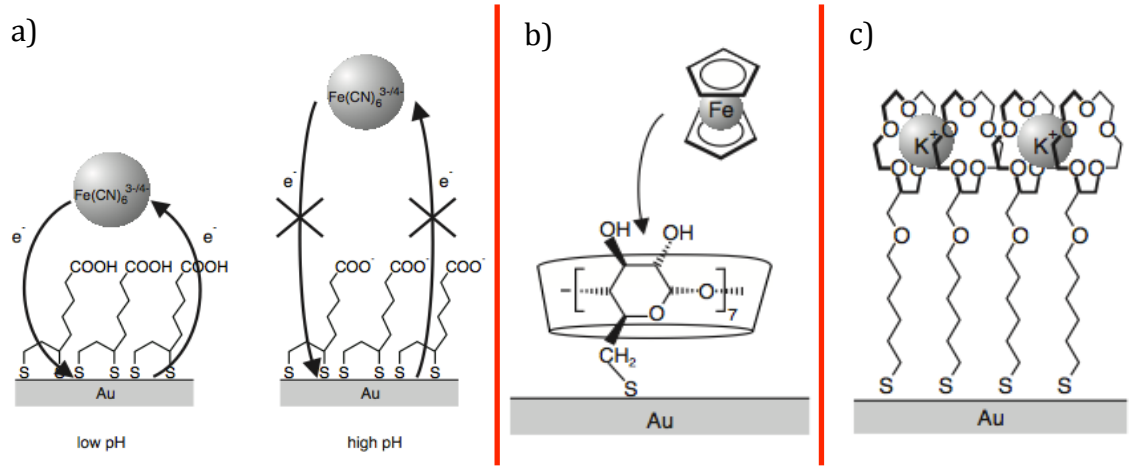

Fig.4. 1 Sensing strategies by means of SAMs a) pH-dependent heterogeneous electron transfer at a de-protonable monolayer, b) SAMs of β-cyclodextrin and their complexation with ferrocene, c) sandwich complexation of metal ions by crown ether adsorbates. [68]

Apart protons, detection of other analytes requires different sensitive mechanism, in which a molecular recognition between SAM molecules and analytes has to occur. Thanks to the extreme versatility of organic chemistry, many SAMs with different functional groups (viz. nonpolar, polar, electroactive and biologically active) are commercial: There are two basic strategies in SAMs engineering: i) the *ex-situ* modification of SAM with functional groups or ligands and the subsequent self-assembly or ii) the modification of the surface due to the direct assembly of a SAM. The latter is more frequent because it requires easier processing, enables the direct integration of ligands in a preformed SAMs. This way of surface engineering makes possible the fusion of particular ligands, which are not compatible with the self-assembling molecules, and it preserves the underlying structure of the SAM. A number of different classes of organic reactions have been explored for SAM modifications, including

nucleophilic substitutions, esterifications, acylations and nucleophilic additions. The external incorporation of functional ligands through amide-bond formation or by means of Schiff's base are two of the most used strategies for SAM tailoring.
Scientific literature presents a wide range of sensors based on the surface engineering; many examples deal with the detection of metal ions like Cd^{2+}, Hg^{2+} and Pb^{2+}, highly toxic environmental contaminants, or with the recognition of small molecules, like glucose. [2–4]
Analyte detection is ensured by the host-guest recognition with SAMs endowed with pluridentate ligands like crown ethers, calixarenes or b-cyclodextrines. [5–7]
When peptides, antibodies or enzymes are directly added on the organic monolayer, a more complex scenario emerges as highlighted in paragraph 4.3.
The fabrication of these '*smart surfaces*' requires not only a careful design of the molecules but also a reliable analytical device. As a result, different transductions have been successfully deployed such as electrochemical, optical, piezoelectric and mechanical ones. Each of them was applied to a wide range of analytes and they showed different pros and cons. My work deals with two types of bio-sensors: the former based on SAMs and the latter on a protein as electrode modifier. These two case studies are part of the field of bioelectronics, whose principal aim is to establish a mutual synergy between electronics and biology.

4.1.2 Organic Bioelectronics

Organic bioelectronics can be seen as the merging of two fields: biology and organic electronics. Main interests are catalysed by this this field, hence the major challenge is to combine electronics to life science and/or health care. Information processing along with storage, electronic components and actuators are other open-issues. [8–10]
The birth of bioelectronics dates back to 18th century thanks to the pioneering work of Luigi Galvani who induced muscular activity in a detached leg muscle of a frog. Nowadays, cells signal stimulation and implantable devices are some of the consequent challenges of this emerging field.
As already mentioned, the implantation of novel devices poses stringent requirements in terms of biocompatibility to avoid auto-immune responses.

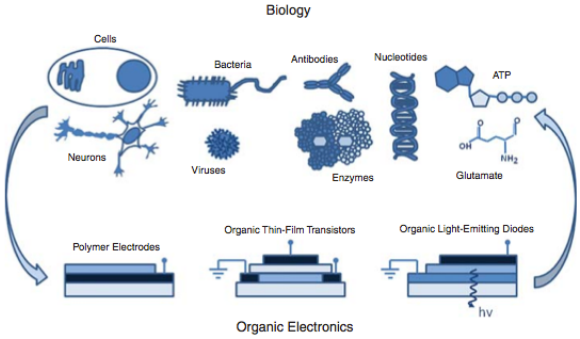

Fig. 4. 2 A cartoon showing the scope of organic bioelectronics. Reprinted with permission from [8]

A further requirement is to provide convenient long-term operation with a minimal loss of electrical functionality throughout the course of implantation; "*real-time*" monitoring could prevent late diagnosis and loco-regional therapies could be performed to improve the quality of life in patients who are subjects of clinical routines.

Furthermore, these kinds of devices have to combine ionic current coupled to electrical signal as many living organisms are used to do.
Nowadays, electronic and electrochemical solid-state transducers operate trough these basic principles by means of architectures based on inorganic and/or organic materials.
As a consequence, organic bioelectronics should design novel devices with active interfaces capable to synchronize communications with living matter and to manage bi-directional exchange of signals.
One of the greatest advantage by using organic materials, compared to the inorganic counterparts, are the mechanical compliance, transparency, easy processing. Moreover they can mimic biological structures such as self-assembly and self-organization.
Field-effect transistors have already demonstrated to be suitable candidate as organic electronics transducer, thus small outer stimuli can induce sizeable changes in its electrical performances. Such kind of sensing includes the detection of gaseous and liquid molecules that have to diffuse in the semiconducting thin-film or adsorb to one of its interface interacting with charge carriers. Some relevant examples were demonstrated by Dodabalapur and Torsi [11], in which an OFET based on NTCDA (1,4,5,8-naphthalene tetracarboxylic dianhydride), as organic semiconductor, was sensitive to specific targets; Andringa et al. [12] demonstrated a SAMFET sensor for nitric oxide in 2010 , whereas Stoliar and co-workers [13] fabricated a pentacene-based OFET sensitive to different concentration of DNA (Fig. 4.3). Further details and examples can be found in literature. [14–20]

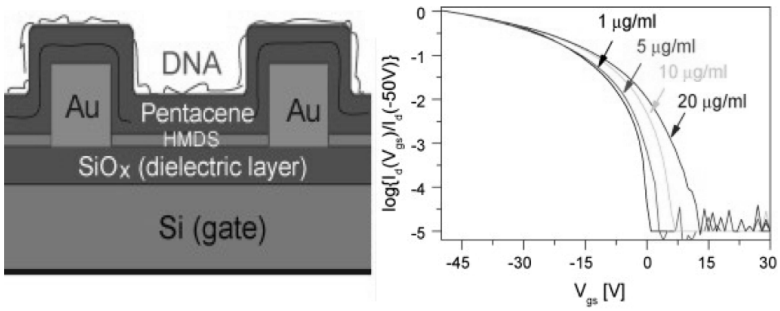

Fig.4. 3 (left) Schematic of the OFET used in [9]. (right) Transfer characteristics at different DNA concentrations. [13]

All these sensors were operated in dry state. The direct exposure of these devices to aqueous solution posed a further requirement: to avoid the water electrolysis and other faradaic reactions.
As already stated, the water electrolysis governed by the following aspects:

$$H_2O \longrightarrow 2H^+ + \tfrac{1}{2}\, O_2 + 2e^-$$

Water is oxidatively turned into protons and oxygen at a standard potential of 0.571 V (vs SHE) and it is inversely reduced

$$2H_2O + 2e^- \longrightarrow H_2 + 2OH^-$$

at a standard potential of -0.658 V (vs SHE) yielding hydrogen and hydroxyls.
These reactions set a limit of the operational potential in OFETs. Usually, organic transistors were operated with higher potentials and the simple exposure to the outer environment induced great instabilities. [21] This scenario posed a further boost in the material synthesis for each single component of the electronic devices. Not only low operational voltages, but

also high-k dielectrics and water-proof organic semiconductors had to be developed in order to avoid encapsulation layers.

The first examples towards this route were the OFET architectures was adopted by Bao and co-workers; they demonstrate the fully operability of these device under aqueous environment by exploiting high-k polymer dielectrics and a water-stable organic semiconductors from 2008 to 2009 [22–24].

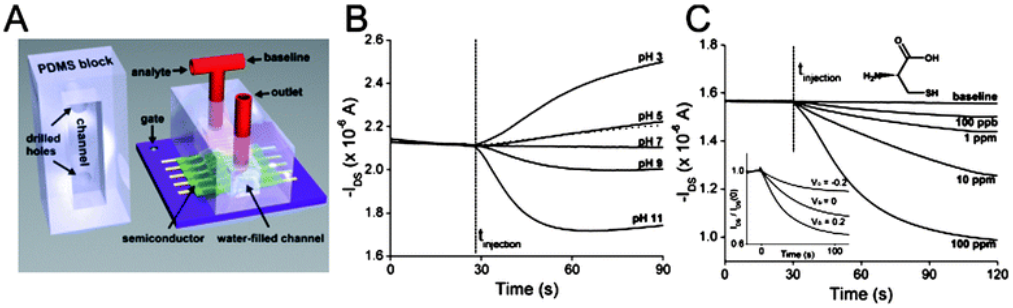

Fig.4. 4 Chemical detection in aqueous systems based on OTFTs (V_{GS} = -1, V_{DS} = -0.6V). A) Schematic showing an OTFT with DDFTTF in flow cell for aqueous phase sensing, B) drain current, IDS, response to pH and C) I_{DS} response to trinitrobenzene (TNB). [23]

The aspecific sensitivity toward small analytes, like cysteine, was validated in the ppm scale (Fig. 4.4). However the recognition mechanism lack of specificity because the response was governed by physical adsorption of these molecules on the OS.

Later on, Kahn and co-workers develop a pentacene OFET biotin sensor using a pentacene as active material with a copper phtalocyanine film (CuPc) as encapsulation layer in 2011. [25]

Specificity was achieved by the introduction of a selective biorecognition system developed in 2012 by Hammock and co-workers, [26] who introduced gold nanoparticles decorated by DNA aptamers onto the organic semiconductor. The high affinity between this kind of aptamer and mercury cations, Hg^{2+}, allows an effective and selective recognition (Fig. 4.5). The same authors developed an analogous system for the *real-time* detection of thrombin down to the nanomolar scale in 2013. [27]

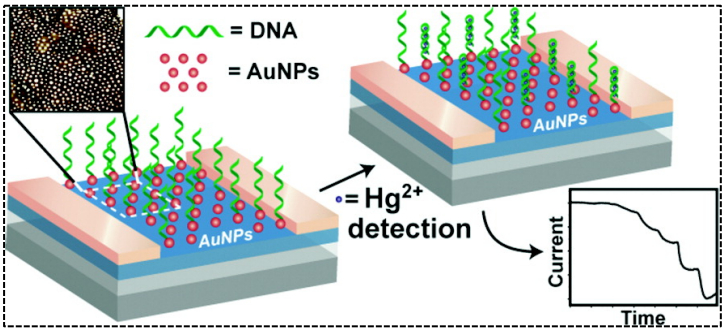

Fig.4. 5 Schematic picture of the sensor showed in [22] for Hg^{2+} detection. [26]

An alternative device configuration with respect to OFET is of the so-called electrolyte-gated organic transistor. This consists of source and drain electrodes and a channel containing the organic active material in direct contact with the gate electrode *via* an electrolyte solution, which acts as the gate dielectric. Two classes of electrolyte-gated devices are known: (i) the Organic Electrochemical Transistors (OECTs) and the Electrolyte-Gated Organic Field Effect Transistors (EGOFETs); the two architectures are shown in Fig. 4.6.

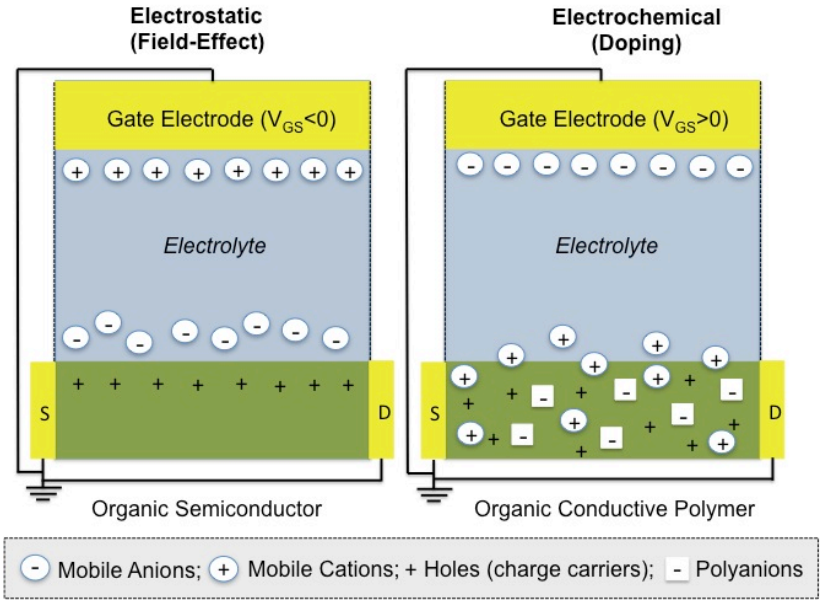

Fig.4. 6 Schematic picture of an EGOFET device (left) and an OECT device (right)

OECT relies on a conductive polymer, which is electrochemically active; thus, ionic diffusion induces (de-)doping of the conductive polymer. Poly(3,4-ethylenedioxythiophene) (PEDOT) or poly(pyrrol) (PPyr) doped by polianion poly(styrenesulfonate) (PSS) are the most used active materials Despite the high transconductance compared to other organic transistors, these devices suffer of low switching speed due to the ion diffusion along with high off-current. Malliaras and co-workers recently overcame this drawback by optimizing the geometrical parameters. [28]

Only in the last decade OECTs have experienced great improvements and they were subject of intense investigations spanning from basic research to advanced application as bio-transducers and bio-sensors.

As a result, Shim et al. [29] reported the first example of OECT as glucose sensor whose working principle resides on the catalytic activity of glucose oxidase. In particular, one by-product of the glucose oxidation is hydrogen peroxide, which is catalytically decomposed by Ptelectrode, which is the OECT gate. This faradaic reaction at the gate electrode induces a more effective Pedot:Pss de-doping, hence a clear lowering of the drain-source current.

Iannotta et al. recently studied the response of OECTs by using surfactants (hexadecyl trimethyl ammonium bromide, CTAB) as electrolyte. The control of the micelle formation offers the unprecedented opportunity to investigate the doping/dedoping mechanism of OECTs by varying their sizes. [30]

Another important example is the use of OECTs coupled to cells and proteins. As shown in Fig.4.7, a cellular barrier has been placed between Pedot:Pss and the gate electrode. Tuning the tissue integrity by using H_2O_2, OECT was successfully used an electrical tool for testing the healthy or pathological state of a cellular tissue. [31] (Fig. 4.7)

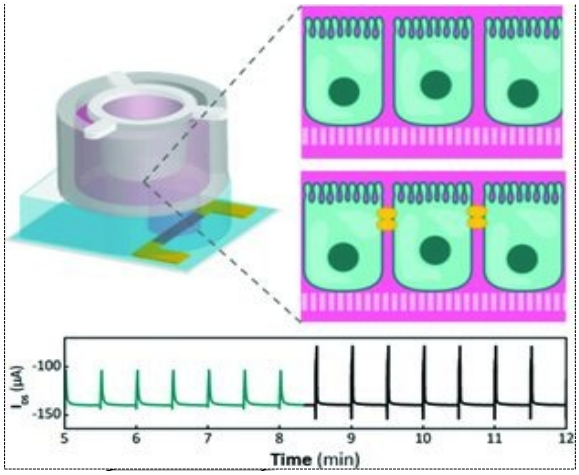

Fig.4. 7 The OECT sensor presented in [27] for assessing barrier tissue integrity of cells.

Extensive reviews on OECTs and their (bio-)applications can be found in literature. [15,18,32,33]

By replacing the conductive polymer with an organic semiconductor (OS), a different working principle arises. Upon the application of gate bias, electrostatic interaction is responsible to charge accumulation at the electrolyte-OS interface due to the presence of an electrical double layer (EDL). Because of EDL thickness (in the order of few nanometers), large capacitive coupling occurs and consequently low operational voltages can be easily exploited.. Many groups evaluate the capacitive coupling at the EDL: Water-gated OFETs were firstly presented by Kergoat at al. in 2010 [35] Impedance spectroscopy was extensively used on semiconducting films, such as P3HT and sexithiophene, in order to quantify the double layer capacitance: 3-6 μF cm^{-2} and 2-8 μF cm^{-2} respectively. [34,35] The double layer capacitance (7.8 ± 0.8 μF cm^{-2}) of pentacene/electrolyte was also extracted by using dual-gated organic field-effect transistor.[36]

Our group extensively adopts this architecture for several purposes, such as bio-sensors and bio-transducers. [37]

4.1.3 Sensing strategy with liquid devices

As already mentioned in previous paragraphs, sensors and/or biosensors should posses an efficient transduction unit capable of signal amplification along with a stable operation. However, one of the main prerogatives lies in the sensitive element, which represents the recognition core towards the analyte of interest.

All the type of OFETs are interfacial devices, thus the interface engineering plays a key in role for (bio-)sensing applications.

Kergoat et al. (2011) and Buth et al. (2013) developed two EGOFETs for DNA and penicillin detection, respectively. As reported in Fig. 4.8a they share the same sensing strategy, namely the chemical modification of the OS surface. The additional charges induced by the analytes grafting in proximity to the conducting channel give rise to a change in the charge carrier density, thus the consequent behaviour turned out to be analyte-dependent. [34,38]

Usually, the OS modification often worsens the electrical behaviour lowering the hydrophobic barrier; Torsi et al overcame these drawbacks by means of direct physisorption of a phospholipid film on OS surface as shown in Fig. 4.8 b).
They shows the stabilizing effect of this natural coating in EGOFETs. [39]
Pedot:Pss and other conductive polymers are electrochemically stable thus OECT configuration opens towards the use of redox active analyte. Tang and co-workers (2011) developed an OECT sensor for the neurotransmitter dopamine. The sensing mechanism (Fig. 4.8 c)) took advantage of the dopamine oxidation to *o*-dopaminequinone at the surface of the gate electrode. The V_{GS} shift is the responsible of the sensing behaviour. [40]
Moving to our approach, the sensing strategy is focused on the modification of the top Au electrode by Self-Assembled Monolayers (SAMs). This means that the sensing core and the transducing unit are decoupled (Fig. 4.8 d)). The binding event at the gate/electrolyte interface gives rise to a resistance drop coupled with the addition of surface dipoles. These changes are consequently mirrored to the transducer unit.

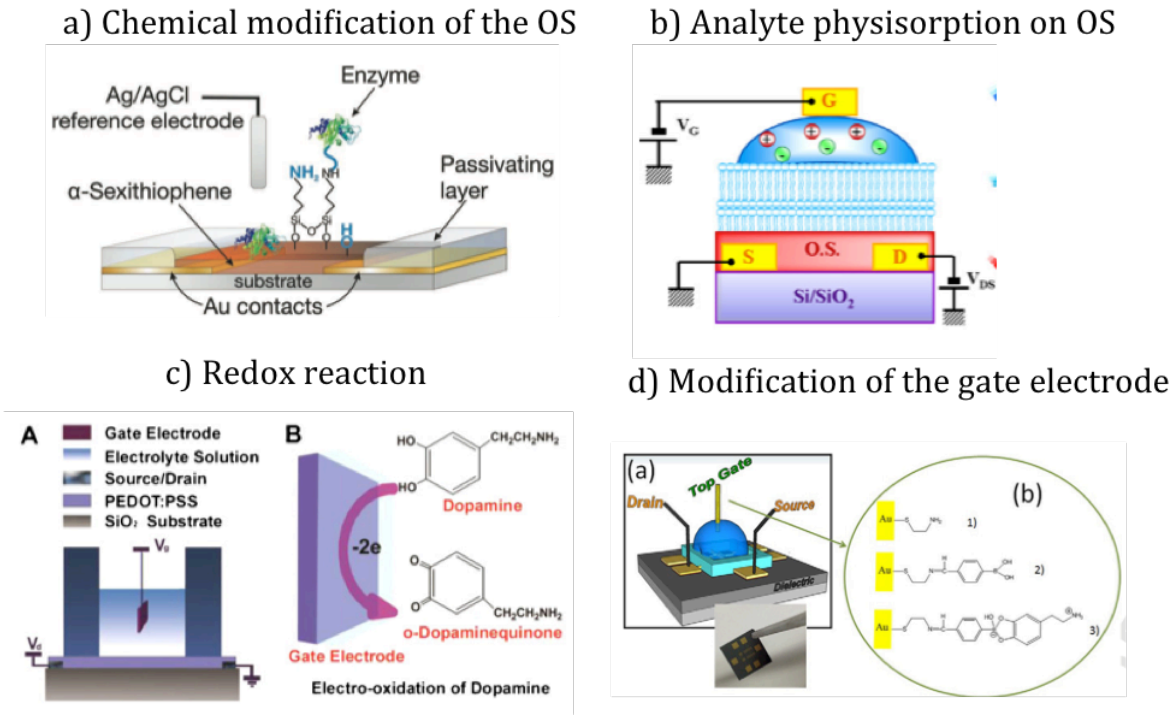

Fig.4. 8 Sensing strategy with OTFT liquid devices: a) chemical modification of the OS, [34] b) physisorption of the analytes on OS, [39] c) redox reaction in liquid electrolyte [40] and d) functionalization oft he top gate electrode.

4.2 Label-free detection of dopamine by means of EGOFET

4.2.1 Dopamine in disease

My work has been focused on dopamine (or 3,4-dihydroxyphenethylamine) that is a neurotransmitter within the catecholamine family. It plays an important role in mammalian brain by regulating the reward-motivated behaviour, motor control and the release of several important hormones.

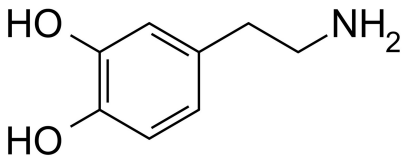

Fig.4. 9 Chemical structure of dopamine.

Outside the nervous system, dopamine acts as a local chemical messenger in several parts of the body. For instance, it inhibits norepinephrine release in the blood vessels; it increases sodium excretion and urine output in the kidneys; it reduces insulin production in the pancreas; it reduces gastrointestinal motility and protects intestinal mucosa in the digestive system; and it reduces the activity of lymphocytes in the immune system. With the exception of the blood vessels, dopamine has a "paracrine" function in each of these peripheral systems, that means its local synthesis and exploitation..

Tyrosine is the natural precursor of dopamine, as shown in fig.4.10. Blood-borne tyrosine is taken up into the brain by a low-affinity amino acid transport system and subsequently from brain extracellular fluid into dopaminergic neurons by high- and low-affinity amino acid transporters. Once tyrosine is inside the neuron, its conversion to dihydroxyphenylalanine (L-DOPA), catalysied by the cytosolicenzyme tyrosine hydroxylase, is normally the rate-limiting step in dopamine biosynthesis (see fig.4.10).

Aromatic amino acid decarboxylase (AADC, dopadecarboxylase) is the enzyme responsible for the cytosolic conversion of L-DOPA to dopamine. This enzyme decarboxylates L-DOPA that the levels of this amino acid in brain are very low under normal conditions. [41]

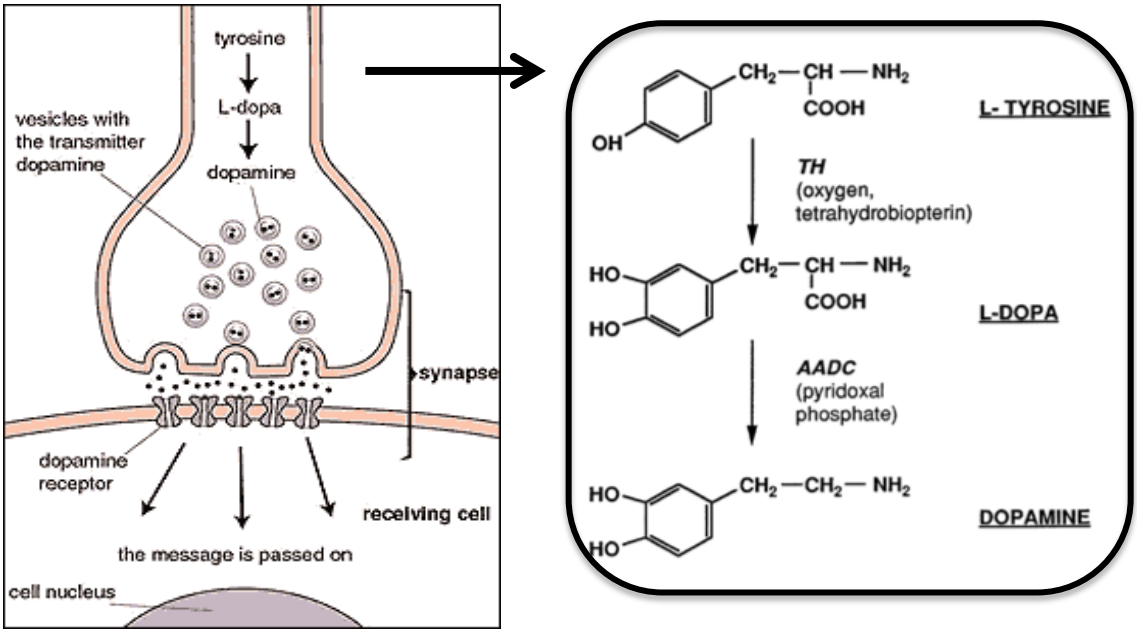

Fig.4. 10 A dopamine synapse (left), the upper part of the figure represent in the pre-synaptic area where dopamine biosynthesis takes place.

Concerning to the therapeutics, in the late 1950s Carlsson showed that L-DOPA was able to cross the blood–brain barrier, restoring brain dopamine levels and motor function in animals. He proposed a role for dopamine in the control of motor function and suggested that dopamine deficiency might give rise to Parkinsonism. [42] In 1960, Ehringer and Hornykiewicz found out that the levels of dopamine are severely reduced in the striatum of patients with Parkinson's disease (PD); symptoms become manifest when about 50% of dopamine-containing neurons in the substantia nigra and 70–80% of striatal dopamine are lost. [43]

PD is the most common neurodegenerative movement disorder. It affects more than 0.1% of the population older than 40 years of age. [44] Clinically, many patients suffer from slowness of movements, rest tremor, rigidity, and disturbances in balance (Fig. 4.11). A number of patients also suffer from anxiety, depression, autonomic disturbances, and dementia. Although there are effective symptomatic therapies, there are no proven neuroprotective or neurorestorative therapies. [44]

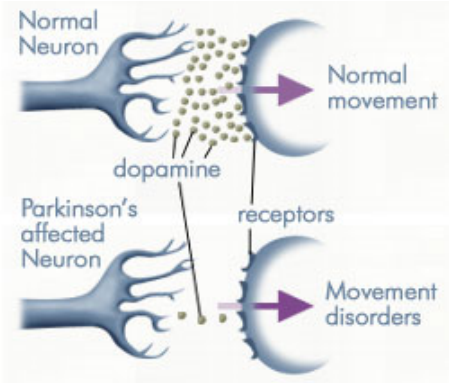

Fig.4. 11 Dopamine levels in a normal and a Parkinson's affected neuron.

Several aetiological triggers have been linked to Parkinson's disease, including genetic mutations and environmental toxins, but the pathway that leads to cell death is still unknown.

Recent developments have shed light on the pathogenic mechanisms that underlie the degeneration of these cells. Dopamine, synthesized in the cytoplasm, is captured and concentrated inside the synaptic vesicles. These vesicles are designed to protect the molecule from degradation by monoamine oxidase and are indispensable for the process of release of neurotransmitter into the synaptic cleft by nerve impulse. The vesicles, due to the wave of depolarization, merging their membrane with the neuron, open releasing their contents into the synaptic cleft. [45]

Recent studies propose that defective sequestration of dopamine into vesicles, leading to the generation of reactive oxygen species in the cytoplasm (Fig. 4.12), is a key event in the demise of dopaminergic neurons in Parkinson's disease, and might represent a common pathway that underlies both genetic and sporadic forms of the disorder. [46][47]

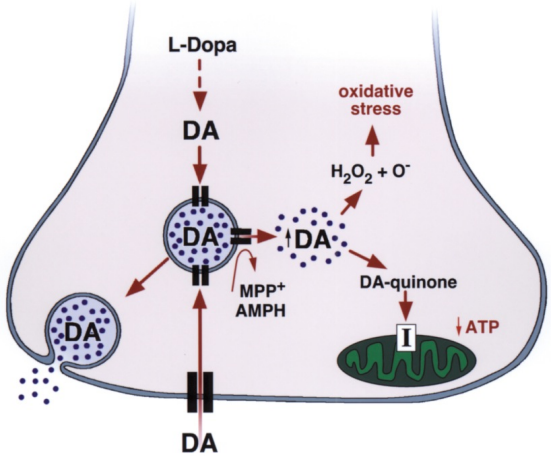

Fig.4. 12 Schematic view of a dopaminergic nigrostriatal terminal depicting the pathways for dopamine (DA) synthesis and metabolism under normal conditions and in the presence of specific neurotoxins. Dopamine is synthesized in the cytoplasm and immediately sequestered into monoaminergic vescicles. If unstored dopamine can auto-oxidized to yield hydrogen peroxide (H_2O_2) superoxide radical ($O^{\cdot -}$) and dopamine-quinone, a cytotoxic dopamine by-product.

The L-DOPA therapy of PD has been one of neuro-pharmacologic breakthroughs because this drug can restore the brain dopamine level crossing the protective blood–brain barrier, whereas dopamine cannot.

Despite its great practical importance, the L-DOPA therapy has a large number of troublesome side effects related to long-term use of this drug.

Concerning PD diagnosis, this is still problematic, mainly at the early stages. Structural and functional imaging, like single photon emission computerized tomography (SPECT), can provided important insights into the structural, pathophysiological and pharmacological changes associated with PD but these techniques usually support PD diagnosis only in patients with advanced-stage disease.

A clinical and analytical method to diagnose PD does not exist. The ability to monitor the concentration change of dopamine could also improve the design of therapeutics and evaluation of their therapeutic efficacy towards PD. One of the open-challenge regarding to the dopamine detection is the low concentration in the extracelluar fluid of the nucleus (0.01–1 μM for a healthy individual and in the nanomolar (nM) range for patients with Parkinson's disease), while the concentrations of the main detection interferents, e.g., ascorbic acid (AA), are usually several orders of magnitude higher (ascorbic acid levels are generally within 0.1–0.6 mM). [48] Different methods have been described for dopamine determination including chromatography, spectrophotometry [49] and electrochemistry [50] and several modified sensors are also reported.

In the following paragraphs, a novel type of sensor for dopamine based on an electrolyte-gated organic field effect transistor (EGOFET) is presented.

4.2.2 EGOFET architecture for dopamine sensing

Our device architecture is depicted in Fig. 4.13. It consists by our standard test pattern cleaned with a standardized protocol (see Chapter 2.2.1) and coated by P3HT thin-film

deposited by spin-coating (see Chapter 2.1.5). The aqueous environment (PBS 50mM, pH = 8.5) is confined onto the four transistors with a polydimethylsiloxane (PDMS) pool.

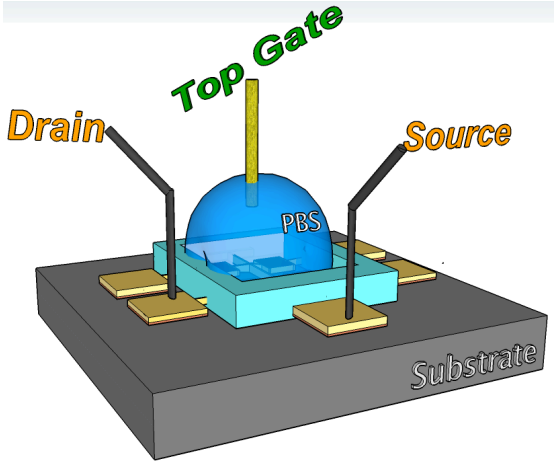

Fig.4.13 Schematic picture of our test pattern integrated with a poly(dimetylsiloxane) pool for confining a droplet of phosphate buffer solution (PBS).

Instead of using the incorporated silicon bottom gate, maintained floating during electrical measurements, we exploit a top Au electrode, which modulates the electrochemical potential of the aqueous solution. The sensing core of our device is a self-assembled monolayer of cysteamine (CA) and 4-formylphenyl boronic acid (BA) on the Au electrode which enables the covalent binding of dopamine (DA) due to the esterification between BA and DA, as shown in Fig. 4.14.

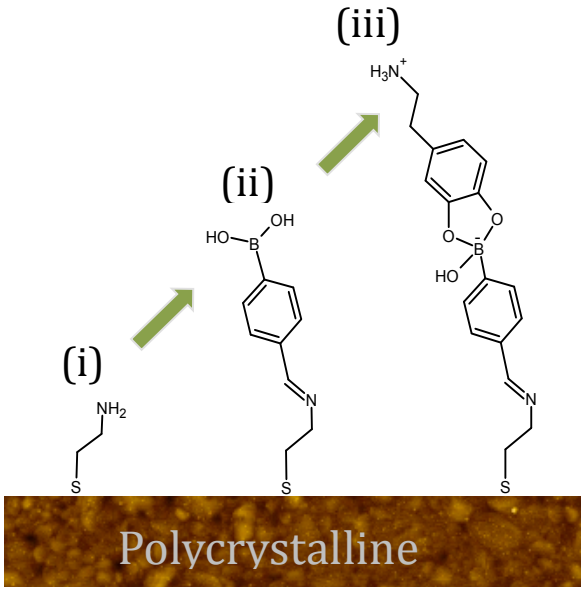

Fig.4. 14 Functionalization protocol for dopamine detection: i) cysteamine (CA), ii) boronic acid (BA) and iii) dopamine (DA) recognition.

The functionalization protocol was the same described by Shervedani et al. [51] except for the CA concentration of 1 mM. The DA adsorption was performed by dipping the Au wires coated with CA–BA-based SAM for 30 min in different DA solutions of 1pM, 1nM, 1μM and 1mM buffered at pH 8.5 with PBS.

In the adsorption process, a large surface dipole builds up due to the zwitterionic structure of

the boronic acid and the amine group. The resulting changes of the transconductance of the EGOFET allow the detection of DA.

4.2.3 Electrical characterization

As benchmark, we use the EGOFET with the gate electrode functionalized by CA–BA SAM. Fig. 4.15 shows the transfer and output characteristics of the reference EGOFET as obtained by sweeping the gate voltage in 50mM PBS.

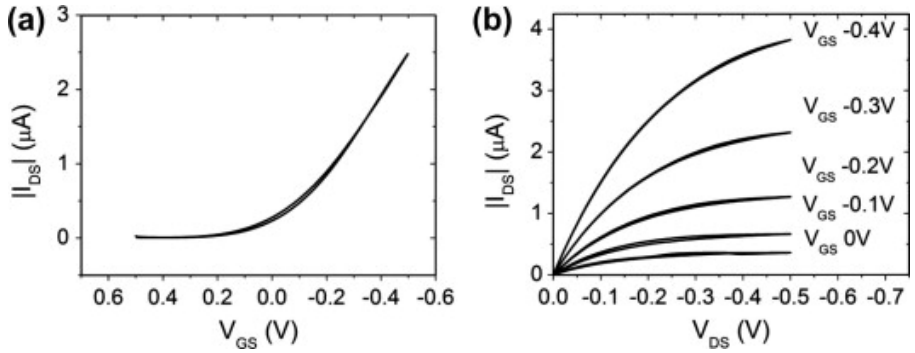

Fig.4. 15 Transfer (a) and output (b) characteristic oft he reference device, in which the gate is functionalized by CA-BA based SAM. Transfer are aquired in linear regime with V_{DS} = -0.1V.

The leakage current always remains below 5nA during operation and no hysteresis appears that indicates no electrochemical doping. In order to investigate the sensitivity of the EGOFET, we immersed the Au electrode for 30min in different DA solutions whose concentration ranges from pM to mM

Results are shown in Fig. 4.16a. At pM concentration, a clear decrease of the current in the transfer characteristics is observed. Increasing DA concentration, the transfer curves decrease down to one order of magnitude (1mM of DA) with respect to the initial value..

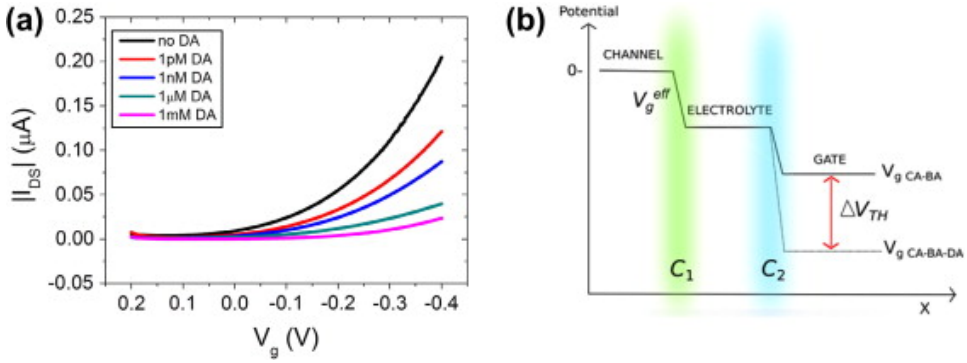

Fig.4. 16 (a) Transfer characteristic are acquired in linear regime (V_{DS} = -0.1V) for each DA concentration. (b) Potential profile along the spatial coordinate x showing the two capacitive drops related to organic semiconductor/electrolyte and gate/electrolyte interfaces respectively.

As shown in Fig. 4.16(b), the rationale illustrates the electrostatic coupling between gate electrode and the p-type semiconducting channel while operating in the accumulation regime. The potential difference, denoted as $V_{G,eff}$,occurs at the organic semiconductor/aqueous solution interface and governs the charge accumulation in the channel and the related drain current. In the case of polarizable gate electrode (no faradaic current), a second potential drop occurs at the electrolyte/gate interface, which leads to a difference between effective

and applied V_G gate potentials. In addition, a surface dipole potential $\Delta\phi_D$ can build up at the interface due to the adsorption of polar molecules, thus inducing a further shift of the gate potential. This can be expressed as:

$$V_{G,eff} = \frac{C_2}{C_1+C_2}(V_G + \Delta\phi_D) \qquad \text{Eq 4.1}$$

where C_1 and C_2 denote the *in-series* capacitances (see Appendix D for the mathematical derivation) of the aqueous solution/organic semiconductor and aqueous solution/gate interfaces, respectively. According to the transfer characteristics, a more negative gate voltage has to be applied to obtain the same amount of current (I_{DS}) after additional DA exposures (see Fig. 416(a) for comparison). DA adsorption changes both the capacitance ($C_{2,DA}$) and the dipole potential ($\Delta\phi_{D,DA}$). Using Eq. 4.1, we perform a quantitative analysis of the sensing experiments and we assess how DA adsorption affects the potential drop at the electrolyte/gate interface. By rescaling the applied gate potential to its effective value all transfer curves can be collapsed into the universal transfer curve (shown in Fig. 416(a)), which is described by the following relation:

$$I_{DS}(V_{G,eff}) = I_{DS}[s_c(V_G + \Delta V_{th})] \qquad \text{Eq. 4.2}$$

where the scaling factor: $s_c = \frac{C_{2,DA}(C_1+C_{2,ref})}{C_{2,ref}(C_1+C_{2,DA})}$

and the threshold shift is: $\Delta V_{th} = \Delta\phi_{D,DA} - \frac{\Delta\phi_{D,ref}}{s_c}$ (see Appendix C for the derivation).

$C_{2,ref}$ and $\Delta\phi_{D,ref}$ are the capacitance and interface dipole potential of the reference device relative to the electrolyte/gate electrode interface.

Fig. 4.17(a) shows the perfect overlap of the different transfer characteristics after least squares minimization of the parameters s_C and ΔV_{th}.

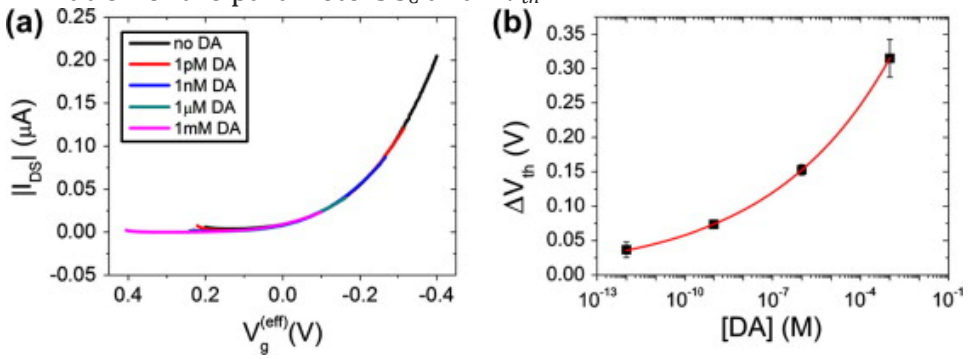

Fig.4. 17 (a) Universal transfer characteristic upon rescaling parameters. (b) ΔV_{th} vs. DA concentration has been reported.

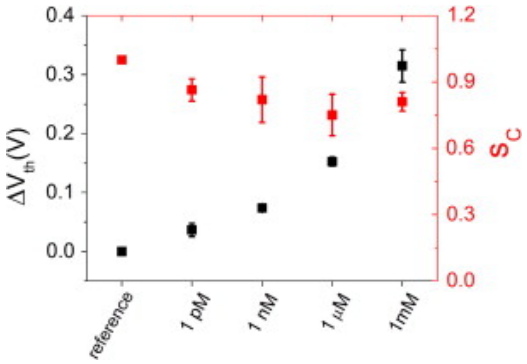

Fig.4. 18 ΔV_{th} (black squares) and sc (red squares) are reported as a function of dopamine concentration.

s_c and ΔV_{th} dependence on DA concentration is shown in Fig. 4.18.

The scaling factor s_c decreases slightly with increasing DA adsorption, indicating a small reduction in capacitance.
A stronger dependence on concentration is observed for the threshold voltage, which shifts up to 350mV. The direction and magnitude of this modulation are in agreement with the zwitterionic structure of the boronic acid together with the terminal amine (see Fig. 4.14). We note however, that screening effects [38] and structural order along the thickness of the SAM [52][53] are expected to strongly influence the dipole potential and to render its dependence on concentration rather complex. The observed non-linear behavior of ΔV_{th} is probably correlated to structural order of the monolayer itself that affects the interfacial dipole at the gate electrode. The ΔV_{th} trend can be fitted by the following power law, $\Delta V_{th} = a * [DA]^{(b)}$, showing a, b and r parameters equal to 0.651 ± 0.001, 0.1045 ± 0.0004 and 0.99994 respectively. The fit (see Fig. 4.17b) points out how the electrical response is more effective for low DA concentrations compared to higher ones. As a consequence, we can state that our EGOFET is well-suited for monitoring healthy or pathological DA concentration. It is worth noting that a similar approach has been achieved for DNA directly adsorbed on the gate surface of an OECT yielding lower ΔV_{th} (around 10–50 mV). [52]

4.2.4 Wettability analysis and Electrochemical characterization

The "*in-situ*" preparation of a multi-step SAM changes progressively the chemical–physical properties of the polycrystalline Au. The study of surface wettability by means of contact angle measurements describes the adhesion work (W_A) profile, which shows a general decrease moving from the bare Au up to the Au–CA–BA–DA (see Fig. 4.19).

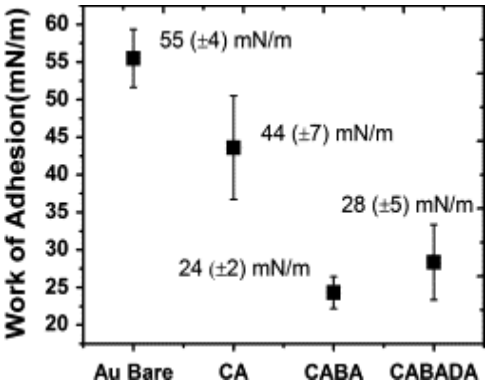

Fig.4. 19 Adhesion work for each step of ML-SAM formation.

Electrochemistry is a powerful tool for assessing monolayers integrity and could monitor the formation of our SAM step-by-step. Two kind of electrochemical experiments have been performed: i) the cyclic voltammetric response of $[Fe(CN)_6]^{3-/4-}$ in order to monitor the blocking properties of the SAM towards electron transfer and ii) the capacitive measurements using phosphate buffer solution (PBS) as support electrolyte.

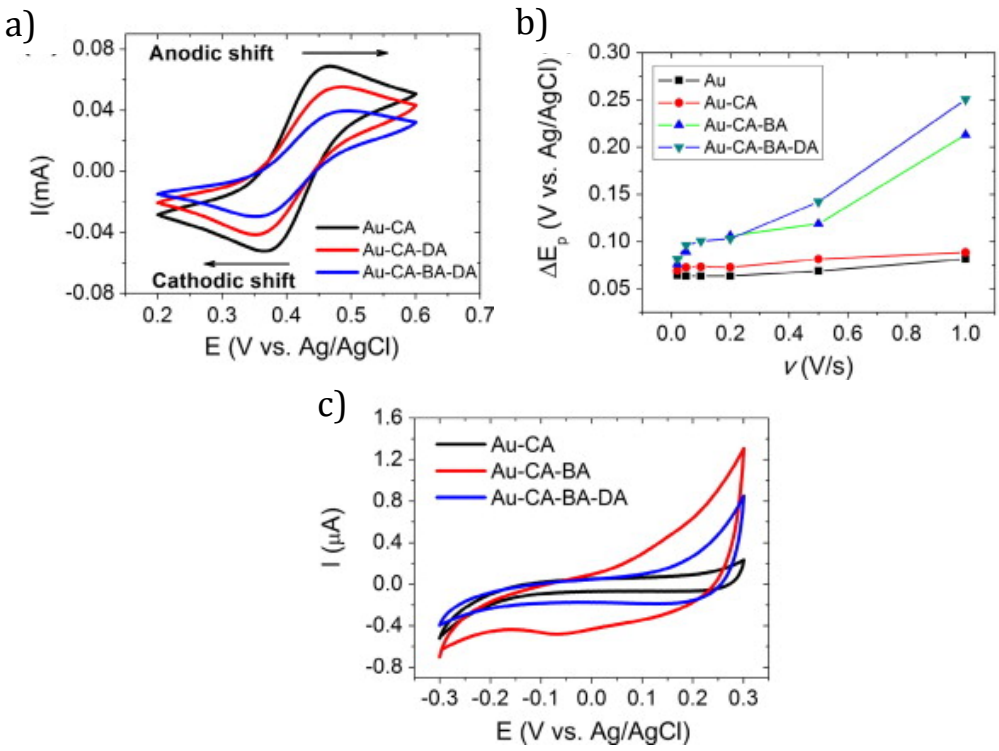

Fig.4. 20 a) Overlay of the three steps for ML-SAM formation at the same ν (200 mV/s). b) ΔE_p vs ν plot for each step of ML-SAM formation and c) capacitive current at the same ν.

The progressive increase of the SAM thickness induces a consequent distortion of the voltammetric response (see Fig. 4.20a) and we observed an increased ΔE_p at the same ν (Fig. 4.20b) after each step. This faradaic study shows a partial distortion of the electrochemical signal of $[Fe(CN)_6]^{3-/4-}$ pointing out a non-complete coverage and a highly disordered SAM. This experimental evidence is further supported by impedance spectroscopy in faradaic regime (see Fig. 4.21). From the fit related to the Nyquist plot [54], the charge transfer resistance undergoes a dramatic increase for each step of the SAM functionalization (equal to 26.2 Ω, 664 Ω and 2.86 kΩ for CA, CA–BA and CA–BA–DA respectively). The capacitive study enables us to assess the capacitance of the double-layer at the gate functionalized by the ML-SAM [55] (see Fig. 4.20c). The linear dependence between the charging current and the scan rate yields capacitance values equal to 1.47(±0.05) μF/cm², 2.42(±0.07) μF/cm² and 2.06(±0.07) μF/cm² for Au–CA, Au–CA–BA and Au–CA–BA–DA respectively. The capacitive drop due to the DA adsorption is equal to 0.36 μF/cm² proving the surface gate switch from soft acidic (BA) to basic (DA) property along with an increase of the SAM thickness.

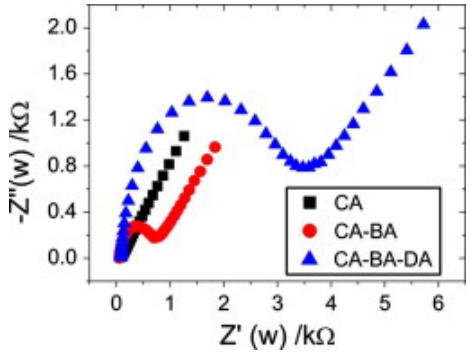

Fig.4. 21 Impedance response obtained for faradic measurements in 100mM PBS at pH 8.5, 5 mM $[Fe(CN)_6]^{3-/4-}$ and 2 M KCl for each step of functionalization.

4.3 Immunosensing by means of Electrolyte-Gated Organic Field-Effect Transistors

4.3.1 Introduction

Accordingly to IUPAC gold book, a biosensor is a device that use specific biochemical reaction mediated by isolated enzymes, immunosystems, tissues, organelles or whore cells to detect chemical compounds usually by electrical, thermal or optical signal. [56]
The canary in a cage that was used by miners to detect gas leakage can be considered the first example of biosensor. Today, the most common commercial biosensors are (i)the blood glucose biosensor that exploits the enzyme glucose oxidase and (ii) the pregnancy test, which is a colorimetric biosensor based on an antibody-based detection..

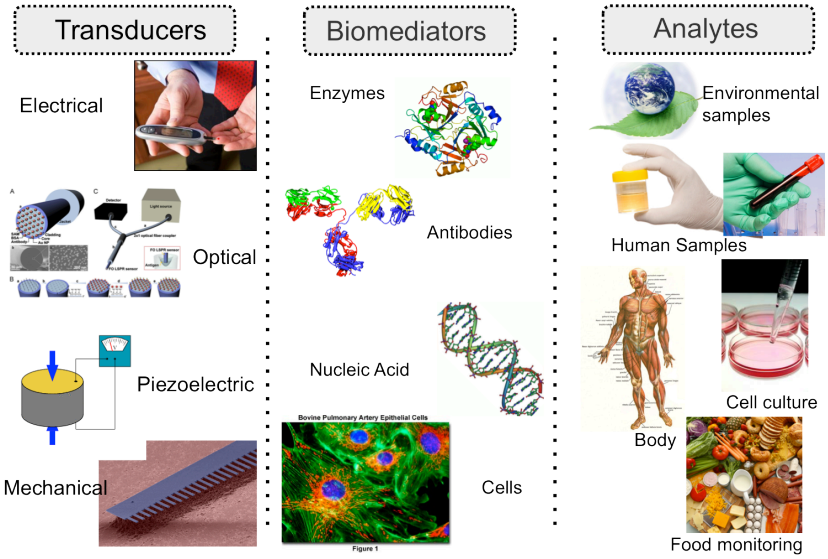

Fig.4. 22 Biosensors components: the transducing unit, the biorecognition element and the analyte.

As depicted in Fig.4.22, a biosensor is composed by two elements: a biological recognition unit and a transducer. The former is capable to interact specifically with a target, whereas the latter is able to turn a biological event into a recordable signal.
The most appealing applications for biosensors are deployed in healthcare, industrial processes and biodefense. New applications are also being discovered since they can be miniaturized, or modified in order to be more user-friendly. The biosensors market is extremely wide, in fact it entails diabetes monitoring, cardiac monitoring, drug discovery, agriculture, environmental and bio-defence practices.

4.3.2 Protein engineering for direct immobilization

Despite the promising symbiosis between material technology, biochemistry, and biotechnology, it is not trivial to implement biosensor concepts in routine diagnostics.
The first aim is to detect target (bio-)molecules in relevant concentrations and in complex media such as bodily fluids (e.g., blood, plasma, urine, ...) and in food/environmental matrices (e.g. water, soil, air, ...). [57–61]
For this reason, it is crucial to assemble the detection element, like protein, antibodies (Abs)

or enzymes, avoiding loss of functionality.
One of the related issues is the (bio-)receptor orientation; a second complication derives by yielding homogenous coverage that can guarantee high reproducibility of the biosensor performances (Fig. 4.23).

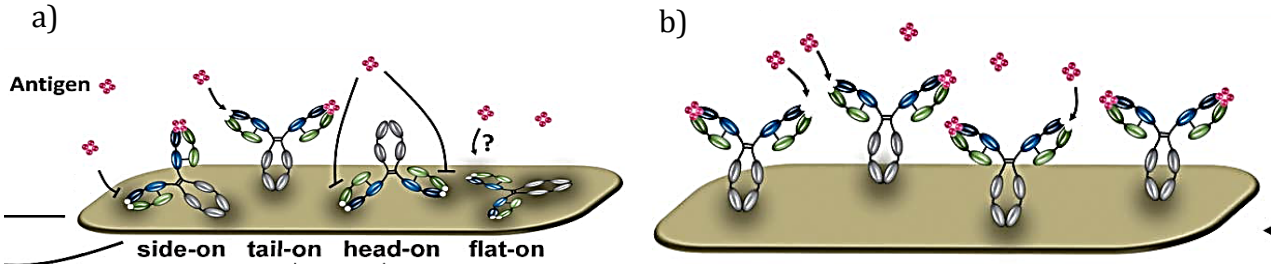

Fig.4. 23 Schematic view of a random immobilized Abs and an oriented immobilized Abs. [69]

In addition to the protein orientation and homogeneity of the surface, the stability of the coupling of the receptor to the supporting surface may play a crucial role. As a consequence, the chemistry used for the immobilization therefore has a pivotal role.
The most simple and inexpensive method for biomolecule immobilization is by physical adsorption. With this method, proteins are immobilized via weak interactions between the protein and the surface (i.e., hydrogen bonds, electrostatic interactions, hydrophobic interactions, and van der Waals interactions). [62]
Although physical adsorption offers some advantages (simplicity and possible reusability of the substrate), it however generally leads to a non-homogeneously surface coated with proteins in a disordered orientation.

Reactive group		Amino acid
	Primary amine	N-terminus ε-amino group of Lysine
	Carboxylic acid	C-terminus Glutamic acid Aspartic acid
	Thiol	Cysteine
	Hydroxyl	Serine Threonine
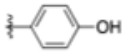	Phenol	Tyrosine
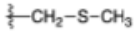	Thioether	Methionine
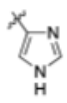	Imidazole	Histidine
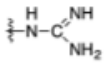	Guanidino	Arginine

Fig.4. 24 Reactive functional groups in naturally occurred amino acids.

A more robust way to create (bio-)functionalized surfaces is to immobilize the proteins at SAM-coated surface by means of covalent bonds (Fig. 4.24). Amine and carboxylic groups are chemical functionalities present on several amino acids and their activation is widely used in coupling chemistry. The most common activation strategies are the amine activation *via* N-Hydroxysuccinimide (NHS) or glutaraldehyde, whereas the carboxylic acid can be activated by EDC/NHS or Sulfo-EDC/NHS. However, these procedures have some limitations. Firstly, these functional groups are pH-dependent, hence each (bio-)molecules have own experimental conditions to be set. The second drawback is the high abundance of amine and carboxylic acids on protein surface that do not allow the control the final orientation of the immobilized (bio-)molecule.
Cysteine-mediated grafting is a more controlled approach, because this aminoacid is less abundant with respect to the other ones.
To further increase the orientation of the immobilized protein of interest, it is possible to make use of tagged proteins, such as protein G and protein A, which can be specifically grafted. Tags are small peptide sequences genetically fused on the N- or C-termini of a recombinant protein. Usually, tags find many usages, such as affinity chromatography and optical assays.
For instance, His-Tag is chemical affine to metal substrates like Ni, Cu, Co, Au etc. Biotin is another well-known tag used for tight recognition towards proteins that bear its counterpart (viz. streptavidin).
These approaches are based on high selective interactions and ensure the control over protein orientation. [63]

4.3.3 Cytokines and immune system

Cytokines are signalling proteins (5-20 kDa) secreted by the cells of innate and adaptive immunity that mediate many of the functions of these cells. Their range of actions is rather wide, including the abilities to induce growth, differentiation, cytolitic activity, apoptosis and chemotaxis.
Their family includes chemokines, interferons, interleukins, lymphokines and tumor necrosis factor. The large family of cytokines is usually classified according to their functional role in the immune system thus, Type I cytokines (INf-γ, TNFα, IL-6, ecc…) enhance the cellular immune response, otherwise Type II (TGF-β, IL-4, IL-10, IL-13, ecc…) stimulate the antibody response.
An interesting aspect of their function is the regulation that the two classes of proteins mutually exert by inhibiting or enhancing the two responses. A subject of intensive study is the unbalance of this mutual response that seems to have a key role in the pathogenesis of several auto-immune disorders.
Among the purposes of bioelectronics, one is the fabrication of implantable devices for loco-regional therapies or *real-time* sensing. Once implantation is carried out, it is usually observed an acute inflammation that in some case compromises the implant itself and the clinical status of patients. Implantable Organic Nano-Electronics (I-ONE) is an European project that

proposes a novel flexible organic electronic device for the treatment of the spinal cord injury (SCI). [64]

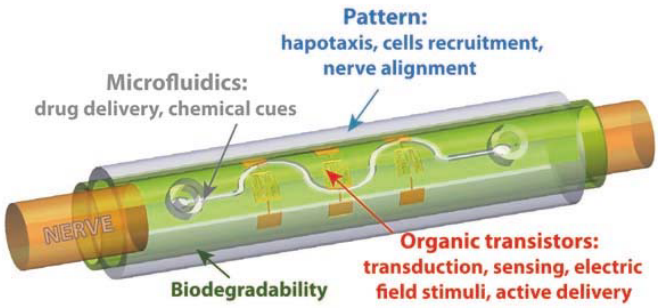

Fig.4. 25 Schematic picture of AMID device.

The implants (Active Multifunctional Implantable Device, AMID, Fig. 4.25) will promote nerve regeneration by a combination of local stimuli. In order to control the immune-inflammatory response, this device must be endowed with a biosensor capable to sense some inflammatory biomarkers such as interleukin-6 and interleukin-4.
Interleukin 6 (IL6) is a glicoprotein arranged in 4 alpha chains that play a role in both innate and adaptive immunity. It acts in a wide variety of biological functions by exerting both a pro-inflammatory and anti-inflammatory roles. [65][66] As pro-inflammatory cytokine, one of its major role is triggered during the acute phase response , because IL-6 induces an intracellular signalling cascade giving rise to inflammation. [67] It is well documented that during trauma, infection or burns, IL6 production increases at the inflammation site from picomolar to nanomolar concentration.
Interleukin 4 (IL4) is 129 amino acids protein arranged in four alpha chains that has a role as anti-inflammatory mediator of immune-response, including the stimulation of the activated B-cells and T-cells proliferation. The two interleukins structures are depicted in Fig. 4.26.

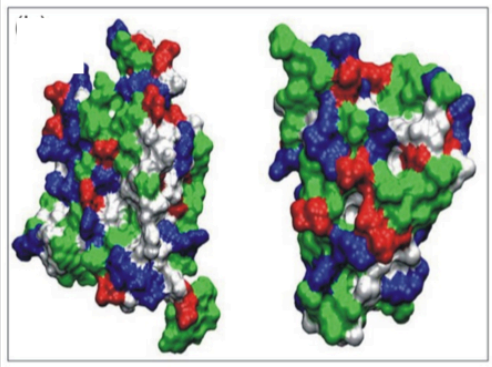

Interleukin-6	Interleukin-4
pro-inflammatory	anti-inflammatory
MW_{IL-6} = 21.7kDa	MW_{IL-4} = 13.5kDa
187 a.a.	120 a.a.
P.I. 6.7	P.I. 8.2

Fig.4. 26 Cytokine targets used in this experiment.

As a result, IL6 and IL4 have been judged to be pro- and anti-inflammatory biomarkers for a biosensor that could be worth to monitor in order to monitor the possible immune-response.
Within this context, we have fabricated and tested a novel EGOFET biosensor for the detection of IL6 and IL4.

4.3.4 EGOFET architecture for interleukins detection

The sensing strategy is similar to the above-described sensor for dopamine. This means that the sensing core is placed on the top gate electrode (Fig. 4.27). The transducer unit has been unconventionally fabricated, as described in Chapter 2.1.2.
To ensure selectivity, we exploited the host-guest recognition of a biological couple antibody (Ab)-antigen (Ag). In particular, monoclonal Anti-IL6 and the monoclonal Anti-IL4 have been immobilized on Au gate.
Antibodies immobilization was performed comparing two different electrode modifiers: (i) the 6-aminohexanethiol (HSC_6NH_2) activated by glutaraldehyde (strategy I) and (ii) the recombinant protein G (PG) (strategy II). The former guarantees a chemical binding between the coated metal and the Ab lysines. This functional approach is well-known and widely used, however it does not control the Ab orientation. The latter approach takes advantage of the recombinant PG, whose N-terminus side is tailored by a 6-His-Tag and it lacks of the albumin binding domain along with cell membrane domain. The presence of the 6-His-Tag is widely exploited in affinity chromatography for protein extraction, and here ensures PG assembly onto Au gate.

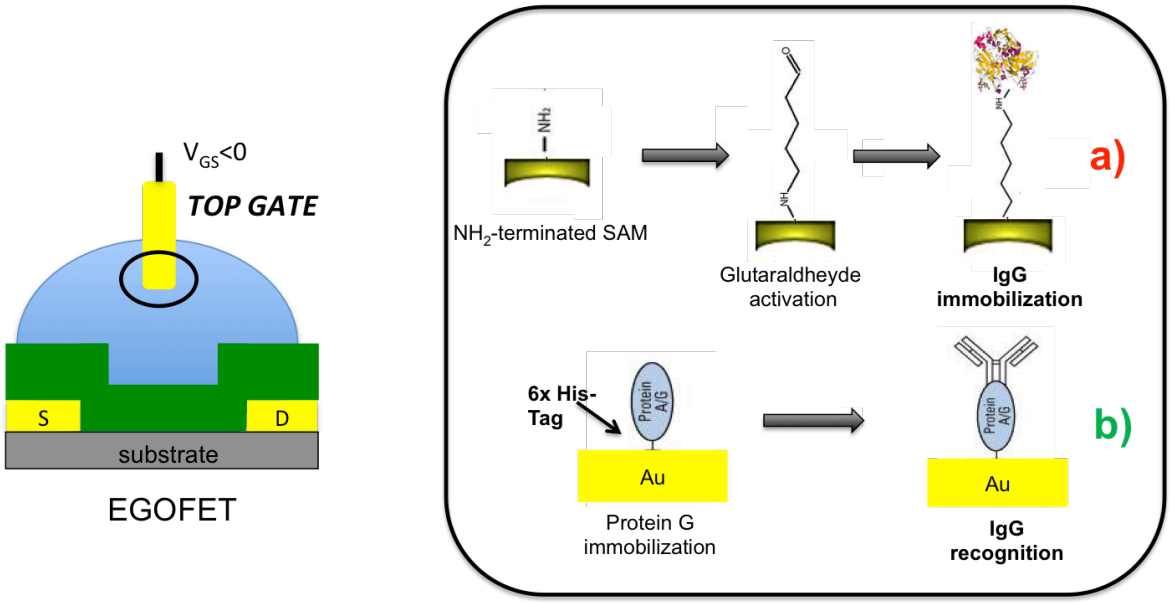

Fig. 4. 27 Functionalization steps for electrode modification a) strategy I and b) strategy II. On the left our EGOFET architecture.

This homogenous PG coating onto our Au gate electrode yields a stable biological layer, which directly promotes the Ab immobilization. Unlike HSC_6NH_2-based approach, the grafted Ab is highly oriented, because PG interacts solely with the fragment crystallizable region (Fc) of the Ab, which exposes its binding sites towards the surrounding environment.
The glutaraldehyde-based functionalization starts with the immersion of the gate electrode in a cysteamine solution (1mM) overnight. The further activation is achieved by using glutaraldehyde solution (2.5%$^{v}/_{v}$) for 1h at 5°C and then the functionalized electrode is immersed in an antibody solution (0.25mg/ml anti-IL4 and 0.1mg/ml anti-IL6) for 1h at 5°C. The last step consists by immersing the Ab-coated electrodes in buffered solution (100mM of

PBS, pH 7.4) of IL-6 (7nM) and IL-4 (5nM). The other functionalization exploits a buffered solution (100mM of PBS pH 7.4) of protein G (5mg/ml). Ab and Ag solutions are the same of the previous protocol.
6-aminohexanethiol and glutaraldehyde are purchased from Sigma-Aldrich and used without further purification. Recombinant protein G, monoclonal anti-murine IL-4, monoloclonal anti-murine IL-6, murine recombinant IL-6 and recombinant murine IL-4 are purchased from Vinci-Biochem S.r.l. (Firenze, Italy). All these biological species are produced by Biovision (San Francisco, USA).

4.3.5 Electrical characterization

I-V transfer characteristics are shown in Fig. 4.28, and strategy I turns out to be not enough sensitive towards both IL6 and IL4 at nM scale. I_{DS} current undergoes a progressive lowering after Ab immobilization but unfortunately Ag recognition does not yield a detectable change. The lack of Ab orientation yields a low number of active sites that compromises the detection of both analytes. The electrochemical desorption of the biological materials restores the drain current demonstrating that the EGOFET are not bias stressed by iterative measurements.

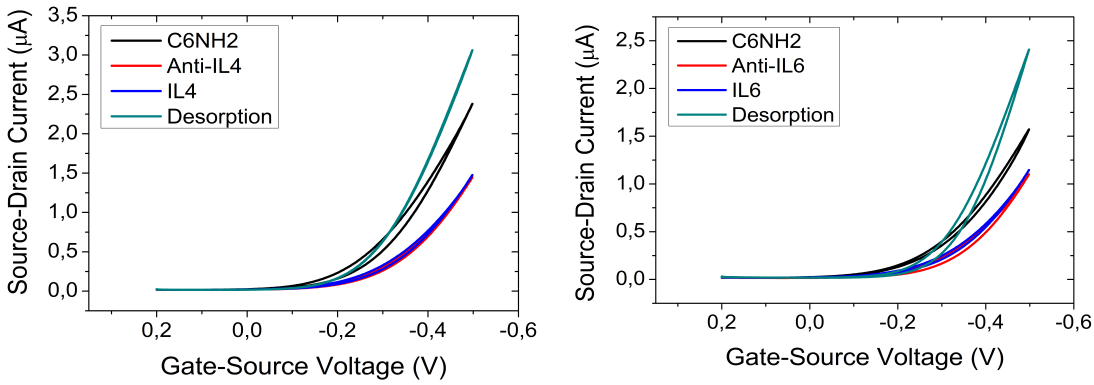

Fig.4. 28 Transfer characteristics acquired in saturation regime (V_{DS} = -0.4V) using strategy I as immobilization procedure. The two set of measurements corresponds tot he two interleukins: (left) IL4 and (right) IL6.

The use of strategy II allows a better control of the antibody orientation, as depicted in Fig. 4.27. The usual behaviour of I_{DS} for the two initial functionalization steps now is accompanied by a clear decrease of drain current induced by both IL4 and IL6 recognition down to nM range (see Fig.4.29).

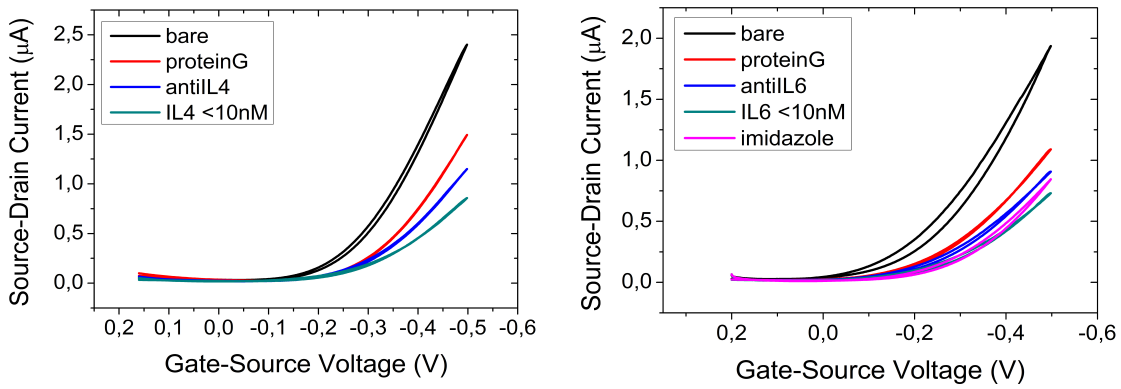

Fig.4. 29 Transfer characteristics aquired in saturation regime (V_{DS} = -0.4V) using strategy II as immobilization procedure. The two set of measurements corresponds to the two interleukins: (left) IL4 and (right) IL6.

μ and V_{th} have been extracted from the transfer characteristics, the overall trend in displayed in Fig. 4.30. In both cases, μ shows a progressive decrease as the functionalization steps proceed indicating of the weakened capacitive coupling at the gate/electrolyte interface. Concerning the threshold voltage, the two experiments shares the same V_{th} shift, but shows different trends for the two Ab-Ag couples. This is likely due to the different dipole deployment on the gate surface, because the two biological ensembles differ by electrical charges. Different interfacial dipoles usually yield different shift of threshold voltages.

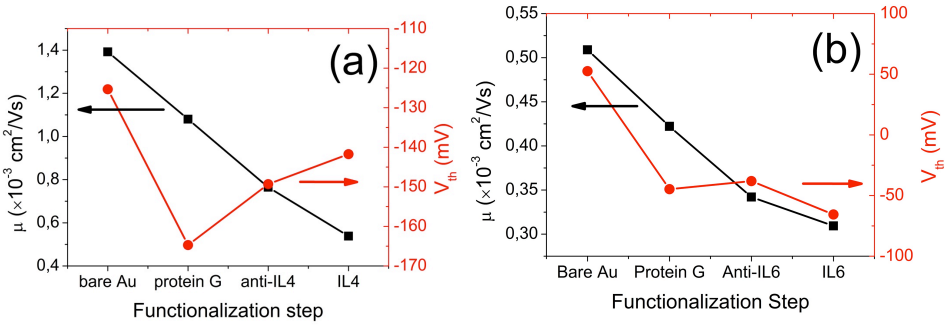

Fig.4. 30 μ and V_{th} trends extracted from transfer characteristic analysis

4.3.6 Electrochemistry

To check the quality of our gate surface and to assess each functionalization step, we have monitored the redox signal of ferricyanide, $[Fe(CN)_6]^{2-/3-}$, employing cyclic voltammetry and impedance spectroscopy. Firstly, we have e verified the presence of the two electrode modifiers, such as HSC_6NH_2 and PG.

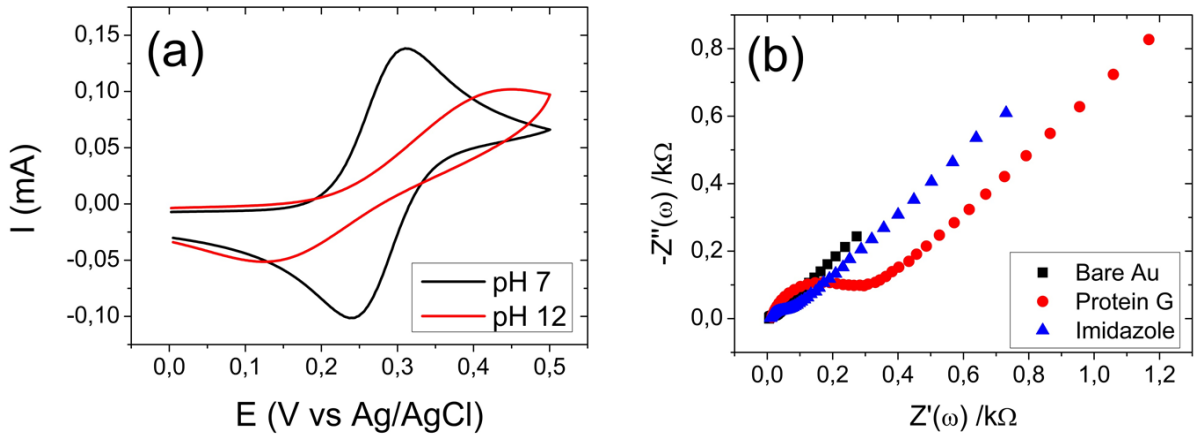

Fig.4. 31 Electrochemical validation of the two functionalization protocols. (a) CV showing the pH dependence oft he SAM using strategy I and (b) impedance response after Protein G coating.

As shown in Fig. 4.31a, the HSC_6NH_2-coated Au shows a clear pH dependence likely due to the proton equilibria of amine and/or thiolate groups onto the Au surface. Moving from neutral to basic solution, the peak to peak distance of $[Fe(CN)_6]^{2-/3-}$ increases of more than 250mV showing a dramatic slowing down of the electron transfer, which is not observed for bare Au (data not shown). On the other side, the ensemble of Protein G onto polycrystalline Au has been monitored by impedance spectroscopy. The overall response is fitted by the Randles circuit, which is an equivalent circuit composed by the electrolyte solution, R_S, the charge transfer resistance, R_{CT}, the double-layer capacitance, C_{dl} and the Warburg element, W. Impedance plots confirm the grafting of protein G, the double layer capacitance decreases from 11.3(±0.2) µF to 2.1(±0.1) µF along with an increases from 12.8(±0.2)Ω to 270(±3)Ω of the charge transfer resistance. The imidazole treatment almost restores the initial impedance response, proved by an increase of capacitance, 2.7(±0.1)µF, along with a dramatic decrease of R_{CT}, 63(±0.1)Ω

Imidazole is a direct proof of the role exerted by 6-His-Tag, which mediates the PG assembly on Au.

Furthermore, the Abs-immobilization (anti-IL4 and anti-IL6) has been electrochemically verified to both surface treatments (Fig. 4.32)

In both cases antibody immobilization induces a dramatic decrease of the C_{dl} and an increase in the charge transfer resistance.

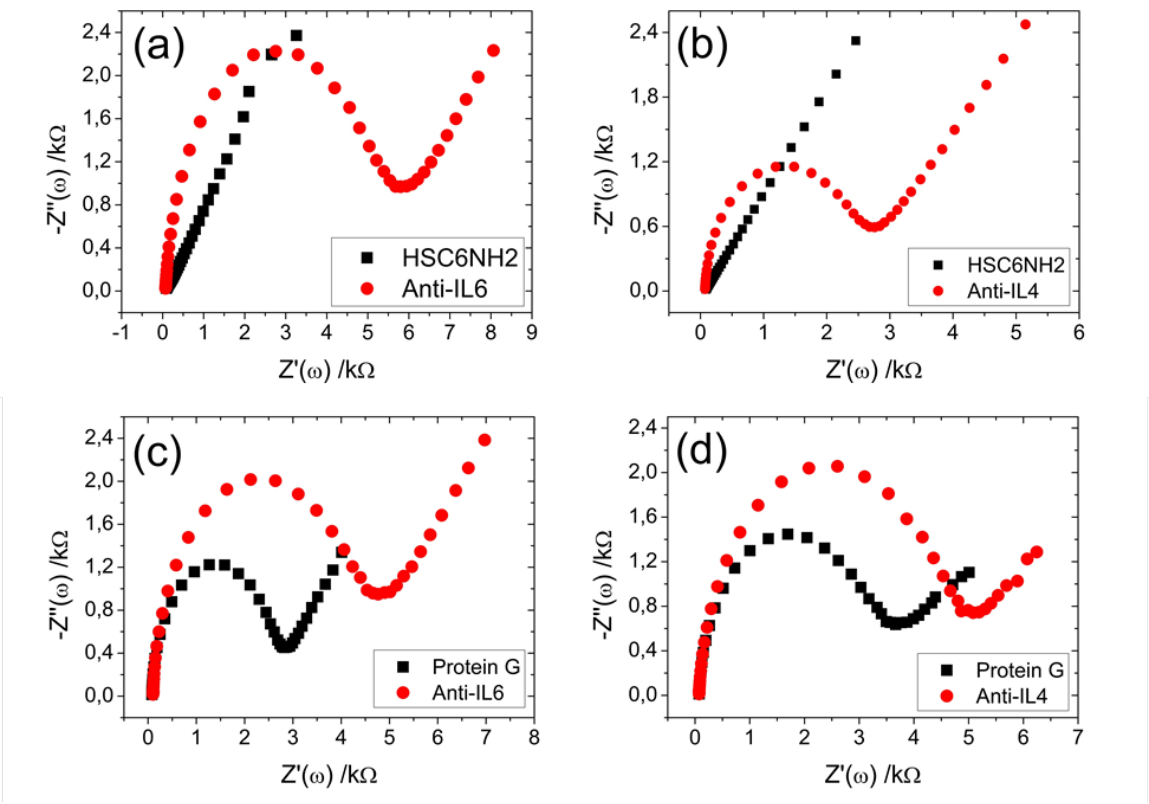

Fig.4. 32 Impedance plots oft he Anti-IL6 (a,c) and Anti-IL4 (b,d) immobilization for both functionalizations.

References:

[1] M.A. Bryant, R.M. Crooks, Determination of surface pKa values of surface-confined molecules derivatized with pH-sensitive pendant groups, Langmuir. 9 (1993) 385–387.

[2] I. Turyan, D. Mandler, Self-assembled monolayers in electroanalytical chemistry: Application of .omega.-mercaptocarboxylic acid monolayers for electrochemical determination of ultralow levels of cadmium(II), Anal. Chem. 66 (1994) 58–63.

[3] X. Lou, T. Zhao, R. Liu, J. Ma, Y. Xiao, Self-Assembled DNA Monolayer Buffered Dynamic Ranges of Mercuric Electrochemical Sensor, Anal. Chem. 85 (2013) 7574–7580.

[4] J. Lyskawa, M. Oçafrain, G. Trippé, F. Le Derf, M. Sallé, P. Viel, et al., Tetrathiafulvalene-based podands bearing one or two thiol functions: immobilization as self-assembled monolayers or polymer films, and recognition properties, Tetrahedron. 62 (2006) 4419–4425.

[5] S. Flink, F.C.J.M. van Veggel, D.N. Reinhoudt, Recognition of Cations by Self-Assembled Monolayers of Crown Ethers, J. Phys. Chem. B. 103 (1999) 6515–6520.

[6] D.L. Dermody, R.M. Crooks, T. Kim, Interactions between Organized, Surface-Confined Monolayers and Vapor-Phase Probe Molecules. 11. Synthesis, Characterization, and Chemical Sensitivity of Self-Assembled Polydiacetylene/Calix[n]arene Bilayers, J. Am. Chem. Soc. 118 (1996) 11912–11917.

[7] J.-Y. Lee, S.-M. Park, Electrochemistry of Guest Molecules in Thiolated Cyclodextrin Self-Assembled Monolayers: An Implication for Size-Selective Sensors, J. Phys. Chem. B. 102 (1998) 9940–9945.

[8] R.M. Owens, G.G. Malliaras, Organic Electronics at the Interface with Biology, 35 (2010) 449–456.

[9] M. Berggren, A. Richter-Dahlfors, Organic Bioelectronics, Adv. Mater. 19 (2007) 3201–3213.

[10] R.M. Owens, G.G. Malliaras, Organic Electronics at the Interface with Biology, MRS Bull. 35 (2010) 449–456.

[11] L. Torsi, A. Dodabalapur, L. Sabbatini, P.G. Zambonin, Multi-parameter gas sensors based on organic thin-film-transistors, Sensors Actuators B Chem. 67 (2000) 312–316.

[12] A.-M. Andringa, M.-J. Spijkman, E.C.P. Smits, S.G.J. Mathijssen, P.A. van Hal, S. Setayesh, et al., Gas sensing with self-assembled monolayer field-effect transistors, Org. Electron. 11 (2010) 895–898.

[13] P. Stoliar, E. Bystrenova, S.D. Quiroga, P. Annibale, M. Facchini, M. Spijkman, et al., {DNA} adsorption measured with ultra-thin film organic field effect transistors, Biosens. Bioelectron. 24 (2009) 2935–2938.

[14] S. Casalini, T. Cramer, F. Leonardi, M. Cavallini, F. Biscarini, Low-dimensionality effects in organic field effect transistors, in: T. Torres, G. Bottari (Eds.), Org. Nanomater. Synth. Charact. Device Appl., John Wiley & Sons, 2013: p. 614.

[15] P. Lin, F. Yan, Organic Thin-Film Transistors for Chemical and Biological Sensing, Adv. Mater. 24 (2012) 34–51.

[16] M.E. Roberts, S.C.B. Mannsfeld, N. Queraltó, C. Reese, J. Locklin, W. Knoll, et al., Water-stable organic transistors and their application in chemical and biological sensors, Proc. Natl. Acad. Sci. . 105 (2008) 12134–12139.

[17] A.N. Sokolov, M.E. Roberts, Z. Bao, Fabrication of low-cost electronic biosensors, Mater. Today. 12 (2009) 12–20.

[18] J. Mabeck, G. Malliaras, Chemical and biological sensors based on organic thin-film transistors, Anal. Bioanal. Chem. 384 (2006) 343–353.

[19] P. Bergveld, The future of biosensors, Sensors Actuators A Phys. 56 (1996) 65–73.

[20] A.N. Sokolov, M.E. Roberts, O.B. Johnson, Y. Cao, Z. Bao, Induced sensitivity and selectivity in thin-film transistor sensors via calixarene layers., Adv. Mater. 22 (2010) 2349–53.

[21] A. Al Naim, A. Hobson, R.T. Grant, A. Dragoneas, M. Hampton, C. Dunscombe, et al., Water-gated organic nanowire transistors, Org. Electron. 14 (2013) 1057–1063.

[22] M.E. Roberts, A.N. Sokolov, Z. Bao, Material and device considerations for organic thin-film transistor sensors, J. Mater. Chem. 19 (2009) 3351.

[23] M.E. Roberts, S.C.B. Mannsfeld, M.L. Tang, Z. Bao, Influence of Molecular Structure and Film Properties on the Water-Stability and Sensor Characteristics of Organic Transistors, 46 (2008) 7332–7338.

[24] M.E. Roberts, S.C.B. Mannsfeld, R.M. Stoltenberg, Z. Bao, Flexible, plastic transistor-based chemical sensors, Org. Electron. 10 (2009) 377–383.

[25] H.U. Khan, M.E. Roberts, W. Knoll, Z. Bao, Pentacene Based Organic Thin Film Transistors as the Transducer for Biochemical Sensing in Aqueous Media, Chem. Mater. 23 (2011) 1946–1953.

[26] M.L. Hammock, A.N. Sokolov, R.M. Stoltenberg, B.D. Naab, Z. Bao, Organic Transistors with Ordered Nanoparticle Arrays as a Tailorable Platform for Selective, In Situ Detection, ACS Nano. 6 (2012) 3100–3108.

[27] M.L. Hammock, O. Knopfmacher, B.D. Naab, J.B.-H. Tok, Z. Bao, Investigation of Protein Detection Parameters Using Nanofunctionalized Organic Field-Effect Transistors, ACS Nano. 7 (2013) 3970–3980.

[28] D. Khodagholy, M. Gurfinkel, E. Stavrinidou, P. Leleux, T. Herve, S. Sanaur, et al., High speed and high density organic electrochemical transistor arrays, Appl. Phys. Lett. 99 (2011) 163304.

[29] N.Y. Shim, D. a Bernards, D.J. Macaya, J. a Defranco, M. Nikolou, R.M. Owens, et al., All-plastic electrochemical transistor for glucose sensing using a ferrocene mediator., Sensors (Basel). 9 (2009) 9896–902.

[30] G. Tarabella, G. Nanda, M. Villani, N. Coppedè, R. Mosca, G.G. Malliaras, et al., Organic electrochemical transistors monitoring micelle formation, Chem. Sci. 3 (2012) 3432.

[31] L.H. Jimison, S.A. Tria, D. Khodagholy, M. Gurfinkel, E. Lanzarini, A. Hama, et al., Measurement of Barrier Tissue Integrity with an Organic Electrochemical Transistor, Adv. Mater. 24 (2012) 5919–5923.

[32] T. Someya, A. Dodabalapur, J. Huang, K.C. See, H.E. Katz, Chemical and physical sensing by organic field-effect transistors and related devices., Adv. Mater. 22 (2010) 3799–811.

[33] G. Tarabella, F. Mahvash Mohammadi, N. Coppede, F. Barbero, S. Iannotta, C. Santato, et al., New opportunities for organic electronics and bioelectronics: ions in action, Chem. Sci. 4 (2013) 1395–1409.

[34] F. Buth, D. Kumar, M. Stutzmann, J.A. Garrido, Electrolyte-gated organic field-effect transistors for sensing applications, Appl. Phys. Lett. 98 (2011) -.

[35] L. Kergoat, L. Herlogsson, D. Braga, B. Piro, M.-C. Pham, X. Crispin, et al., A Water-Gate Organic Field-Effect Transistor, Adv. Mater. 22 (2010) 2565–2569.

[36] T. Cramer, A. Kyndiah, M. Murgia, F. Leonardi, S. Casalini, F. Biscarini, Double layer capacitance measured by organic field effect transistor operated in water, Appl. Phys. Lett. 100 (2012) -.

[37] S. Casalini, F. Leonardi, T. Cramer, F. Biscarini, Organic field-effect transistor for label-free dopamine sensing, Org. Electron. 14 (2013) 156–163.

[38] L. Kergoat, B. Piro, M. Berggren, M.-C. Pham, A. Yassar, G. Horowitz, {DNA} detection with a water-gated organic field-effect transistor, Org. Electron. 13 (2012) 1–6.

[39] S. Cotrone, M. Ambrico, H. Toss, M.D. Angione, M. Magliulo, A. Mallardi, et al., Phospholipid film in electrolyte-gated organic field-effect transistors, Org. Electron. 13 (2012) 638–644.

[40] H. Tang, P. Lin, H.L.W. Chan, F. Yan, Highly sensitive dopamine biosensors based on organic electrochemical transistors, Biosens. Bioelectron. 26 (2011) 4559–4563.

[41] J.D. Helsworth, R.H. Roth, Dopamine Synthesis , Uptake , Metabolism , and Receptors : Relevance to Gene Therapy of Parkinson ' s Disease, Exp. Neurol. 9 (1997) 4–9.

[42] A. Carlsson, THE OCCURRENCE, DISTRIBUTION AND PHYSIOLOGICAL ROLE OF CATECHOLAMINES IN THE NERVOUS SYSTEM, Pharmacol. Rev. . 11 (1959) 490–493.

[43] C.D. Marsden, Parkinson's disease, Lancet. 335 (1990) 948–949.

[44] T.M. Dawson, V.L. Dawson, Molecular pathways of neurodegeneration in Parkinson's disease., Science. 302 (2003) 819–22.

[45] M. Goedert, Alpha-synuclein and neurodegenerative diseases, Nat Rev Neurosci. 2 (2001) 492–501.

[46] J. Lotharius, P. Brundin, Impaired dopamine storage resulting from α-synuclein mutations may contribute to the pathogenesis of Parkinson's disease, Hum. Mol. Genet. . 11 (2002) 2395–2407.

[47] J. Lotharius, P. Brundin, Pathogenesis of parkinson's disease: dopamine, vesicles and [alpha]-synuclein, Nat Rev Neurosci. 3 (2002) 932–942.

[48] P. Capella, B. Ghasemzadeh, K. Mitchell, R.N. Adams, Nafion-coated carbon fiber electrodes for neurochemical studies in brain tissue, Electroanalysis. 2 (1990) 175–182.

[49] B. Li, Z. Zhang, Y. Jin, Plant tissue-based chemiluminescence flow biosensor for determination of unbound dopamine in rabbit blood with on-line microdialysis sampling, Biosens. Bioelectron. 17 (2002) 585–589.

[50] J. Justice Jr., Introduction to In Vivo Voltammetry, in: J. Justice Jr. (Ed.), Voltammetry Neurosci. SE - 1, Humana Press, 1987: pp. 3–101.

[51] R.K. Shervedani, M. Bagherzadeh, Electrochemical Characterization of In Situ Functionalized Gold Cysteamine Self-Assembled Monolayer with 4-Formylphenylboronic Acid for Detection of Dopamine, Electroanalysis. 20 (2008) 550–557.

[52] P. Lin, X. Luo, I.-M. Hsing, F. Yan, Organic Electrochemical Transistors Integrated in Flexible Microfluidic Systems and Used for Label-Free DNA Sensing, Adv. Mater. 23 (2011) 4035–4040.

[53] P. Lin, F. Yan, H.L.W. Chan, Ion-Sensitive Properties of Organic Electrochemical Transistors, ACS Appl. Mater. Interfaces. 2 (2010) 1637–1641.

[54] L. V Protsailo, W.R. Fawcett, Studies of electron transfer through self-assembled monolayers using impedance spectroscopy, Electrochim. Acta. 45 (2000) 3497–3505.

[55] A.L. Eckermann, D.J. Feld, J.A. Shaw, T.J. Meade, Electrochemistry of redox-active self-assembled monolayers, Coord. Chem. Rev. 254 (2010) 1769–1802.

[56] http://goldbook.iupac.org

[57] X. Jiang, D. Li, X. Xu, Y. Ying, Y. Li, Z. Ye, et al., Immunosensors for detection of pesticide residues, Biosens. Bioelectron. 23 (2008) 1577–1587.

[58] B. Van Dorst, J. Mehta, K. Bekaert, E. Rouah-Martin, W. De Coen, P. Dubruel, et al., Recent advances in recognition elements of food and environmental biosensors: A review, Biosens. Bioelectron. 26 (2010) 1178–1194.

[59] M. Sharpe, It's a bug's life: biosensors for environmental monitoring, J. Environ. Monit. 5 (2003) 109N–113N.

[60] S. Rodriguez-Mozaz, M.-P. Marco, M.J. Lopez de Alda, D. Barcelò, Biosensors for environmental applications: Future development trends, Pure Appl. Chem. 76 (2004) 723–752.

[61] S. Kröger, S. Piletsky, A.P.F. Turner, Biosensors for marine pollution research, monitoring and control, Mar. Pollut. Bull. 45 (2002) 24–34.

[62] F. Rusmini, Z. Zhong, J. Feijen, Protein Immobilization Strategies for Protein Biochips, Biomacromolecules. 8 (2007) 1775–1789.

[63] E. Steen Redeker, D.T. Ta, D. Cortens, B. Billen, W. Guedens, P. Adriaensens, Protein Engineering For Directed Immobilization, Bioconjug. Chem. 24 (2013) 1761–1777.

[64] http://ione-fp7.eu

[65] T. Kishimoto, The biology of Interleukin-6, J. Am. Soc. Hematol. 74 (1989) 1–10.

[66] J. Van Snick, Interleukin-6: an overview., Annu. Rev. Immunol. 8 (1990) 253–78.

[67] P.C. Heinrich, J. V Castell, T. Andus, Interleukin-6 and the acute phase response., Biochem. J. 265 (1990) 621–36.

[68] S. Flink, F. C. J. M. van Veggel and D. N. Reinhoudt, Sensor functionalities in Self-Assembled Monolayers, Adv Mater. 12 (2000) 1315-1328.

[69] A. K. Trilling, J. Beekwilder and H. Zuilhof, Antibody orientation on biosensor surfaces: a minireview, Analyst, 138 (2013) 1619-1617.

Appendix A

Estimation of field-effect mobility μ corrected for the contact series resistance

As reported in Chapter 2.1.2, field-effect mobility μ in saturation regime ($V_{DS} > V_{GS} - V_{th}$) is usually modelled as:

$$I_{DS\,sat} = \left(\frac{W}{2L}\right) \mu\, C_i (V_{GS} - V_{th})^2 \qquad \text{Eq. A1}$$

where W and L are channel width and length and C_i is the capacitance of the gate insulator and this parameter is therefore estimated from the slope of $\sqrt{I_{DS}}$ *vs* V_{GS}. However this model does not take into account of any variation of the electric field along the channel or free carrier concentration and ignores the contact resistance effects.
To estimate mobility corrected by contact resistance, Horowitz and co-workers [1] develop a method that depends on the drain current at low drain voltage.
In fact the I_{DS} follows Ohm's law for low drain voltage and can be modelled as:

$$I_{DS} = \left(\frac{W}{L}\right) \mu\, C_i (V_{GS} - V_{th}) V_{DS} \qquad \text{Eq. A2}$$

by differentiating Eq. A2 with respect to gate voltage, the result is the so-called transconductance g_m:

$$g_m = \frac{\partial I_{DS}}{\partial V_{GS}} = \frac{W}{L} \mu\, C_i V_{DS} \qquad \text{Eq. A3}$$

Eq. A3 is useful for estimating the gate bias dependent mobility at low drain voltage.
The model is improved by accounting for the contact resistance at source and drain, hence we add in Eq. A2 the voltage drop through a series resistance R_C:

$$I_{DS} = \frac{W}{L}\, C_i \mu (V_{GS} - V_{th})(V_{DS} - I_{DS} R_C) =$$

$$= \frac{(W/L)\mu\, C_i (V_{GS} - V_{th}) V_{DS}}{1 + (W/L)\mu\, R_C C_i (V_{GS} - V_{th}) V_{DS}} \qquad \text{Eq. A4}$$

Eq. A4 requires only R_C to be voltage independent that is a reasonable scenario considering the low longitudinal electric field of a transistor in planar geometry and ignoring the gate voltage.
To remove the contribution of R_C, we firstly estimate the drain conductance g_d (by considering in our case the output curve at V_{GS} = -40) and the transconductance g_m defined as:

$$g_d = \frac{\partial I_{DS}}{\partial V_{DS}} = \frac{I_{DS}}{V_{DS}} = \frac{(W/L)\mu\, C_i (V_{GS} - V_{th})}{1 + (W/L)\mu\, R_C C_i (V_{GS} - V_{th})} \qquad \text{Eq. A5}$$

$$g_m = \frac{\partial I_{DS}}{\partial V_{GS}} = \frac{(W/L)\mu\, C_i V_{DS}}{[1+(W/L)\mu\, R_C C_i (V_{GS}-V_{th})]^2} \qquad \text{Eq. A6}$$

to eliminate the series resistance is sufficient divide Eq. A5 by the square root of Eq. A6:

$$\frac{g_d}{\sqrt{g_m}}\sqrt{\frac{L}{W}}\frac{V_{DS}}{C_i} = \sqrt{\mu}(V_{GS} - V_{th}) \qquad \text{Eq. A7}$$

Once the I-V transfer characteristic at low drain voltage (V_{DS} = -1 in our case) is recorded, Eq. A7 can be correctly applied with respect to gate voltage.
The contact resistance could be extracted by the following expression derived directly from Eq. A5:

$$R_C = \frac{1}{g_d} - \frac{L}{W\mu C_i (V_{GS}-V_{th})} \qquad \text{Eq. A8}$$

the data of R_C obtained for our homolog series of hydrophilic SAMs [2] is show in Fig. A1. As already mentioned in Chapter 3 the trend is V_{GS} independent (except for low V_{GS}) and for high gate voltage R_C approach to constant value independent of V_{th}.

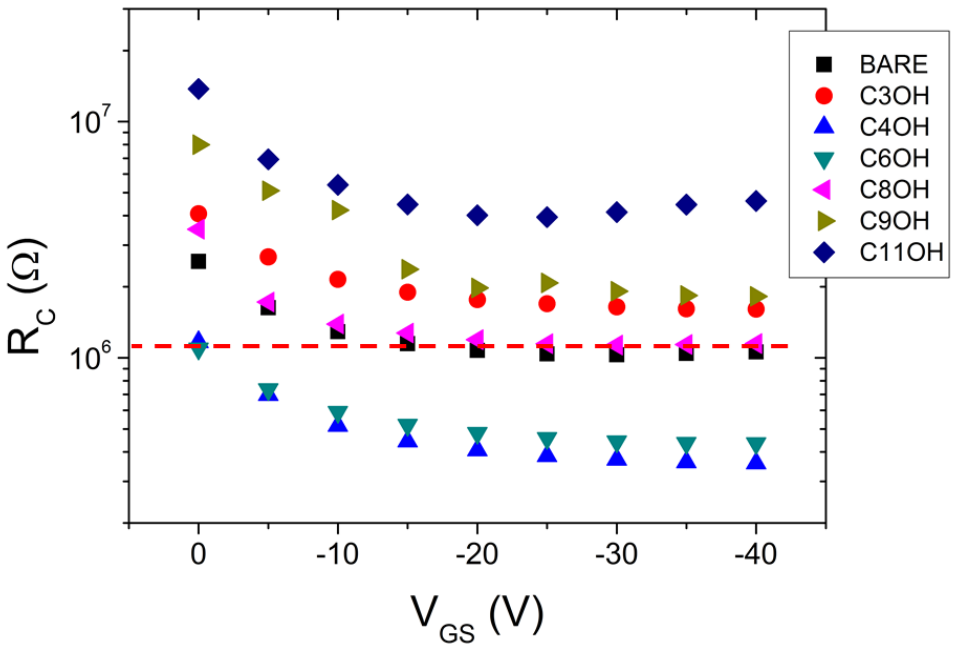

Fig. A1 Contact resistance vs. gate-source voltage for each functionalization. As example, R_C has been extracted for C8OH by intercepting the resistance saturation value (red dashed line) to the Y-axis.

References:

[1] G. Horowitz, R. Hajlaoui, D. Fichou, A. El Kassmi, Gate voltage dependent mobility of oligothiophene field-effect transistors, J. Appl. Phys. 85 (1999).

[2] S. Casalini, A. Shehu, F. Leonardi, C. Albonetti, F. Borgatti, F. Biscarini, Hydrophilic self-assembly monolayers for pentacene-based thin-film transistors, Org. Electron. 14 (2013) 1891–1897.

Appendix B

Determination of surface coverage by means of electrochemical reductive measurements.

This section present how can be quantified the monolayer coverage of alkanethiol assembled on gold surfaces.
In a series of work in 1991, Porter et al. [1,2] demonstrated that these films desorb in alkaline solution (pH>11) through the following redox reaction:

$$AuS(CH_2)_n\,CH_3 + 2H_2O \longrightarrow Au(0) + {}^{-}O_2S(CH_2)_n\,CH_3 + 4H^+ + 3e^- \qquad (I)$$

$$AuS(CH_2)_n\,CH_3 + e^- \longrightarrow Au(0) + {}^{-}S(CH_2)_n\,CH_3 \qquad (II)$$

Where (I) is a multi-electronic oxidative path whereas (II) is the mono-electronic reductive one. Our experiments of reductive desorption are carried out exploiting reaction (II)
Fig. B1 displays our electrochemical reductive desorption for the four oligoarylenes molecules performed in a conventional three-electrode cell with KOH 0.5 M as supporting electrolyte. The potential ranges from 0.4 to -2.4 V and each scan is repeated three time in order to verify the complete vanishing of the desorption peak (in our case no peaks are observed after the first cycle).

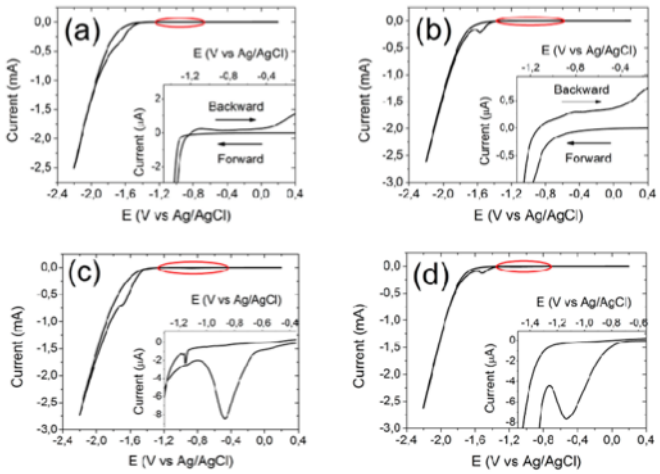

Fig. B1 Reductive desorption graphs of (a) MTM, (b) MTD, (c) NTM, and (d) NTD. Each inset is the magnification of the potential range highlighted by the red circle.

The reductive peaks are clearly placed in the onset of the electrolyte reduction but they are sharp enough to get a reliable value for the charge of the Au-S bond. [3]
By integrating the reduction peaks and knowing the redox reaction, the charge has been extracted applying the following Eq.:

$$\Gamma = Q/nFA \qquad \text{Eq. B1}$$

where Q is the charge required to break Au-S bond (espressed in C/cm^2), n is the number of electrons involved in the electron transfer process (for the reductive desorption n = 1), F is Faraday constant and A is the area of the electrode (1mm^2 in our case).

Γ is the surface coverage expressed in moles/cm^2, the values extracted for MTM, MTD, NTM and NTD thiols are reported in Table B1:

	MTM	**MTD**	**NTM**	**NTD**
Γ x10^{-10} (mol/cm^2)	5.3 ± 0.4	4.8 ± 0.2	6.0 ± 0.2	6.1 0.02

Once you have extracted Γ, the step forward is the extraction of the number of molecules and the percentage of surface coverage by considering the projected area of the molecule.
The values extracted from Fig. B1 are slightly lower with respect to a perfect packed alkanethiol SAMs (Γ = 9.3 × 10^{-10} mol/cm^2). [2]
MTD and NTD peaks are located at −1.53−1.55 V (vs Ag/AgCl), while MTM and NTM at −1.67 V (vs Ag/AgCl). Notably, the higher reduction charge density observed for MTD and NTD is almost twice as large as that of MTM and NTM, indicating that the binding of MTD and NTD occurs via both thiolate groups.
It is also worth noting that a cathodic peak (highlighted with a red circle in the graph) is invariably observed for NTM and NTD, prior to the S−Au cleavage but not for MTM and MTD. This signal is ascribed to the reduction of the $-NO_2$ group and is placed at−0.869 V (*vs* Ag/AgCl) for NTM thiol and at −1.089 V (*vs* Ag/AgCl) for NTD.

References:

[1] M.M. Walczak, D.D. Popenoe, R.S. Deinhammer, B.D. Lamp, C. Chung, M.D. Porter, Reductive desorption of alkanethiolate monolayers at gold: a measure of surface coverage, Langmuir. 7 (1991) 2687–2693.

[2] C.A. Widrig, C. Chung, M.D. Porter, The electrochemical desorption of n-alkanethiol monolayers from polycrystalline Au and Ag electrodes, J. Electroanal. Chem. Interfacial Electrochem. 310 (1991) 335–359.

[3] A.H. Suroviec, Determining Surface Coverage of Self-Assembled Monolayers on Gold Electrodes, Chem. Educ. 17 (2012) 83–85.

Appendix C

Determination of s_c and ΔV_{th}

Considering Fig. D1, the adsorption of DA at the gate/electrolyte interface (denoted as C_2) induces variations in terms of capacitance and threshold voltage.

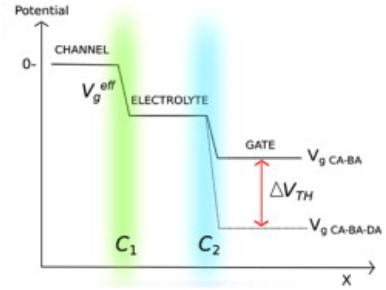

Fig. D1 Potential profile along the spatial coordinate x showing the two capacitive drops related to organic semiconductor/electrolyte and gate/electrolyte interfaces respectively

Our goal is to extract values of C_2 and $\Delta\phi_D$ from transfer measurements $I_{DS}(V_{GS})$ with a gate electrode functionalized at different DA concentrations. In our measurements the semiconductor/electrolyte interface does not change and therefore $I_{DS}(V_{G,\,eff})$ is constant and represent an universal transfer curve

The total charge Q at the electrolyte/semiconductor interface is determined by the effective gate voltage $V_{G,eff}$ felt by the semiconductor. If we consider that $V_{G,\,eff}$ is affected by the potential applied by the instrumentation V_{GS} and the variation of surface dipole $\Delta\phi_D$, we can write:

$$Q = C_1 V_{G,eff} = C_{tot}(V_G + \Delta\phi_D) \qquad \text{Eq. D1}$$

where C_{tot} is given by:

$$C_{tot} = \frac{C_1 \cdot C_2}{C_1 + C_2} \qquad \text{Eq. D2}$$

for two in-series capacitance, C_1 and C_2.

By rearranging eq.D2:

$$V_{G,eff} = \frac{C_2}{C_1 + C_2}(V_G + \Delta\phi_D) \qquad \text{Eq. D3}$$

As the absolute value of $V_{G,eff}$ cannot be determined, we use the transfer curve obtained with the unfunctionalized gate electrode $V_{G,\,\mathrm{ref}}$ as reference:

$$V_{G,eff} = \frac{C_{2,ref}}{C_1 + C_{2,ref}}\left(V_{G,ref} + \Delta\phi_{D,ref}\right) = \frac{C_{2,DA}}{C_1 + C_{2,DA}}\left(V_{G,DA} + \Delta\phi_{D,DA}\right) \qquad \text{Eq. D4}$$

simple rearrangements lead to:

$$V_{GS,ref} = \frac{C_{2,DA}(C_1 + C_{2,ref})}{C_{2,ref}(C_1 + C_{2,DA})}\left(V_{G,DA} + \Delta\phi_{D,DA}\right) - \Delta\phi_{D,ref} \qquad \text{Eq. D5}$$

where $s_c = \frac{C_{2,DA}(C_1 + C_{2,ref})}{C_{2,ref}(C_1 + C_{2,DA})}$ is the capacitive scaling parameters used in Chapter 4.

Now the expression can be reduced to:

$$V_{GS,ref} = s_c\left(V_{G,DA} + \Delta\phi_{D,DA} - \frac{\Delta\phi_{D,ref}}{s_c}\right) \qquad \text{Eq. D6}$$

where $\Delta V_{th} = \Delta\phi_{D,DA} - \frac{\Delta\phi_{D,ref}}{s_c}$ denote the threshold voltage shift induced by dopamine adsorption.

Finally we obtain the relation for rescaling the gate voltage as used in Chapter 4:

$$V_{GS,ref} = s_c(V_{G,DA} + \Delta V_{th}) \qquad \text{Eq. D7}$$

List of Abbreviations:

Ab Antibody
AFM Atomic Force Microscopy
Ag Antigene
AMID Active Multifunctional Implantable Device
BA Boronic Acid
BC Bottom Contact
BG Bottom Gate
C_{dl} Double Layer Capacitance
C_i Dielectric Capacitance
CA Cysteamine
CE Counter Electrode
CIOG Charge Injection Organic Gauge
CPE Constant Phase Element
CV Cyclic Voltammetry
D Drain
DA Dopamine
EDL Electrical Double layer
EGOFET Electrolyte-Gated Organic Field-Effect Transistor
EIS Electrochemical Impedance Spectroscopy
FET Field Effect Transistor
G Gate
HF Hydrofluoric Acid
HMDS 1,1,1,3,3,3 hexamethyldisilazane
HV High Vacuum
L Channel Length
IL4 Interleukin 4
IL6 Interleukin 6
MTD 4-methoxy- terphenyl-3′′,5′′-dimethanethiol
MTM 4- methoxy-terphenyl-4′′-methanethiol
ML Monolayer
ML-SAM Multi-Layer Self-Assembled Monolayer
NTD 4-nitro-terphenyl-3′′,5′′- dimethanethiol
NTM 4-nitro-terphen- yl-4′′-methanethiol
OTFT Organic Thin-Film Transistor
OECT Organic Electrochemical Transistor
OFET Organic Field Effect Transistors
OS Organic Semiconductor
ODTS Octadecyltrichlorosilane
PD Parkinson's disease
PDMS Polydymetilsiloxane
P3HT Poly(3-hexylthiophene-2,5-diyl)
PEDOT:PSS poly(3,4-ethylenedioxythiophene) poly(styrenesulfonate)

R_{ch} Channel Resistance
R_{ct} Charge Transfer Resistance
R_s Solution Resistance
RE Reference Electrode
Redox Reduction-Oxidation
S Source
SAM Self-Assembled Monolayer
SCI Spinal Cord Injury
SMU Source Measure Unit
TBD (4′-(Thiophen-2-yl)Biphenyl-3,5-diyl) Dimethanethiol
TBM (4′-(Thiophen-2-yl)Biphenyl-4-yl)Methanethiol
TC Top Contact
TD ([1,1′;4′,1′′] Terphenyl-3,5-diyl)Dimethanethiol
TG Top gate
TP Test Pattern
UHV Ultra-High Vacuum
V_c Critical Voltage
V_{TH} Threshold Voltage
W Channel Width or Warburg Impedance Element
W_A Work of Adhesion
WE Working Electrode
Z_r (Z') Real Impedance
Z_{im} (Z'') Imaginary Impedance

μ Charge Carriers Mobility
β Exponential Tunnelling Factor
α Roughness Exponent or Phenomenological Exponent
ξ Correlation Length
σ_{rms} Root Mean Square Roughness
Θ Film Thickness/Coverage
Φ Deposition Rate
λ Wavelength
θ Contact Angle

List of Publications:

- Cavallini M. D'Angelo P., Vendrell Criado V., Gentili D., Shehu A., Leonardi F., Milita S., Liscio F., Biscarini F., 'Ambipolar Multi-Stripe Organic Field-Effect Transistors', Advanced Materials, **2011**, 23, 5091-5097.
- Casalini S., Shehu A., Destri S., Porzio W., Pasini M. C., Vignali F., Borgatti F., Albonetti C., Leonardi F., Biscarini F., 'Organic field-effect transistors as new paradigm for large-area molecular junctions', *Organic Electronics*, **2012**, 13, 789-795.
- Cramer T., Kyndiah A., Murgia M., Leonardi F., Casalini S., and Biscarini F., 'Double Layer Capacitance Measured by Organic Field Effect Transistor Operated in Water', *Applied Physics Letters*, **2012**, 100, 143302.
- Gentili D., Gonzalo Givaja G., Mas-Balleste R., Azani M. R., Shehu A., Leonardi F., Mateo-Marti E., Greco P., Zamora F. and Cavallini M. 'Patterned conductive nanostructures from reversible self-assemble of 1D coordination polymer', *Chemical Science*, **2012**, 3, 2047-2051.
- Gentili D., Di Maria F., Liscio F., Ferlauto L., Leonardi F., Maini L., Gazzano M., Milita S., Barbarella G. and Cavallini M. 'Targeting ordered oligothiophene fibers with enhanced functional properties by interplay of self-assembly and wet lithography', *Journal of Materials Chemistry*, **2012,** 22, 20852.
- Casalini S., Leonardi F., Bortolotti C. A., Operamolla A., Hassan Omar O., Paltrinieri L., Albonetti C., Farinola G. M. and Biscarini F. 'Mono/Bidentate Thiol Oligoarylenes-based Self-Assembled Monolayers (SAMs) for Interface Engineering', *Journal of Materials Chemistry*, **2012**, 22, 12155.
- Casalini S., Cramer T., Leonardi F., Cavallini M. and Biscarini F., 'Organic Nanomaterials: Synthesis, Characterization and Device Applications', Wiley Book, ISBN: 9781118016015, **2013**.
- Casalini S., Leonardi F., Cramer T., Biscarini F. 'Organic field-effect transistor for label-free dopamine sensing', *Organic Electronics*, **2013**, 14, 156-163.
- Casalini S., Shehu A., Leonardi F., Albonetti C., Borgatti F., Biscarini F., 'Hydrophilic self-assembly monolayers for pentacene-based thin- film transistors', *Organic Electronics*, **2013**, 14, 1891-1897.
- Cramer T., Campana A., Leonardi F., Casalini S., Kyndiah A., Murgia M. and Biscarini F. 'Water-gated organic field effect transistors – opportunities for biochemical sensing and extracellular signal transduction', *Journal of Materials Chemistry B,* **2013**, 1, 3728-3741.
- Casalini S., Leonardi F., Cramer T., Campana A., Biscarini F., 'Bio-sensing based on electrochemically-gated organic field-effect transistors', *La chimica e l'industria*, **2013**, 5, 104-105.
- Gentili D., Sonar P., Liscio F., Cramer T., Ferlauto L., Leonardi F., Milita S., Dodabalapur A., and Cavallini M. 'Logic-Gate Devices Based on Printed Polymer Semiconducting Nanostripes', *Nano Letters*, **2013**, 13, 3643-3647.
- Casalini S., Berto M., Leonardi F., Operamolla A., Bortolotti C. A., Borsari M., Sun W., Di Felice R., Corni S., Albonetti C., Hassan Omar O., Farinola G. M., and Biscarini F. 'Self-Assembly of mono- and bi-dentate oligoarylene thiols onto polycristalline Au', *Langmuir*, **2013**, 29, 13198-13208.

Acknowledgments:

Mi ritengo una persona fortunata principalmente per due motivi: il mio percorso di dottorato è stato pieno di soddisfazioni e ho avuto la possibilità di lavorare con persone meravigliose sia dal punto di vista umano che lavorativo. Alla fine di questa tesi non mi resta che ringraziare tutti per il supporto e per i preziosi consigli. Non ritengo necessario fare la solita lista di nomi perché penso che il sorriso che rivolgo loro ogni giorno faccia loro capire quanto gli sia grata.

Grazie ragazze per essere state delle amiche, non solo delle colleghe…non avrei potuto desiderare di più.

C'è una persona che ringrazio in modo particolare ed è chi più di tutti mi ha consolato, consigliato, guidato e sostenuto. A questa persona devo un immenso grazie per tutto ciò che ha fatto e per la grande pazienza, spero che per noi sia solo l'inizio…

''On ne voit bien qu'avec le cœur. L'essentiel est invisible pour les yeux ''

Non si vede bene che col cuore. L'essenziale è invisibile agli occhi

Antoine de Saint-Exupéry